UNIVERSITY OF SOUTHAMPTON

Optical time resolved spin dynamics in III-V semiconductor quantum wells

by

Matthew Anthony Brand

A thesis submitted for the degree of

Doctor of Philosophy

at the Department of Physics

August 2003

UNIVERSITY OF SOUTHAMPTON

ABSTRACT

FACULTY OF SCIENCE

Doctor of Philosophy

"Optical time resolved spin dynamics in III-V semiconductor quantum wells"

Matthew Anthony Brand

This thesis presents time-resolved measurements of the spin evolution of transient carrier populations in III-V quantum wells. Non-equilibrium distributions of spin polarisation were photoexcited and probed with picosecond laser pulses in three samples; a high mobility modulation n-doped sample containing a single GaAs/AlGaAs quantum well, an $In_{0.11}Ga_{0.89}As$/GaAs sample containing three quantum wells and, a multi-period GaAs/AlGaAs narrow quantum well sample.

Electron spin polarisation in low mobility wells decays exponentially. This is successfully described by the D'yakonov-Perel (DP) mechanism under the frequent collision regime, within which the mobility can be used to provide the scattering parameter. This work considers the case of a high mobility sample where collisions are infrequent enough to allow oscillatory spin evolution. It is shown however, that in n-type quantum wells the electron-electron scattering inhibits the spin evolution, leading to slower, non-oscillatory, decays than previously expected.

Observed electron spin relaxation in InGaAs/InP is faster than in GaAs/AlGaAs. This may be ascribed to an enhanced DP relaxation caused by Native Interface Asymmetry (NIA) in InGaAs/InP, or to the differing natures of the well materials. Here the two possibilities have been distinguished by measuring electron spin relaxation in InGaAs/GaAs quantum wells. The long spin lifetime implicates the NIA as the cause of the fast relaxation in InGaAs/InP.

Finally, the reflectively probed optically induced linear birefringence method has been used to measure quantum beats between the heavy-hole exciton spin states, which are mixed by a magnetic field applied at various angles to the growth direction of the GaAs/AlGaAs multi-quantum well sample within which the symmetry is lower than D_{2d}. Mixing between the optically active and inactive exciton spin states by the magnetic field, and between the two optically active states by the low symmetry, are directly observed.

This thesis is dedicated to my parents.

Acknowledgments

Many people have made my time at the Department of Physics in Southampton enjoyable, interesting and educational. In particular I would like to thank: Richard Harley for excellent supervision and much encouragement over the years; Andy Malinowski who as a postdoc in the early part of this work taught me much about how to obtain useful results actually and efficiently; Phil Marsden for his technical assistance and many useful discussions; Jeremy Baumberg, David Smith, Geoff Daniell and Oleg Karimov who have clarified some specific physics topics I was having difficulties with.

I would also like to thank my family whose support and encouragement has made this possible.

Contents

1. Introduction 1

2. Electrons in III-V semiconductor heterostructures 4

3. Time-resolved measurement method 16

4. Electron-electron scattering and the D'Yakonov-Perel mechanism in a high mobility electron gas 22

4.1 Introduction 22

4.2 Background 23

4.3 Theory 25

4.3.1 Conduction band spin-splitting and the D'yakonov-Perel mechanism 25

4.3.2 Evolution of spin polarisation excited in the valance band 28

4.3.3 Energy distribution of the electron spin polarisation 29

4.4 Sample description 32

4.4.1 Sample mobility 34

4.4.2 Optical characterisation 36

4.5 Experimental procedure 38

4.6 Results 38

4.7 Analysis 44

4.7.1 Monte-Carlo simulation 45

4.7.2 Electron-electron scattering 47

4.7.3 Spectral sampling of the conduction band spin-splitting and anisotropy 48

4.8 Summary and conclusions **55**

4.9 References **57**

5. Spin relaxation in undoped InGaAs/GaAs quantum wells ***60***

5.1 Introduction **60**

5.2 Background and theory **61**

5.2.1 Exciton spin dynamics 62

5.2.2 Effects of temperature 67

5.3 Sample description **71**

5.4 Experimental procedure **71**

5.5 Results **74**

5.6 Analysis **94**

5.7 Interpretation **99**

5.7.1 Phases in the evolution of the excited population 100

5.7.2 Exciton thermalisation 101

5.7.3 Thermalised excitons 103

5.7.4 Comparison with InGaAs/InP, the Native Interface Asymmetry 107

5.7.5 Dynamics of the unbound e-h plasma and carrier emission 108

5.8 Summary and conclusions **112**

5.9 References **114**

6. Exciton spin precession in a magnetic field ***117***

6.1 Introduction **117**

6.2 Background and theory 118

6.3 Sample description 124

6.4 Experiment 125

6.5 Results 127

6.6 Summary and Conclusions 140

6.7 References 141

7. Conclusions *143*

7.1 References 146

8. List of Publications *147*

1. Introduction

This thesis concerns the optical manipulation of electron spin in III-V semiconductor heterostructures. It presents measurements of the time evolution of transient spin polarised carriers on a picosecond timescale.

Some of the information contained in the polarisation state of absorbed light is stored in the spin component of the excited state of the absorbing medium, it is lost over time due to processes which decohere or relax the spin polarisation in the medium. How well a material can preserve spin information is represented by the spin relaxation and decoherence rates, quantities which depend on many parameters, the principal determinants are temperature; quantum confinement; and external and internal electromagnetic field configurations, manipulated for example by doping, and excitation intensity. Hysteresis effects are also possible in magnetic-ion doped semiconductors. Mechanisms of light absorption and energy retention in semiconductors can be described in terms of the photo-creation of transient populations of various quantum quasi-particles; electrons, holes, excitons and phonons being the most basic kind. Holes and excitons are large scale manifestations of electron interactions, whereas phonons represent vibrational (thermal) excitations of the crystal lattice. More exotic wavicles such as the exciton-photon polariton; the exciton-phonon polariton, bi-, tri- and charged-exciton; and plasmon states are obtained from various couplings between members of the basic set. It has been found that the basic set of excitations suffice for the work presented in this thesis.

Many current semiconductor technologies exploit only the charge or Coulomb driven interactions of induced non-equilibrium electron populations to store, manipulate and transmit information. It has long been recognised that in addition information of a

fundamentally different, quantum, nature may also be carried by the electron spin. Many proposals for advances in information processing, the development of quantum computing and spin electronic devices, involve manipulation of spin in semiconductors.

Currently, most mass produced semiconductor devices are Silicon based. From an economic viewpoint, since the industrial production infrastructure is already in place, spin manipulation technologies based on Silicon would be most desirable. Silicon is however an indirect gap semiconductor, it couples only weakly to light, which, in respect of optical spin manipulation, places it at a disadvantage relative to its direct gap counterparts. Many III-V (and II-VI) materials are direct gap semiconductors and couple strongly to light. Interest in research, such as presented here, into the interaction of polarised light with III-V's for the purpose of manipulating spin information, has thus grown rapidly over recent years. Gallium Arsenide has been the prime focus and other materials such as InAs, InP, and GaN are also under increasingly intense investigation.

It is not only potential further technological reward that motivates spin studies in semiconductors, they also provide an ideal physical system in which to test and improve understanding of physical theories. This is because physical parameters, such as alloy concentrations, temperature, quantum confinement lengths, disorder, and strain to name a few, can be systematically varied with reasonable accuracy and effort during experimentation or growth. Theories attempt to relate these parameters to basic physical processes and measurement results, experiments verify (or contradict) the predictions, and through a feedback process fundamental understanding can increase and deepen.

The work presented in this thesis is a contribution to this field, the ongoing investigation of the properties and behaviour of electrons in III-V semiconductors, with emphasis on the time-resolved dynamics of optically created transient spin polarisations in quantum confined heterostructures.

Laser pulses of ~2 picosecond duration were used to excite a non-equilibrium electron distribution into the conduction band. Optical polarisation of the laser beam is transferred into polarisation of the electron spin. Evolution of this injected spin polarisation was measured using a reflected, weaker, test pulse whose arrival at the sample was delayed. Rotation of the linear polarisation plane of the test pulse revealed some information concerning the state that the spin polarisation had reached after elapse of the delay time. A more detailed description of the measurement method is given in chapter 3.

Three pieces of experimental work have been undertaken in this thesis. Measurements in a high mobility modulation n-doped (1.86×10^{11} cm^{-2}) GaAs/AlGaAs sample were designed to observe the precession of electron spin in the absence of an external magnetic field (see chapter 4). The spin vectors are thought to precess around an effective magnetic field related to the conduction band spin-splitting which is caused by the inversion asymmetry of the Zincblende crystal structure. Spin relaxation in an undoped $In_{0.11}Ga_{0.89}As$/GaAs sample was studied to ascertain whether previously observed fast electron spin relaxation in InGaAs/InP was due the native interface asymmetry present in the structure or if spin relaxation is generally fast in InGaAs wells (see chapter 5). Finally, quantum beating of exciton spin precession was measured in a GaAs/AlGaAs multiple quantum well sample with a magnetic field applied at various angles to the growth and excitation direction using optically-induced transient linear birefringence. Previous studies on this sample have shown that some of the excitons experience a low symmetry environment which lifts the degeneracy of the optically active heavy-hole exciton spin states. In this study we attempt to observe the effects of this in time-resolved spectroscopy (chapter 6).

In chapter 2 some basic semiconductor physics relating to the behaviour of electrons is outlined in sufficient detail to give some perspective to the work presented in subsequent chapters.

2. Electrons in III-V semiconductor heterostructures

The relation between the electron kinetic energy (E) and momentum ($\underline{p}$) is called the dispersion function and its form can explain many of the properties of electrons in semiconductors. In free space, ignoring relativistic effects, it is the familiar parabolic function:

$$E = p^2/(2m_0), \tag{2.1}$$

where m_0 is the electron rest mass. When the electron moves through a material the dispersion function is modified through interaction with the electromagnetic fields of particles that compose the material. Its exact form depends on the material system considered and in general it is a complicated function of many interactions and factors. For small values of $\underline{p}$ the experimentally determined dispersion relation in direct gap III-V semiconductors is well approximated by a set of parabolic bands with modified particle masses. It should be noted that the manifold p is not continuous, it forms a quasi-continuum where the distance between each discrete state labelled by p is small enough to ignore and can be treated as a continuous variable in most practical work. It is convenient to focus on the wave nature of electrons inside the lattice and use the electron wave vector, $\underline{k} = \underline{p}/\hbar$. Within the parabolic approximation, electrons in the conduction band have energies (measured from the top of the valence band):

$$E= (\hbar^2k^2)/(2m_em_0) + E_g, \tag{2.2}$$

where m_e is the effective electron mass ratio. E_g is the band gap, a region of energy values which electrons cannot possess. In the valence band, the functions can be approximated by the solutions of the Luttinger Hamiltonian [1]:

$$H = (\hbar^2/(2m_0)).[(\gamma_1+\gamma_2 5/2)k^2 - 2\gamma_2(k_x^2 J_x^2 + k_y^2 J_y^2 + k_z^2 J_z^2) - 4\gamma_3(\{k_x.k_y\}\{J_x.J_y + \ldots\})], \quad (2.3)$$

where γ_n are the Luttinger parameters which define the valence band, {A.B} is the anticommutation operator (AB + BA), and J_i is the i'th component of angular momentum. Solutions of the Hamiltonian depend on the propagation direction. Defining the z-direction along the [001] crystal direction and considering electrons propagating along it reveals two dispersion relations, of the light and heavy-hole valence bands according to J_z having values ±1/2 and ±3/2 respectively:

$$E= (\gamma_1+2\gamma_2).(\hbar^2 k_z^2)/(2m_0) \quad J_z=\pm 1/2 \text{ (light-electron states)},$$
$$E= (\gamma_1-2\gamma_2).(\hbar^2 k_z^2)/(2m_0) \quad J_z=\pm 3/2 \text{ (heavy-electron states)}, \quad (2.4)$$

thus electrons with $J_z=\pm 1/2$ move with effective mass $m_0/(\gamma_1+2\gamma_2)$ and those with $J_z=\pm 3/2$ with effective mass $m_0/(\gamma_1-2\gamma_2)$.

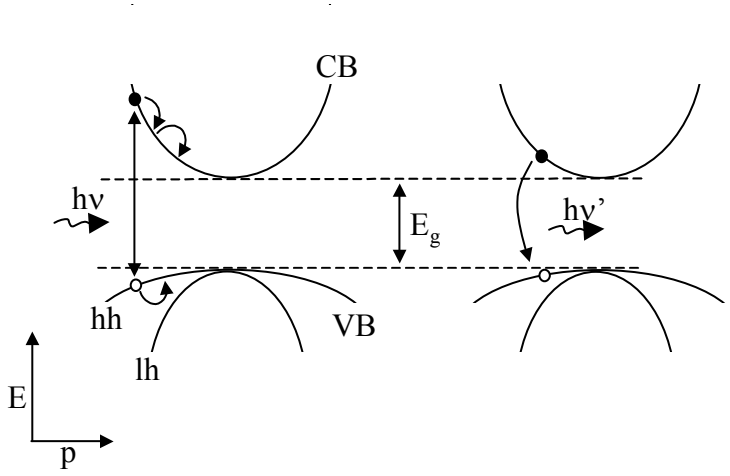

Figure 2.1: Basic band structure and absorption/emission process in a direct gap semiconductor. Light of energy hν is absorbed promoting an electron to the conduction band and leaving a hole in the valence band, the particles relax towards the band minima and eventually recombine emitting a photon with less energy.

Absorption of light in un-doped samples occurs for photon energies (hν) greater than the band gap (E_g), resulting in the promotion of an electron from the valence to conduction band leaving a hole (an unfilled state) in the valence band. The conduction electron will generally lose energy by emission of phonons, ending near the bottom of the conduction band. Similar phonon emission by the electrons in the valence band gives the appearance that the hole moves towards the top of the band. Holes may be either `light` or `heavy` according to their angular momentum being $J_z=\pm 1/2$ or $J_z=\pm 3/2$ respectively. The electron and hole may eventually recombine; the electron falls back to the valence band, the hole disappears, and a photon of altered energy hν' is emitted, the process is illustrated in figure 2.1. By momentum conservation and because the photon momentum is negligible, the electron and hole must have wave vectors of roughly equal and opposite magnitude for absorption/emission to occur. That is, only vertical transitions in E(k) vs. k space are allowed.

The energy gap of a structure is a function of the material composition and mesoscale structure. By alloying different III-V elements the band gap can be engineered, materials can be made strongly transparent or absorbent at different wavelengths. In particular, by substituting Aluminium for Gallium the important $Al_xGa_{1-x}As$ alloy is produced. The potential energy of an electron in this alloy is an increasing function of x and the band gap can be varied from just below 1.5 to above 2 eV as x varies from 0 to 1. However, $Al_xGa_{1-x}As$ becomes an indirect semiconductor, where the conduction band minimum does not occur at the same wavevector as the valence band maximum, for x greater than 0.45 and interaction with light is weakened considerably.

Characteristically different behaviours of the electrons can be tuned by varying the equilibrium concentration of electrons in the conduction band via doping. An intrinsic sample is characterised by an empty conduction and a full valence band at low temperature in the

unexcited state. Within such a sample, as studied in chapter 5, the Coulomb attraction between the electron and hole modifies behaviour through the formation of excitons under most excitation conditions and particularly at low temperatures. Adding dopant atoms during growth which carry extra outer shell electrons (n-doping) results in the occupation of some conduction band states at low temperature, up to and defining the Fermi energy. In n-type samples electrical conduction is higher and formation of excitons is less probable, though through the transition from intrinsic to n-type many interesting phenomena occur such as exciton screening and the formation of charged excitons. Non-equilibrium electrons in n-type samples occupy higher conduction band energies than in undoped samples and experience important effects such as exposure to increased conduction band spin splitting (which increases with the electron energy), the subject of chapter 4. p-doping is the process of adding dopant atoms that are deficient in outer shell electrons which create extra states for the valence band electrons to occupy, resulting in the creation of holes in the valence band which are present at low temperature in the unexcited state.

Potential wells can be formed by growing a layer of GaAs between two layers of $Al_xGa_{1-x}As$. Within such a structure the electrons and holes become trapped in the GaAs layer where they have a lower potential energy, figure 2.2. If the thickness of the GaAs confining layer is of the order of the de Broglie wavelength then quantum effects become evident in the electron and hole behaviours, the most relevant (to this work) of which are the quantisation of the electron motion perpendicular to the layers and degeneracy breaking between the heavy and light-hole valence bands.

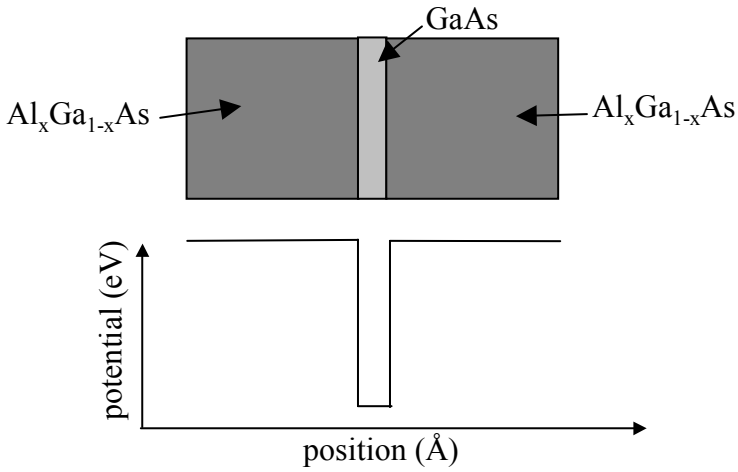

Figure 2.2: Simplified schematic of a type-I semiconductor heterostructure. Dark rectangles indicate AlGaAs layers and the light grey represents a GaAs quantum well layer. The plot illustrates the variation of electron (and hole) potential energy as a function of position in the structure, at low temperatures the electrons and holes are confined in the quantum well layer.

Confinement lifts the energies of the bands by different amounts, its effect on the valence band states can be separated into three stages:

1) The bands are shifted by the confinement energies, resulting in lifting of hh-lh degeneracy.

2) When confinement is included in the Luttinger Hamiltonian as a first order perturbation the hole masses change, the $J_z=\pm 3/2$ mass becomes $m_0/(\gamma_1+\gamma_2)$ which is lighter than the new $J_z=\pm 1/2$ mass of $m_0/(\gamma_1-\gamma_2)$ and the bands would be expected to cross at some finite wavevector.

3) Inclusion of higher orders of perturbation in the theory results in an anti-crossing.

Weisbuch [1] discusses the confinement effect on the valence band effective masses in greater detail.

Motion of electrons inside one-dimensionally quantum confined heterostructures separates into two parts. Motion along the plane of the structure remains quasi-continuous and is characterised by a two-dimensional continuous wave vector, but the wave vector in the confinement direction becomes quantised and only discrete values are allowed. For infinitely deep wells (i.e. taking the electron potential energy in the barrier material to be infinite), the electron and hole energies are raised by the confinement effect and form the discrete set:

$$E_n(\underline{k}) = (n\pi \hbar/ L_z)^2/(2m^*), \qquad (2.5)$$

where m^* is the effective mass of the particle, L_z is the confinement length and n is the principal quantum number of the state. Because the heavy and light-holes have different effective masses for motion in the z-direction, quantum confinement removes the degeneracy of the $J_z=\pm1/2$ and $J_z=\pm3/2$ hole states. The particle wave functions are sinusoidal in the well material:

$$\varphi_n(z) = A.\sin(n\pi z/L_z), \qquad (2.6)$$

and are zero in the barriers, they are illustrated in figure 2.3.

If finite barrier heights are considered then the confinement energies are solutions of the transcendental equation:

$$\tan((2m_z^*E_n/ \hbar^2)^{1/2}L_z/2 - \pi/2) = -(E_n m_z^{*1}/ (m_z^*[V - E_n])), \qquad (2.7)$$

where m_z^* and m_z^{*1} are the effective masses for motion along the growth direction in the well and barrier material respectively and V is the barrier height. The particle wave functions are sinusoidal inside the well and decay exponentially in the barriers, the amount of wave function penetration into the barrier increases for narrower wells. Motion of electrons in the layers results in a parabolic dispersion (equation 2.2) with the confinement energy added on. For holes with small in-plane wavevector the dispersion can be characterised by similar parabolic

relations, but when this is large the $J_z=\pm1/2$ and $J_z=\pm3/2$ states are no longer eigenstates of the Luttinger Hamiltonian and valence band mixing with anti-crossing becomes important.

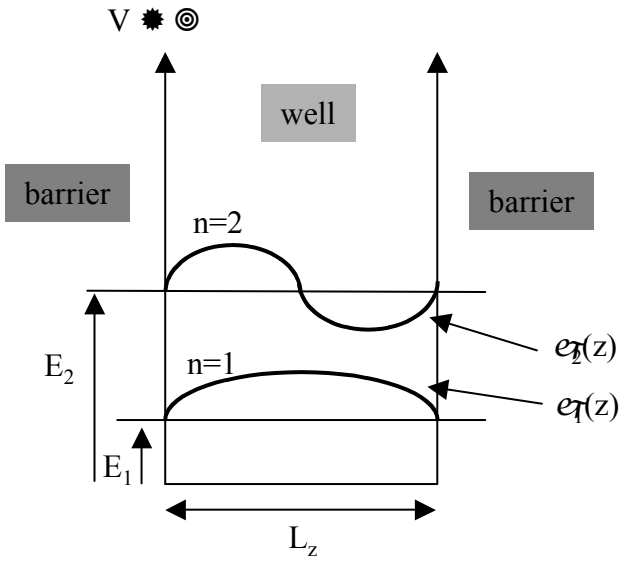

Figure 2.3: Schematic of the quantum confinement energies and wave functions in the growth direction in an infinite barrier quantum well. The first confined state is cosinusoidal and has a minimum energy that is of magnitude E_1 greater than the minimum energy of the particle in the absence of the barriers.

It is clear that an effect of quantum confinement is to raise the band energies in the well material by different amounts for the electron, heavy- and light-hole respectively of E_{1e}, E_{1hh} and E_{1lh}, figure 2.4. This allows tuning of the band gap by variation of L_z and barrier height. The difference in E_{1hh} and E_{1lh} has fundamental implications to optical polarisation effects.

Electrons in the conduction band have angular momentum (S) of 1/2 and can have components (s_z) of +1/2 or -1/2 projected along the growth direction. Holes in the valence

bands have J of 3/2 and thus possess four orientations of the z-component of angular momentum (J^h_z). Heavy-holes have possible J^h_z values of +3/2 and -3/2 and light-holes have +1/2 and -1/2. In addition there is a spin-orbit split-off band with a J value of 1/2, but the splitting is 340 meV in GaAs compared to energy scales relevant to this work of tens of meV or less, so the split-off band is neglected.

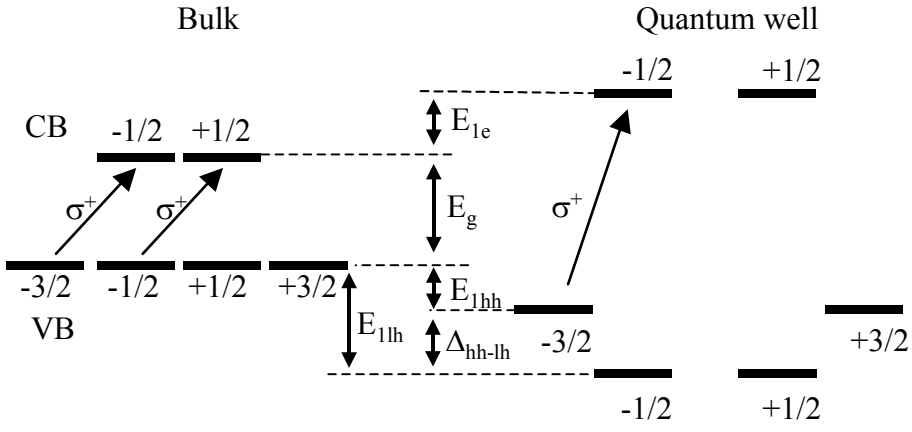

Figure 2.4: Schematic diagram illustrating the effects of quantum confinement on the energy structure of the electron and hole spin states at the zone-centre ($\underline{k} = 0$) in direct gap zinc-blende III-V semiconductor materials. E_g is the fundamental band-gap of the well material, E_{1e}, E_{1hh} and E_{1lh} are the confinement energies of the 1s electron and lowest hh and lh states. $\Delta_{hh\text{-}lh}$ is the heavy-light-hole splitting induced by confinement, which enables optical creation of 100 % spin polarisation in the conduction and valence bands through excitation with circularly polarised light of energy $E_g+E_{1e}+E_{1hh}$. The fractional numbers are the z-components of orbital angular momentum (spin) quantum numbers.

Light absorption causes the promotion of an electron from a valence band state to a conduction band state. Because the photon linear momentum is small, the net momentum transfer to the carriers is negligible and only vertical transitions are allowed. The light polarisation satisfies the angular momentum conservation:

$$m_p = J^h_z + s_{z,} \qquad (2.8)$$

where m_p is the angular momentum of the photon, and can take the value +1 or –1 for the two circular polarisations. Because the heavy and light-hole states are degenerate at the zone centre in bulk material, absorption of circularly polarised light (σ^+ say) excites electrons from both the heavy and light valence bands, populating simultaneously the spin up and down conduction band states which results in only partial electron spin polarisation. The states are also strongly mixed so that a population of holes with J^h_z value of 3/2 relax quickly to a mixture of 3/2, -3/2, 1/2 and –1/2 J^h_z values.

Lifting of the heavy-light-hole degeneracy by quantum confinement unmixes the hole states with J^h_z values of ±3/2 and ±1/2, and they become energy selectable at the zone centre allowing optical excitation of complete electron spin polarisation in the conduction band. The heavy-light-hole valence band mixing is still present but is moved away from the zone centre (to finite $\underline{k}$). This has implications for hole and exciton spin relaxation.

Attraction between the electron and hole via the Coulomb interaction leads to hydrogenic states (excitons) in which the electron and hole motions are strongly correlated. In such states, the electron and hole relative motion is characterised by their mean separation a_0, the exciton Bohr radius. Excitons are important at low temperatures in undoped sample. At high temperatures they are unstable because of the high number of optical phonons which can ionise them in a single collision. Their effects in spin dynamics are investigated in chapters 5 and 6.

The centre-of-mass motion of the electrically neutral exciton can be represented by a plane wave. The observed discrete spectral lines below the fundamental absorption edge, and the enhancement factor to the absorption coefficient above the band gap (the Sommerfeld factor), can both be explained by considering the effects of exciton states. One-dimensionally confined exciton wave functions are slightly elongated and the mean radius decreases as the confinement length decreases below a_0. Subsequently, the increased overlap of the electron and hole wave functions increases the exciton stability and spin-exchange interaction strength. Extreme confinement results in barrier penetration of the exciton wave function. Heavy-hole excitons can be resonantly created through excitation with light of energy:

$$E_x = E_g + E_{1e} + E_{1hh} - E_B, \qquad (2.9)$$

where E_B is the exciton binding energy. Figure 2.5 illustrates the relative magnitudes of these energies calculated for a quantum well studied in this work (chapter 5). Note that alloying GaAs with Indium lowers rather than increases the electron potential energy and so in this system it is the InGaAs alloy that forms the well material.

Just as for hydrogen atoms, a Rydberg-like series of discrete energy states extending from E_X to E_X+E_B exists for the exciton. The lowest-energy unbound state (exciton principal quantum number, n, of ∞) corresponds to electrons and holes with purely two-dimensional plane wave character in the well material at energy E_{1e}. For an infinitely deep well, motion is exactly two-dimensional and E_B is equal to R_{2D}, the two-dimensional exciton Rydberg energy which is related to the three-dimensional Rydberg energy (R_{3D}) by equation 2.10. n is the principal quantum number of the binding state (not to be confused with that for the electron confinement), ε_r is the relative permittivity of the well material and R_y is the Rydberg constant with value 13.6 eV.

$$E_B = R_{2D} = R_{3D}/(n - 1/2)^2, \qquad (2.10)$$

$$R_{3D} = R_y(1/m_e + 1/m_h)/(m_0.\varepsilon_r^2). \qquad (2.11)$$

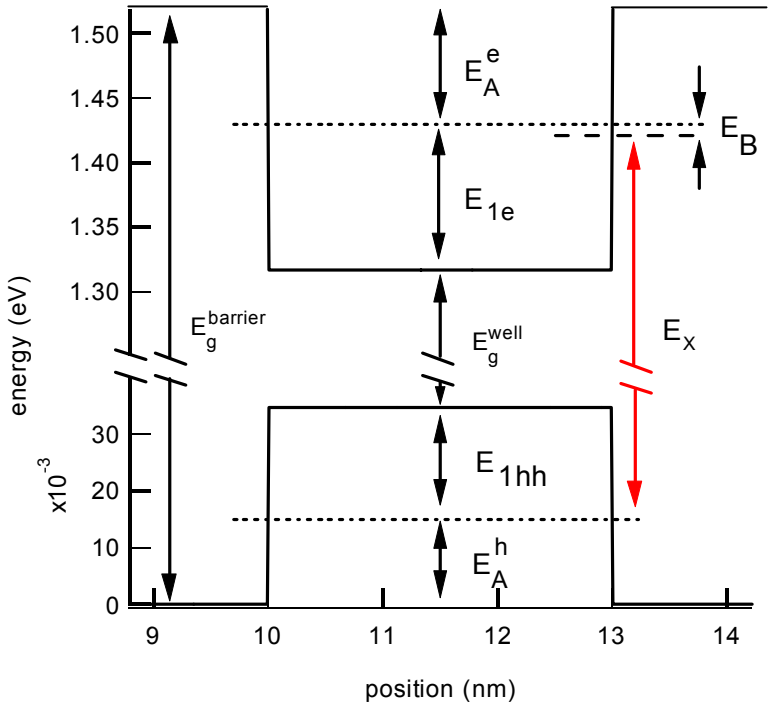

Figure 2.5: Scaled diagram of some important energies in an undoped quantum well showing the band-gaps of the barrier and well, $E_g^{barrier}$ and E_g^{well}, the exciton resonant excitation energy E_X, the heavy-hole and electron confinement and activation energies, E_{1e}, E_{1hh}, E_A^h and E_A^e respectively. Actual values are those calculated for the 30 Å $In_{0.11}Ga_{0.89}As/GaAs$ well of sample DB918 (chapter 5).

Further discussion of fundamental semiconductor band structure theory and other topics introduced in this chapter appear in many textbooks and details of some useful texts are given below.

1. **"Quantum semiconductor structures, fundamentals and applications"**, C. Weisbuch, B. Vinter, *Academic Press Inc (1991)*.

2. "Monographies De Physique: wave mechanics applied to semiconductor heterostructures", G. Bastard, *Les editions de physique (1992)*.

3. "Survey of semiconductor physics: electrons and other particles in bulk semiconductors", K. W. Böer, *Van Nostrand Reinhold (1990).*

4. **"Optical nonlinearities and instabilities in semiconductors"**, edited by H. Haug, *Academic Press (1988)*.

5. **"Ultrafast spectroscopy of semiconductors and nanostructures"**, J. Shah, *Springer (1998).*

6. **"Optical Orientation, Modern Problems in Condensed Matter Science"**, edited by F. Meier and B. P. Zakharchenya, North-Holland, Amsterdam (1984).

3. Time-resolved measurement method

The time-resolved experimental arrangement used in this work is described here (see figure 3.1). Key elements are: the use of balance detection, which eliminates noise due to laser power fluctuations; and chopping of the pump and probe beams at different frequencies combined with lock-in detection at the sum frequency, which reduces noise sources that affect the beams independently. Extra apparatus or principles that are specific to a particular experiment will be mentioned in the chapter pertaining to that work.

Samples were held either in a variable temperature insert (VTI) cryostat which contained an 8-Telsa magnet or in a gas flow cryostat. The VTI allowed maintenance of sample temperatures from below 2 K up to 300 K with the magnet remaining immersed in liquid Helium and thus super conducting. The gas flow cryostat allowed a similar temperature range but did not contain a magnet, it was physically smaller and much less cumbersome to manipulate and cool. A mode-locked Ti:Sapphire laser system was used to generate pulses of width of ~2 ps at a rate of 76 MHz corresponding to a pulse separation of ~13 ns. It was readily tuneable over the range of 680-1100 nm.

With reference to figure 3.1, the beam from the Ti:Sapphire laser was attenuated with a variable neutral density filter (ND), and passed through a beam splitter (BS1). Transmitted and reflected components through this element are termed the pump and probe beams respectively. Each was reflected from a corner cube (CC1 and CC2) and directed through the outer and inner holes of an optical chopper wheel respectively, which had different hole spacings and modulated each component at a different frequency. CC1, which reflected the probe beam was mounted on a delay line driven by a computer controlled stepper motor. Positioning of this

corner cube allowed the delay of the probe pulse train relative to the pump pulse train to be altered in steps of 0.1 ps at variable speeds; the maximum available delay was ~3 ns.

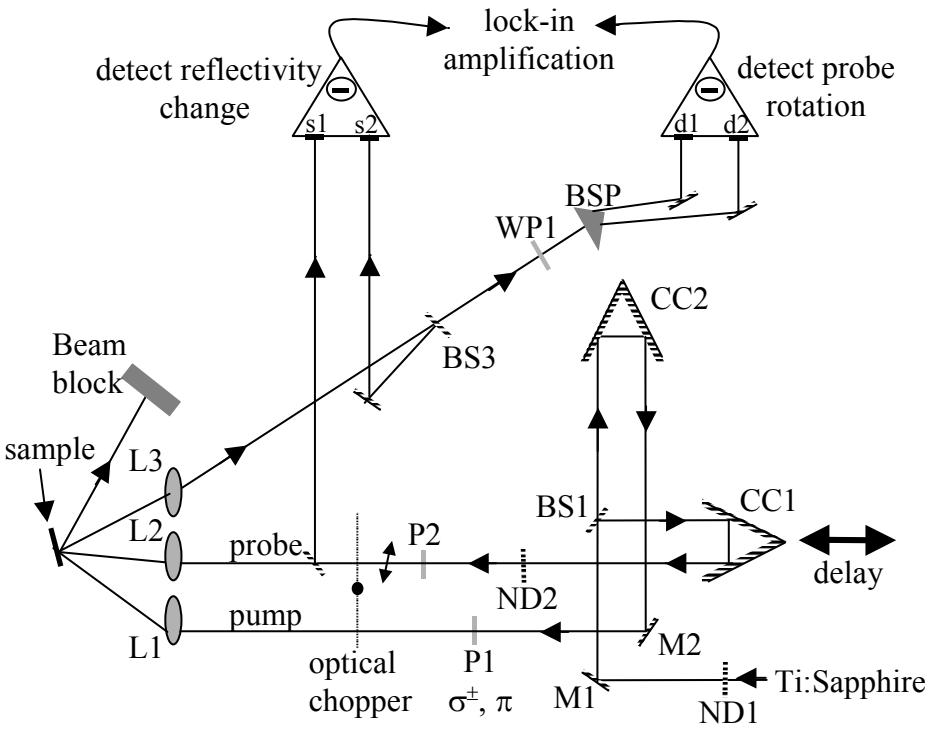

Figure 3.1: Schematic of experimental arrangement for time-resolved measurement, the labelled elements (Mirror (M), Beam Splitter (BS), Neutral Density filter (ND), Corner Cube (CC), Lens (L), Polariser (P), Wave-plate (WP) and Beam Splitting Prism (BSP)) are discussed in the text. Angles of beams incident on sample are greatly exaggerated and were actually less than 3^{o}.

In all of the experiments the probe beam was linearly polarised by element P2. Polarisation of the pump beam was set by element P1 as circular ($\sigma^{\pm}$) or linear (π), arbitrary polarisation angle relative to the probe was possible. ND2 allowed attenuation of the probe intensity independently of the pump. In order to guide the reflected probe beam through the detection optics the sample was rotated, but the angle of incidence of the beams on the sample surface

were less than 5^o. However, the internal angle of incidence was much less than this, by a factor of around 3.5, due to the high refractive index of GaAs. Care was taken to eliminate scattered light from the pump beam from entering the detection optics, for example by placing an iris around the reflected probe beam.

The reflected probe beam was collimated using L3 and passed through BS3, set almost normal to the beam direction in order to avoid polarisation sensitivity of the reflected component, and directed into one arm of a balance detector via a mirror. Part of the probe beam (the reference component) was picked off by reflection from BS2 set at ~45^o to the beam direction, placed between the chopper and the sample. It was directed into the other arm of the balance detector. It is the pump induced change in the relative intensity of these two beams that is referred to as the sum signal, the reflectivity change, or ΔR.

The component of the probe reflection from the sample transmitted through the BS3 was passed through a rotatable half-wave plate, then onto a Calcite birefringent prism. The prism has different refractive indices for polarisations parallel and perpendicular to the apex. They therefore emerge at different angles. The components were directed onto the photodiodes of a second balance detector; the pump induced change in the relative intensity of these two components is referred to as the difference signal, the probe polarisation rotation, or $\Delta\theta$.

Signals were measured using lock-in amplification at the sum of the pump and probe modulation frequencies and thus were composed only of the changes induced on the probe pulse by the remnants of the interaction of the pump pulse with the sample. Frequencies were chosen to avoid noise sources such as integer multiples of 50 Hz. The chop frequency was typically of the order of 880 Hz for the probe and 1.15 kHz for the pump. Balance detection was used to eliminate noise due to laser power fluctuations.

The electric field components of a general elliptically polarised beam can be expressed as:

$$E_x \sim [\cos(\omega t)\cos(\theta`) + \cos(\omega t + \varepsilon)\sin(\theta`)]/\sqrt{2}$$

$$E_y \sim [-\cos(\omega t)\sin(\theta`) + \cos(\omega t + \varepsilon)\cos(\theta`)]/\sqrt{2} \qquad (3.12)$$

$$\theta` = \theta - \pi/4.$$

In this representation, ω is the optical frequency of the light, θ the angle of the plane of polarisation relative to the y-axis (vertical direction) measured in a clockwise sense, and ε is a parameter describing the ellipticity. A zero value of ε corresponds to perfect linearly polarised light, a value of $\pi/2$ corresponds to circular polarisation and values in between to varying degrees of ellipticity as illustrated in figure 3.2.

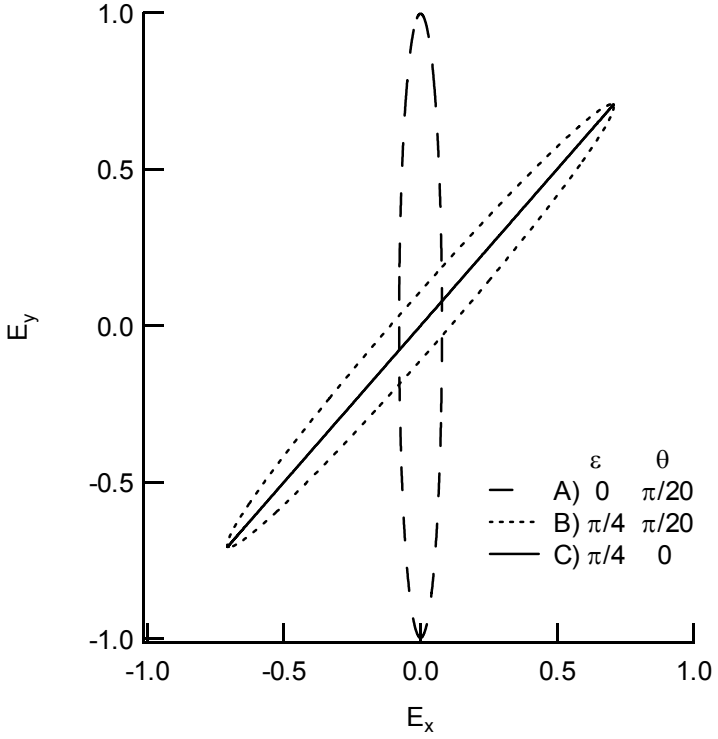

Figure 3.2: Electric field components for different ellipticities and polarisation angles, where (θ, ε) have values: A. (0, 20), B. (π/4, 20) and C. (π/4, 0).

Light passing through the birefringent prism (labelled BSP in figure 3.1) was split into its two orthogonal linear components, the difference in their intensity that was detected by the balance detector can be modelled by:

$$D \sim - \cos(\varepsilon).(\sin^2\theta - \cos^2\theta)/2. \qquad (3.13)$$

Since the detector responded much slower than the optical frequency the average signal over an optical cycle was measured.

Figure 3.3 shows the modelled output of the difference detector as a function of polarisation angle for three different ellipticities. When the light is 100 % circular the response is completely insensitive to the polarisation angle. Maximum sensitivity ensues when the probe is linearly polarised.

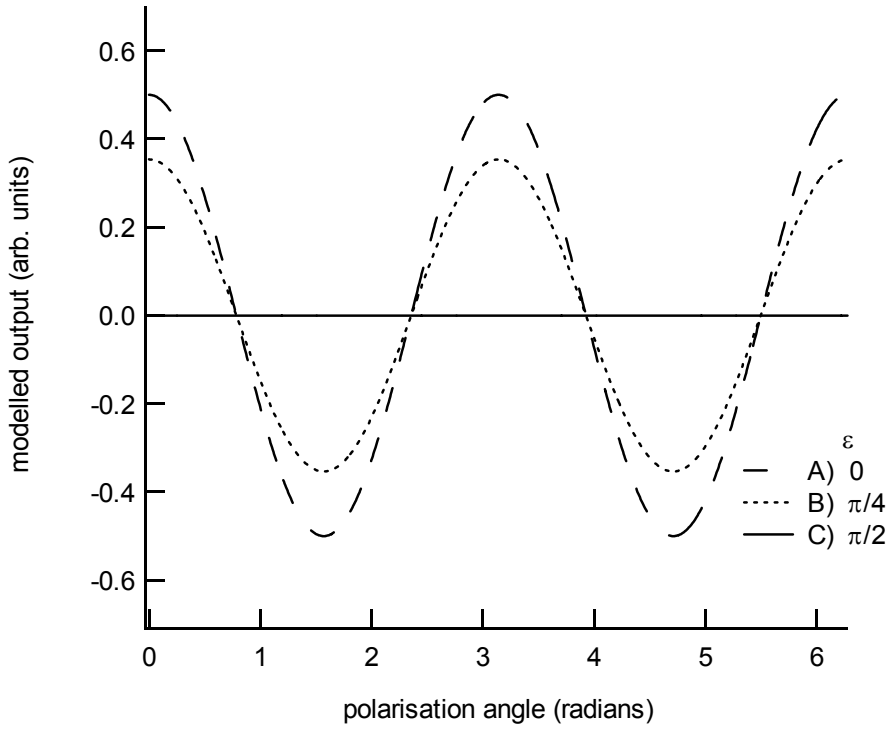

Figure 3.3: Difference detector response as a function of light polarisation angle for different ellipticities (ε): A. 0, B. π/4, C. π/2.

To initialise the experiments the pump beam was blocked and the half-wave plate rotated to nullify the output of the balance detector (effectively setting θ to π/4).

In order to quantify what is measured by the difference detector, consider the induced change in the value of the function $D(\theta,\varepsilon)$, δD_θ brought about by a change in the angle θ, δθ:

$$\delta D_\theta \equiv D(\pi/4 + \delta\theta) - D(\pi/4) = -2\delta\theta\cos(\varepsilon). \quad (3.14)$$

It is clear that maximum sensitivity to induced probe rotation should occur when the probe is as close to linearly polarised as possible (zero value of ε). Consider now the change in the value of $D(\theta,\varepsilon)$, δD_ε induced by a change in the value of ε , δε:

$$\delta D_\varepsilon \equiv (\partial D/\partial\varepsilon)\delta\varepsilon = \delta\varepsilon.\sin(\varepsilon).(\sin^2\theta - \cos^2\theta). \quad (3.15)$$

As long as the system is balanced correctly and induced rotations are small then θ will remain infinitesimally close to π/4 and the $\sin^2\theta$-$\cos^2\theta$ factor vanishes so that:

$$0 \approx \delta D_\varepsilon << \delta D_\theta \quad (3.16)$$

This shows that the system is insensitive to induced elliptisation of the probe beam to first order and the difference signal, Δθ, measures δD_θ.

Output of the sum balanced detector was insensitive to the polarisation state of the probe. It measured the difference in intensities of the reference beam and the beam reflected from the sample, ΔR.

4. Electron-electron scattering and the D'Yakonov-Perel mechanism in a high mobility electron gas

4.1 Introduction

Electron spin evolution in III-V semiconductor quantum wells is governed by the D'Yakonov-Perel mechanism [1, 2, 3] in which spin relaxation is induced by precession between scattering events in the effective magnetic field represented by the conduction band spin-splitting. The spin relaxation rate is predicted to be proportional to the electron momentum scattering time, τ_p^*, which has been commonly assumed to be proportional to the electron mobility. In samples of low mobility (strong scattering) this predicts that the spin polarisation will decay exponentially, but when mobility is sufficient (weak scattering) the same mechanism should lead to oscillatory dynamics.

This chapter describes measurements of electron mobility, concentration and spin evolution in the high mobility two-dimensional electron gas (2DEG) of a 100 Å GaAs/AlGaAs modulation n-doped single quantum well sample with the aim of testing these predictions. We have developed a Monte-Carlo simulation of the spin evolution to extract values of the scattering time, τ_p^*, from our data. The high mobility and its weak temperature dependence in our 2DEG led to the expectation of oscillatory behaviour up to temperatures of ~100 K. However, the measurements at the Fermi energy revealed heavily damped oscillations only at the lowest temperature (1.8 K) and exponential decay otherwise.

The reason for this discrepancy is that the scattering time τ_p^* from spin evolution is different and generally much shorter than the transport scattering time τ_p from the mobility. At low temperatures the τ_p obtained from the measured mobility of our sample does approach τ_p^*, but the two rapidly deviate with increasing temperature.

We suggest that in high mobility samples it is the electron-electron scattering which limits the spin evolution and must be used in spin evolution theories applied to high mobility electron systems. Electron-electron scattering does not affect the mobility, is infrequent at low temperature and increases rapidly as the temperature is raised; these properties are similar to those of our measured τ_p^*.

Parallel to publication of our experimental work and a preliminary theory [4], Glazov and Ivchenko [5] showed theoretically the role of Coulomb scattering on spin relaxation in non-degenerate two-dimensional electron gases. Subsequently Glazov and Ivchenko et al. [6] published an extension of the theory to degenerate gases, showing good quantitative agreement with our results and adding further evidence to confirm the influence of electron-electron scattering on spin processes.

The chapter begins with sections on the background and theory of spin evolution followed by description of the sample, experimental technique and results. Finally we describe our analysis of the data.

4.2 Background

Future devices that exploit spin may require electron systems which simultaneously possess a long spin memory and high mobility, it may also be useful to have devices in which spin polarisation is lost rapidly. For 2DEG's in Zincblende semiconductor heterostructures however, the spin relaxation rate theoretically increases with mobility [1, 2] and it ought not be possible to maintain arbitrary mobility and spin memory simultaneously.

Experimental studies of electron spin relaxation in n-doped quantum wells have been rare and have focused on high temperatures (above 100 K) in samples of low mobility (typically below 6.10^3 $cm^2V^{-1}s^{-1}$) [e.g. 7, 8]. Commonly, the momentum scattering time determined by Hall mobility measurements has been used as the relevant scattering parameter in application of the spin relaxation theories. For low mobility electron gases this is valid because the momentum scattering is significantly faster than the electron-electron (Coulomb) scattering.

Three mechanistic descriptions of electron spin relaxation in III-V semiconductor heterostructures have become prominent. For the structure under study in this chapter the Bir-Aronov-Pikus [9] and Elliot-Yafet [10, 11] mechanisms are weak and the leading mechanism is that of D'yakonov, Perel and Kachorovskii [1, 2]. Within the Bir-Aronov-Pikus mechanism electrons relax their spin polarisation due to electron-hole scattering in an exchange process; this mechanism is inefficient in n-doped samples under weak photo excitation conditions where the hole density is low. The Elliot-Yafet mechanism considers coupling between the conduction and valence bands which can lead to electron spin relaxation; this mechanism should be inefficient in GaAs/AlGaAs quantum wells [12].

The D'yakonov-Perel theory proposes firstly that electron spin depolarisation occurs due to precession around the effective magnetic field induced by motion through the inversion asymmetric Zincblende crystal structure, which also causes the conduction band spin-splitting; and secondly, that scattering of the electron wavevector randomises somewhat the value of this field for each electron, causing a motional slowing of the rate of spin depolarisation. Spin dynamics of electrons in Zincblende crystals are thus heavily perturbed by conduction band spin-splittings caused by inversion asymmetries in their environment [13] which, with high scattering rates, leads to the strongly motionally slowed evolution characterised by exponential decay.

Temperature has two major effects on the 2DEG. It determines the mobility, which decreases with increased temperature due to stronger lattice deformation and impurity scattering. It also alters the Coulomb scattering rate, which for a degenerate gas vanishes at low temperature [14, 15, 6]. Coulomb scattering within the gas does not reduce the mobility but it ought, in addition to mobility scattering, to be effective in the D'yakonov-Perel mechanism which inhibits relaxation of the electron spin. This point had been overlooked until the work we describe here.

4.3 Theory

4.3.1 Conduction band spin-splitting and the D'yakonov-Perel mechanism

Inversion asymmetry in the zinc-blende crystal structure and spin-orbit coupling lift the spin degeneracy [13] for electron states of finite wave vector ($\underline{k}$). The spin-splitting can be represented by an effective magnetic field vector acting on the spin part of the electron wave function whose value, in particular its direction, is a function of $\underline{k}$. In heterostructures there can be additional contributions to asymmetry; that (already mentioned) associated with the intrinsic crystal structure is termed the Bulk Inversion Asymmetry and is commonly referred to as the Dresselhaus term. Structural Inversion Asymmetry, commonly called the Rashba term, arises in the presence of electric fields across the electron gas, generated for example by one-sided modulation doping or gating. Bonds between non-common anions across the barrier/well interface lead to the Native Interface Asymmetry; it is not present in the GaAs/AlGaAs structure studied in this chapter and its significance is still under investigation (see for example reference 19). In chapter 5 we show that it is the likely cause of previously observed [12, 16] fast spin relaxation in InGaAs/InP quantum wells. The original work by D'yakonov, Perel and Kachorovskii [1, 2] considered Bulk Inversion Asymmetry terms alone. Improved theoretical and experimental values for the strength of the effective field have been published which

include the Structural Inversion Asymmetry contribution and are given by Lommer [17] for <100> growth direction as:

$$\underline{\Omega}(\underline{k}) = 2/\hbar\{[a_{42}k_x(\langle k_z^2\rangle - k_y^2) - a_{46}E_z k_y]\underline{i} + [a_{42}k_y(k_x^2 - \langle k_z^2\rangle) + a_{46}E_z k_x]\underline{j}, \qquad (4.1)$$

where a_{42} and a_{46} are material dependent constants with values $1.6\text{x}10^{-29}$ eV m^3 [18] and $9.0\text{x}10^{-39}$ Cm^2 [17] respectively in GaAs, E_z is the electric field along the growth direction and $\underline{i}$ and $\underline{j}$ are unit vectors in the plane of the well along [001] and [010].

Within the Bir-Aronov-Pikus and Elliot-Yafet mechanisms, electron spin relaxation occurs only due to and during non-spin-conserving scattering events. D'yakonov and Perel proposed that precession of the electron spin vector around the effective field during the time between scattering events should lead to fast spin relaxation [1] - but that momentum scattering events which change the direction of $\underline{k}$ also change at random the direction of the effective field, and thus the axis of precession for each electron randomly reorients at the momentum scattering rate, the effect of the field averaged over time is therefore weakened. D'yakonov-Perel theory applies to bulk (3D) electron systems, D'yakonov and Kachorovskii [2] later extended the theory to quantum wells and 2DEG's. They calculated the appropriate population average of the Bulk Inversion Asymmetry contribution over the growth direction which, for <100> grown wells, leads to an effective magnetic field lying in the plane of the well. It is now more appropriate to use the more recent formula, equation 4.1, which includes the Structural Inversion Asymmetry contribution.

The spin vector of an electron which is initially in a state labelled by $\underline{k}$ with its spin pointing out of the plane will precess towards the plane at a rate $\sim\Omega$, and after some time (on average τ_p^*, the momentum scattering time) it will suffer an elastic collision which alters its wave vector direction at random. A finite component of its spin vector may then, with large probability, begin to precess back out of the plane and in this way the relaxation (precession) of

spin components initially along the growth axis is slowed down by collision events; with frequent scattering the spin vectors have less time between scattering events in which to keep rotating about the same axis before the axis is reoriented. Thus each electron spin vector in effect exercises a random walk in angle space with path length increasing with the momentum scattering time.

Experimental observations are invariably made on an ensemble of spin polarised electrons with some distribution of wave vectors and it is the average of the projection of the spin vectors of the ensemble members that is monitored. In the absence of scattering ($\Omega.\tau_p^* >> 1$) this quantity will oscillate indefinitely with a decay or dephasing due to the bandwidth $\Delta\Omega$ sampled by the wavevector and energy distribution of the electron population. If scattering events are marginally infrequent ($\Omega.\tau_p^* \approx 1$) it will contain additional damping that "wipes-out" the phase coherence of the spin of the ensemble. In the case of frequent scattering ($\Omega.\tau_p^* << 1$) it will decay exponentially at the rate:

$$\tau_s^{-1} = \langle\Omega^2\rangle\tau_p^*, \qquad (4.2)$$

predicted by D'Yakonov and Perel [3], where $\langle\Omega^2\rangle$ is the square of the field strength appropriately weighted over the electron distribution. A peculiar characteristic of this mechanism is that spin relaxes faster in purer samples (longer τ_p^*) that is, spin can be preserved better in "dirtier" samples and at higher temperatures, which can seem counterintuitive.

The quantity $\langle\Omega^2\rangle\tau_p^*$, where $\langle\Omega^2\rangle$ is calculated using perturbation theory and τ_p^* measured, is found to be about an order of magnitude faster than measured spin relaxation rates [19]. Flatté et al. have recently published [7] an improved method of calculating $\langle\Omega^2\rangle$ which takes proper account of the field symmetry and they find good agreement with experiment for a range of low mobility ($\Omega.\tau_p^* << 1$) electron systems.

4.3.2 Evolution of spin polarisation excited in the valance band

Spin polarisation induced in the valance band during photo excitation experiments, carried by non-equilibrium holes, may in general affect spin measurement results obtained in time-resolved measurements. In this section it is argued that in experiments such as presented here, where both excitation and measurement are resonant with the Fermi energy of a 2DEG, the holes energy relax within a time of the order of the pulse width (see figure 4.4) and from then on have a negligible effect on the probe rotation. Results therefore pertain to the spin dynamics of the electrons.

Studies of electron and hole spin relaxation via polarised photoluminescence (PL) measurements using circularly polarised excitation light have been carried out in n- and p-type doped quantum wells. In those experiments [e.g. 20, 21] photo injection was at or above the Fermi energy and detection was at the band edge (those were non-degenerate measurements) where the spin polarisation of the high ambient density of majority carriers due to doping was negligible. The minority carriers were initially 100 % spin polarised and recombined with the majority carriers during and after energy relaxation towards states of zero in-plane wave-vector ($\underline{k}_{\|}$), the luminescence polarisation thus yielded information on the spin relaxation rate of the minority carriers. Time-resolved luminescence measurements [20] in a 75 Å n-modulation doped GaAs/AlGaAs quantum well have shown that the hole-spin relaxation time can be as long as a few nanoseconds in a system with approximately 3 times the electron concentration in the quantum well under investigation here, and in a 48 Å quantum well with 3.10^{11} cm^{-2} doping, hole spin polarisation of 40 % has been shown in recombination luminescence [21]. The present quantum well is 100 Å thick and although valence band mixing can be expected to reduce the hole spin life-time somewhat it can be expected that the holes retain some of their initial spin polarisation throughout the measurements.

In resonant experiments the carriers are still injected at or above the Fermi wave-vector but the polarisation is probed at the same energy. The minority carriers, in the present case the holes, should relax in energy away from the Fermi wave-vector towards the top of the valance band within ~100 fs [14] where they recombine with electrons at the bottom of the conduction band on a time-scale of >1 ns. They ought to have little effect on optical probes tuned to the Fermi energy on time-scales greater than a picosecond as illustrated in figure 4.4. It is therefore the spin-polarisation of the photo-excited part of the majority population that is probed in this time-resolved experiment.

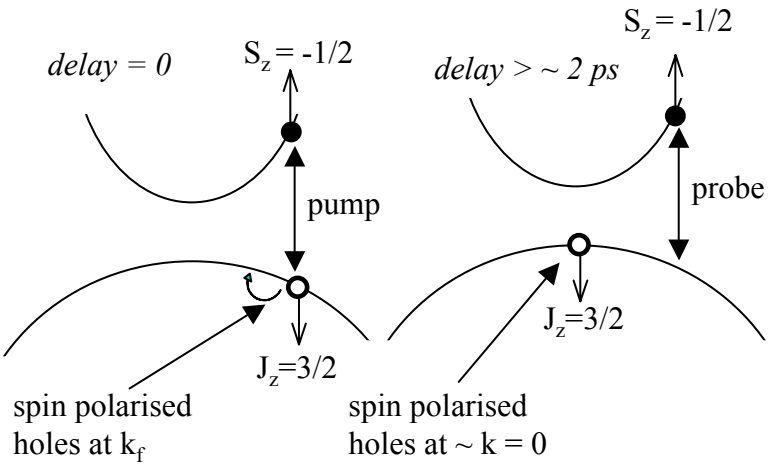

Figure 4.4: Diagram indicating the fast relaxation of the holes which are photoexcited at the Fermi wavevector k_f. The holes may retain their spin polarisation throughout the measurement but they relax to the top of the valance rapidly. The probe is tuned to the Fermi energy and is unaffected by the spin polarised holes at k=0.

4.3.3 Energy distribution of the electron spin polarisation

Conduction band states of opposite spin can be modelled as separate thermodynamic systems [22] with thermal equilibrium achieved via electron-electron scattering. This scattering theoretically vanishes with decreasing temperature for carriers close to the Fermi

energy in degenerate systems. Electron dephasing times, measured in four-wave mixing experiments, of much longer than 40 ps have been observed [14, 15], limited by mobility scattering. The temperature of the thermalised carrier population may be far in excess of the lattice temperature and is a function of excitation energy and power. Under conditions of low power excitation at the Fermi energy the fully thermalised carrier temperature would essentially be that of the lattice.

In two-dimensional systems the density of states (N) of each sub-band is constant with respect to particle energy within the band and for the first confined state is given by:

$$N = 4\pi m^{*}/\hbar^{2}, \tag{4.3}$$

where m* is the effective carrier mass. Their fermionic nature dictates that electrons and holes have a probability of state occupation given by the Fermi-Dirac function:

$$f(E) = 1/\{\exp[(E-\mu_{50})/(k_B T)] + 1\}, \tag{4.4}$$

where μ_{50} is the chemical potential (energy of the state for which there is 50 % chance of occupation) and T is the effective carrier temperature. In 2D systems the chemical potential is found to be an algebraic function (unlike for 3D and 1D systems where numerical solutions are necessary) of the temperature, carrier mass and the carrier density n:

$$\mu_{50} = k_B T.\ln\{\exp[(\pi\hbar^{2}n)/(mk_B T)] - 1\}. \tag{4.5}$$

The value of the chemical potential at zero Kelvin is called the Fermi energy:

$$E_f \equiv \mu_{50}(T\rightarrow 0) = \pi\hbar^{2}n/m. \tag{4.6}$$

As described later in section 4.4 (equation 4.11), E_f can be determined experimentally from the Stokes shift between the low temperature photoluminescence and photoluminescence excitation spectra; along with knowledge of the carrier effective mass, this yields the electron concentration in the system at low temperatures from equation 4.6. The terms chemical

potential and Fermi energy are often used interchangeably, particularly at low temperatures where they coincide.

Absorption of σ^+ (σ^-) circularly polarised pump photons can be modelled as an increase of the chemical potential of the spin-down (spin-up) polarised electron population, with the chemical potential of the opposite polarisation remaining unchanged [22]. Figure 4.5 illustrates the idea for temperatures of 10 and 30 K, the system modelled is a 100 Å quantum well with background doping of 1.86×10^{11} cm^{-2} and a pump injection density of 3.10^9 cm^{-2}, which are similar conditions to those of the experiments presented here, the chemical potential shift of the spin-up electrons has been calculated using equations 4.5 and 4.6.

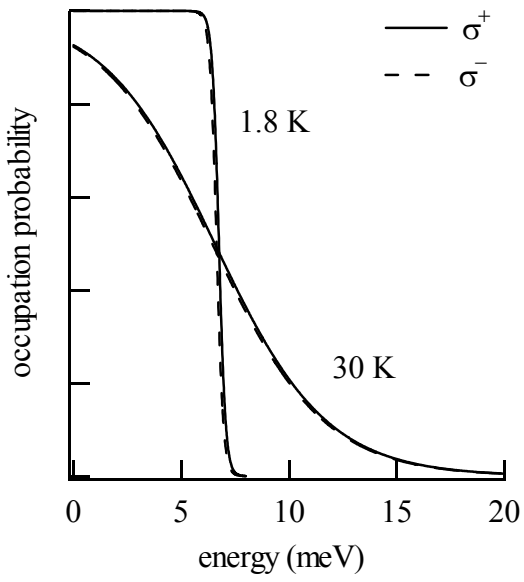

Figure 4.5: Occupation probabilities for electrons in the circularly polarised states of the conduction band after pump pulse injection of 3.10^9 cm^{-2} electrons, the background (gate bias induced) doping is 1.86×10^{11} cm^{-2}. The σ^+ state has an increased Fermi energy of 6.75 meV due to the photo-excitation but the Fermi energy of the σ^- states is unchanged at 6.64 meV.

4.4 Sample description

The sample (T315) studied was a modulation n-doped GaAs/$Al_{0.33}Ga_{0.67}As$ <001>-oriented 100 Å single quantum well molecular beam epitaxy grown at the Cavendish Laboratory Cambridge by Prof. D. A. Ritchie and Dr. D. Sanvitto. It was processed into a device by Dr A. J. Shields of Toshiba research Europe. Further spectroscopic information about the sample is given by them in reference 23. The structure consisted of 1 μm GaAs, 1 μm AlGaAs, 0.5 μm GaAs/AlGaAs superlattice with each layer of thickness 25 Å, the 100 Å GaAs quantum well layer, a 600 Å un-doped AlGaAs spacer, a Si-doped (10^{17} cm^{-3}) 2000 Å AlGaAs layer, follow by a 170 Å GaAs capping layer. The sample had 33 % of Aluminium content of in all AlGaAs layers.

A diagram of the sample is shown in figure 4.6. By changing the electric potential on the semi-transparent Schottky gate (referred to as the gate) the electron concentration in the quantum well, supplied by the dopant layer, can be controlled. The source, drain and Hall contacts are connected to the quantum well layer electrically and allow mobility of the 2DEG in the well to be measured. Throughout the experiments presented in this chapter, the channel (formed by short circuiting the source and drain) was held at 0 V; positive gate potentials drew electrons into the channel whilst negative potentials pushed electrons within the channel to the edges, leaving a depleted region in the centre. Current through the gate-channel circuit was kept below 1 μA to avoid sample damage; a source-measure unit (SMU) was used to apply stable biases, the maximum bias not exceeding the current limit was 0.876 V. Application of a given bias to the sample was found to maintain practically the same concentration for all temperatures up to 100 K, so the carrier concentration calculated from the low temperature Stokes shift was used to obtain the chemical potential as a function of temperature.

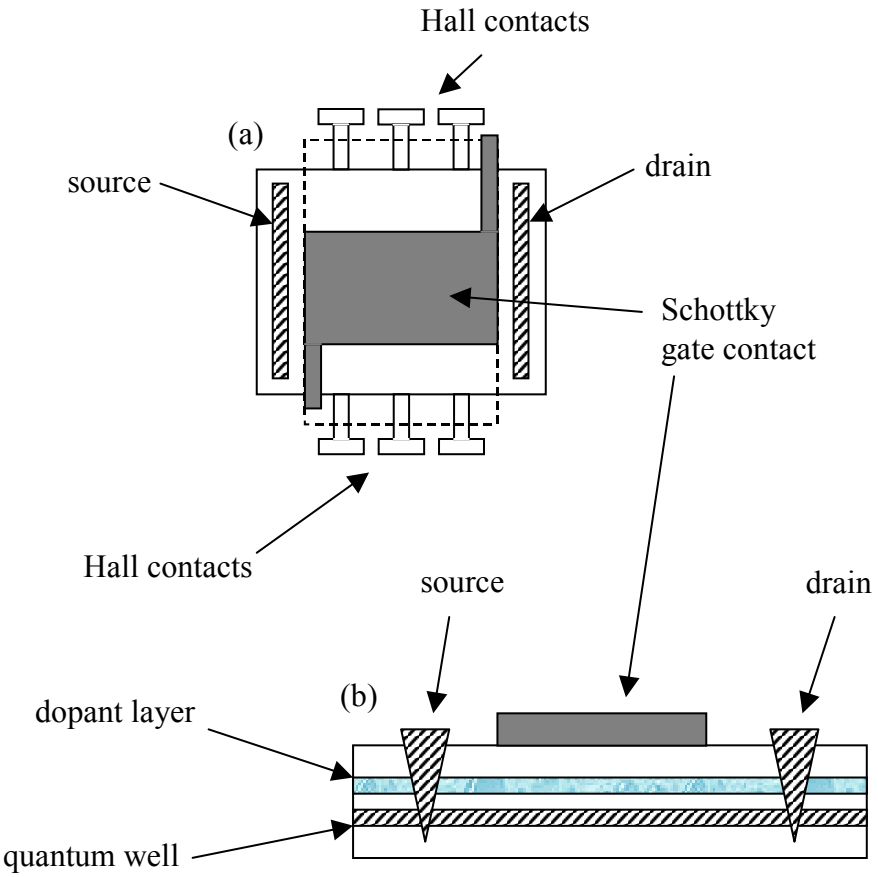

Figure 4.6: Top down (a) and edge on (b) schematics of sample T315. The source and drain make electrical contact with the quantum well layer and through application of a bias between them and the gate the electron concentration in the well can be manipulated. The Hall contacts to the well allow measurement of the mobility of the electron gas.

4.4.1 Sample mobility

Hall measurements of the mobility (μ) were made from 1.8 to 100 K using the arrangement illustrated in figure 4.7. The electron concentration in the channel was set by applying a potential to the gate. A small oscillating voltage of 0.1 V amplitude and frequency 17 Hz, sourced from the reference output of a digital lock-in, was applied across the source and drain. This drove electrons backwards and forwards in the channel. A magnetic field (B_z) of strength 300 mT was applied along the sample normal to add a Lorentz force which pushes electrons alternately towards the H_1 or H_2 side of the sample depending on the polarity of the cycle. The forcing voltage (V_X) was measured across terminals X_2 and X_1 and the resulting Hall voltage (V_H) across H_1 and H_2 using lock-in detection. Given the shape of our sample, the measured mobility is related to the Hall and forcing voltages by:

$$\mu = V_H/(B_z V_X), \tag{4.7}$$

and is shown in figure 4.8; empirically, it varied linearly with temperature over the range studied:

$$\mu = 26.376 - 0.175T \text{ m}^2\text{V}^{-1}\text{s}^{-1}, \tag{4.8}$$

and the scattering time (τ_p) implied by the mobility, shown in figure 4.8 is given by:

$$\tau_p = m_e \mu / e, \tag{4.9}$$

$$\text{i.e. } \tau_p = 10.05 - 0.067.T \text{ ps}. \tag{4.10}$$

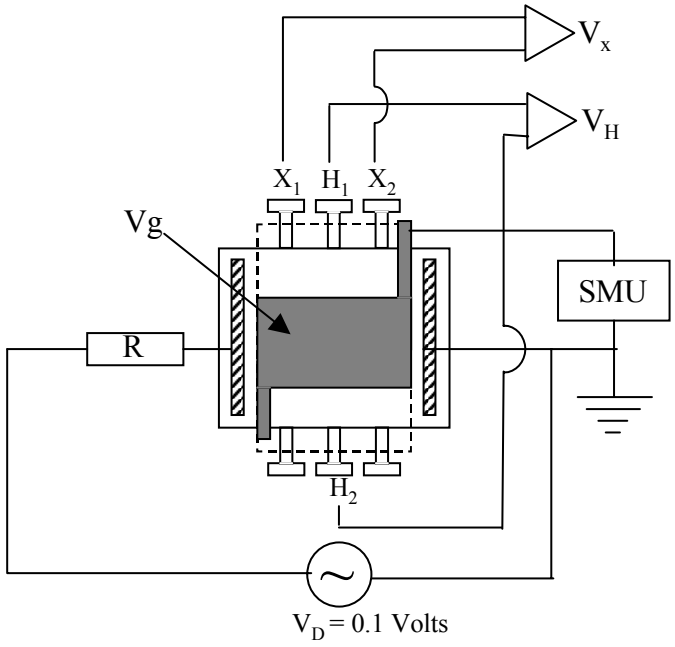

Figure 4.7: Diagram to illustrate how the mobility measurements were made. The potential between the gate and the channel was set to bias the maximum achievable electron concentration (1.86×10^{11} cm^{-2}) into the well using a source measure unit (SMU). A small oscillating voltage was added across the source and drain using the reference output from a digital lock-in and, a magnetic field of 300 mT was applied along the well normal. Measurement of the voltage drop across the contacts X_1 and X_2 (V_X), and across H_1 and H_2 (V_H) indicate the mobility of the electron gas in the well.

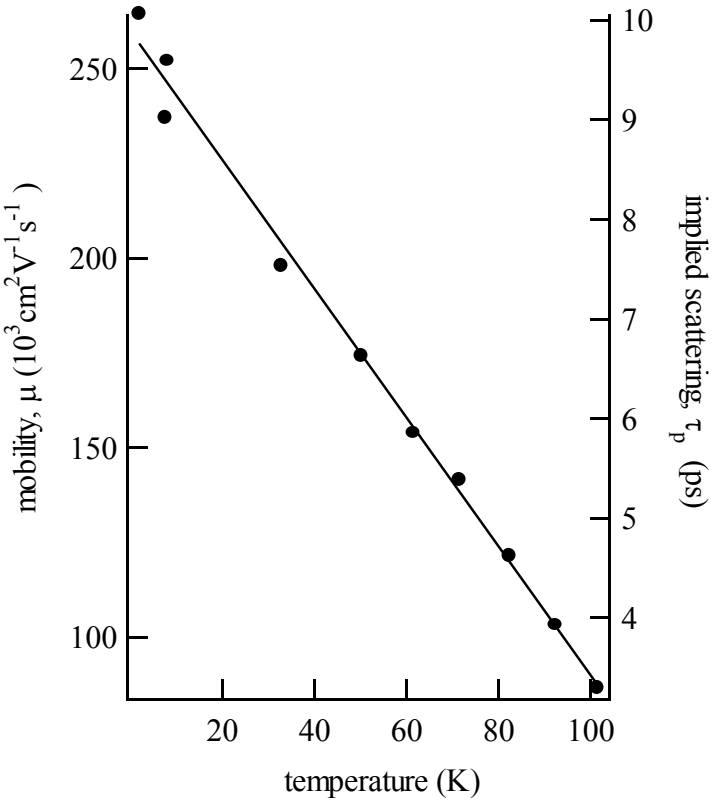

Figure 4.8: Plot of the measured mobility (circles) of the electron gas in sample T315 with a linear fit (line). The axis on the right indicates the momentum scattering time implied by the mobility.

4.4.2 Optical characterisation

Figure 4.9 contains the low temperature photoluminescence and photoluminescence excitation spectra with a bias of 0.8 V applied to the gate to force the maximum possible electron concentration in the channel. The peak of the photoluminescence excitation occurs at 1.5749 eV and that of the photoluminescence at 1.5643 eV, indicating a Stokes shift of 10.6 meV. Electroreflectance carried out in-situ with the time-resolved experiment allowed precise location of the Fermi energy without altering the sample alignment. This was achieved by adding to the bias a small oscillatory component (~ 0.1 V) and measuring reflectivity changes of the probe beam (with pump beam blocked) at the imposed frequency using lock-in detection

of the output of a GaAs photodiode as a function of the laser light wavelength. Peaks occur at wavelengths where the absorption changes rapidly.

Figure 4.9 contains typical results (dotted) of electroreflectance measurements; the peak coincides with the Fermi energy [23]. Electroreflectance measurements were used at 1.8 K to locate the Fermi energy precisely; at higher temperatures pump induced probe rotation and reflectivity changes at short delay (< 5 ps) as a function of wavelength were used to locate the wave-length of greatest probe rotation for the time-resolved experiments, which also coincides with the Fermi energy.

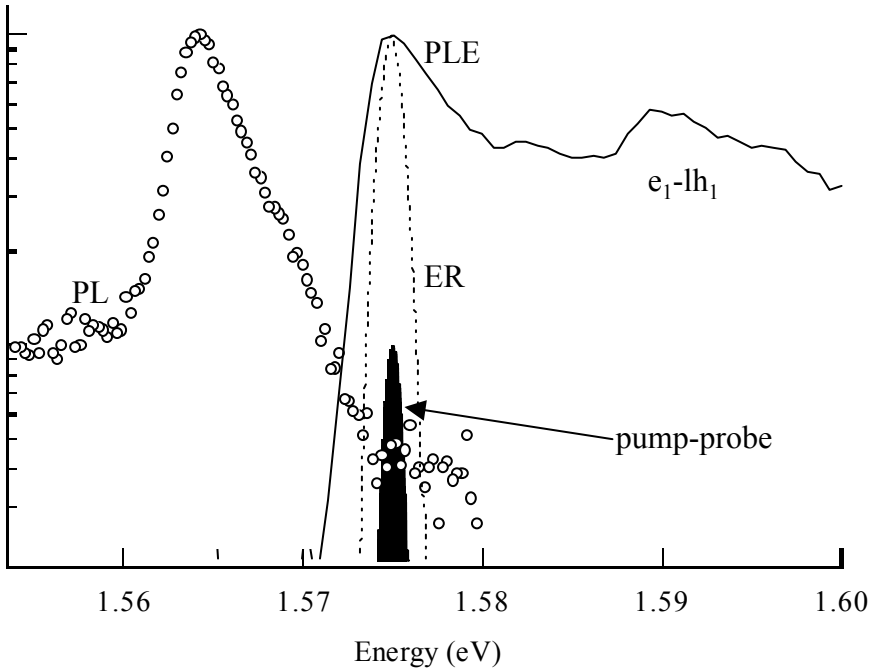

Figure 4.9: The photoluminescence (open circles), photoluminescence excitation (solid line), and electroreflectance (dashed) spectra with applied bias of 0.8 V between the gate and channel at 1.8 K show a Stokes shift of 10.6 meV indicating an electron Fermi energy of 6.64 meV in the conduction band and an corresponding electron concentration of 1.86×10^{11} cm^{-2}. Absorption into the light-hole valence band is observed just above 1.59 eV.

Assuming parabolic conduction band dispersion, the Fermi energy and Stokes shift are related by:

$$E_f = E_{stokes}/(1 + m_e/m_h), \quad (4.11)$$

where m_h and m_e are the hole and electron effective masses with values 0.067 and 0.112 [24] of the electron rest mass, giving a Fermi energy of 6.64 meV.

4.5 Experimental procedure

The sample was held in the Helium flow cryostat. The temperature was measured and controlled by an automatic electronic temperature controller, which was connected to an electronic heater and temperature sensor attached close to the sample holder. The controller was also able to regulate the flow of Helium gas, but greater stability was attained with constant gas flow. For measurements at 1.8 K the sample space was filled with liquid Helium and the temperature reduced by continuous pumping to maintain low pressure. For measurements above 4.2 K the sample was surrounded by flowing Helium gas and the temperature was controlled by balancing the electrical heater power against the gas flow rate. The laser was tuned to the Fermi energy as described above and the pump (probe) was focused to a ~60 (~30) μm diameter spot with beam intensities set to ~0.1 mW and 0.01 mW for the pump and probe respectively. The excitation density created by the pump was 2.10^9 cm^{-2}, ~2 % of the density of the 2DEG.

4.6 Results

The spin evolution at 1.8 K is shown in figure 4.10 along with results from Monte-Carlo type simulations of the D'Yakonov-Perel mechanism (described below).

Figures 4.11a-g contain the spin evolution measured at temperatures of 5, 10, 20, 30, 50, 70, and 100 K respectively. Spin evolution at temperatures of 5 K and above were fitted by the

product of a single exponential decay and a complimentary error function to approximate signal build-up:

$$A_1.\{1\text{-}0.5\text{erfc}[(t\text{-}t_0)/\Delta]\}.\exp[(t\text{-}t_0)/\tau_s] + A_2, \qquad (4.12)$$

Δ and t_0 were parameters to allow for the finite pulse width and errors in the estimate of the zero delay position, they were free parameters in the fit but did not vary significantly. Ideally results from cross-correlation of the pump and probe ought to be used in their place but such measurements were not made; values found by the fitting procedure were of acceptable magnitude. Background offsets in the recorded signals have been noted throughout the development of this time resolved experimental arrangement, explanation of its presence remains elusive. Parameter A_2 was used to eliminate this offset where present. The magnitude of response is a function of temperature, for example through weakening of the oscillator strength, and parameter A_1 allowed for this. The most significant parameter was τ_s which varied through more than an order of magnitude with temperature.

The experimental data presented in figures 4.11a-g have had their fitted values of parameter A_2 subtracted, been horizontally shifted by t_0 and divided by parameter A_1. Figure 4.13 collates results from selected temperatures and is intended to illustrate the magnitude of the effect of temperature.

Corresponding ΔR collected in-situ are shown in figure 4.12 for cases where such data was successfully recorded, evolution did not change with delay over the range of the spin signal measurement, indicating that the density of spin carriers remained constant throughout the measurement at all temperatures.

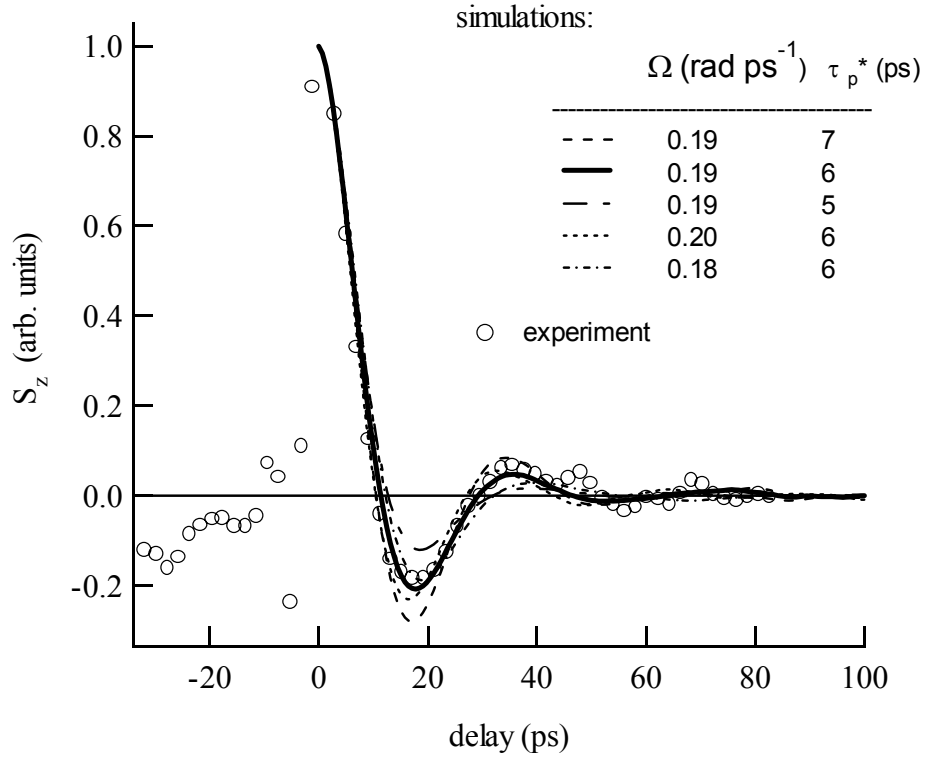

Figure 4.10: Spin evolution at 1.8 K (circles) and Monte-Carlo simulation (described below) results (curves). Monte-Carlo simulation for five sets of parameter values are shown.

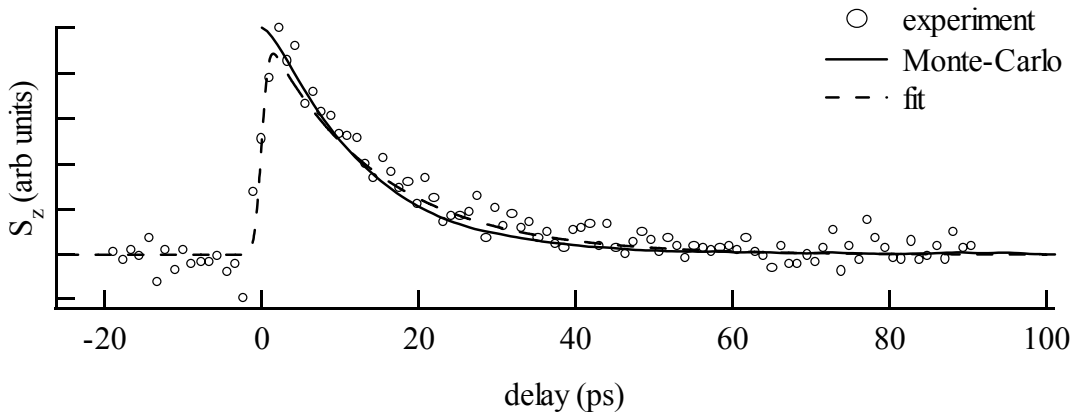

Figure 4.11a: Spin evolution at 5 K (circles) with fit (dashed curve) of decay rate τ_s^{-1} and, results of the Monte-Carlo simulation with a value of 0.19 rad ps^{-1} for $|\Omega|$ and $\tau_s^{-1}/|\Omega|^2$ for the scattering time τ_p*.

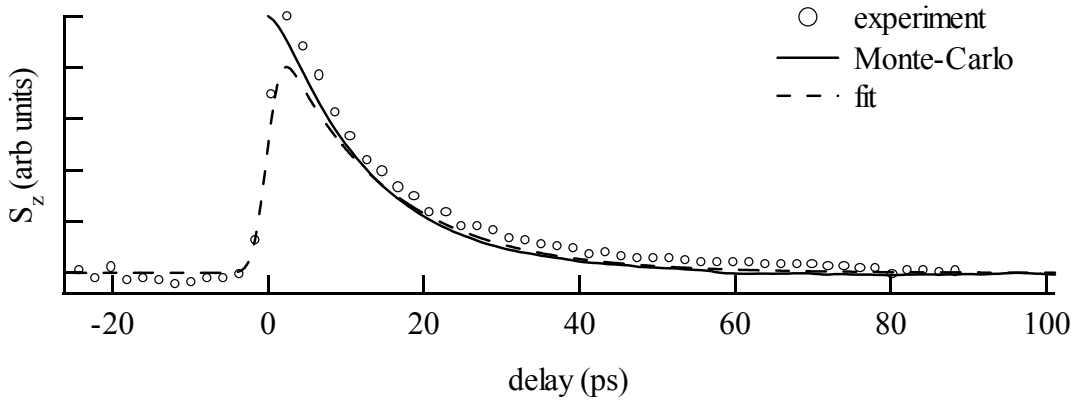

Figure 4.11b: Spin evolution at 10 K, see caption to figure 4.11a for description.

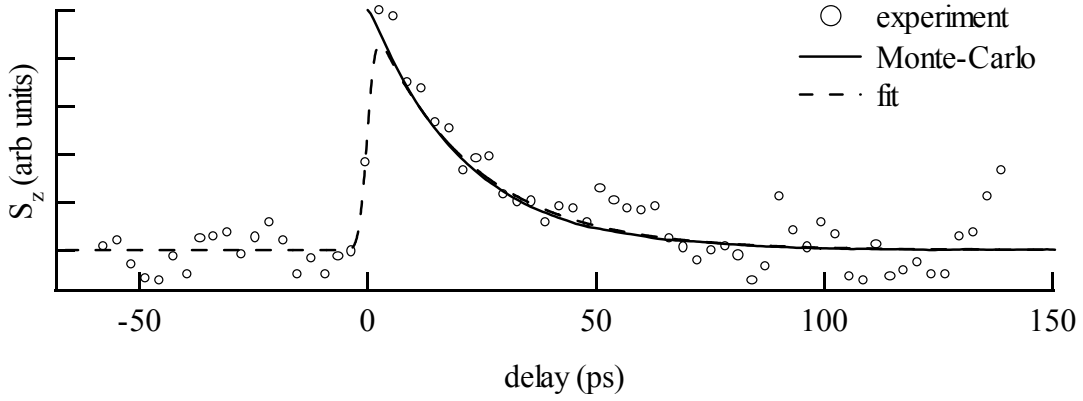

Figure 4.11c: Spin evolution at 20 K, see caption to figure 4.11a for description.

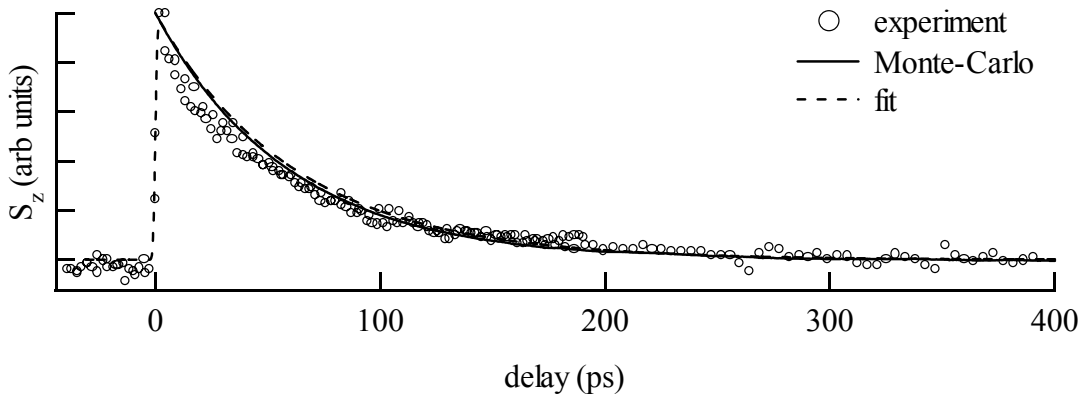

Figure 4.11d: Spin evolution at 30 K, see caption to figure 4.11a for description.

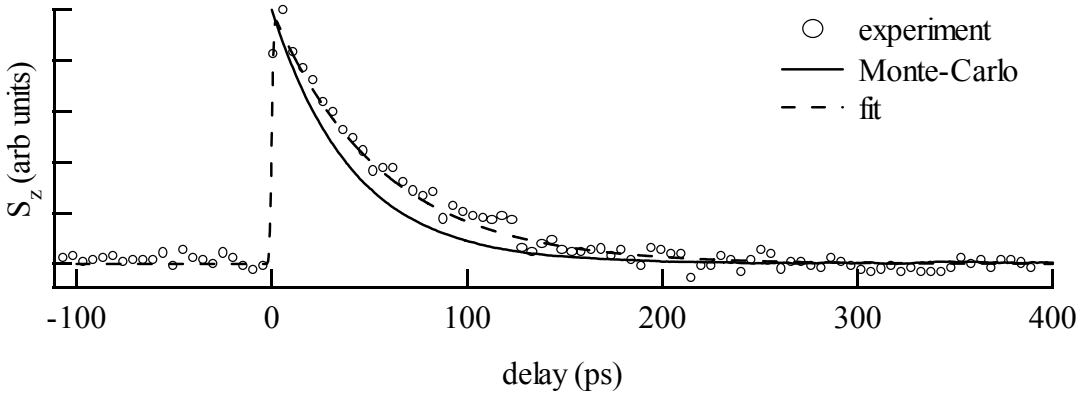

Figure 4.11e: Spin evolution at 50 K, see caption to figure 4.11a for description.

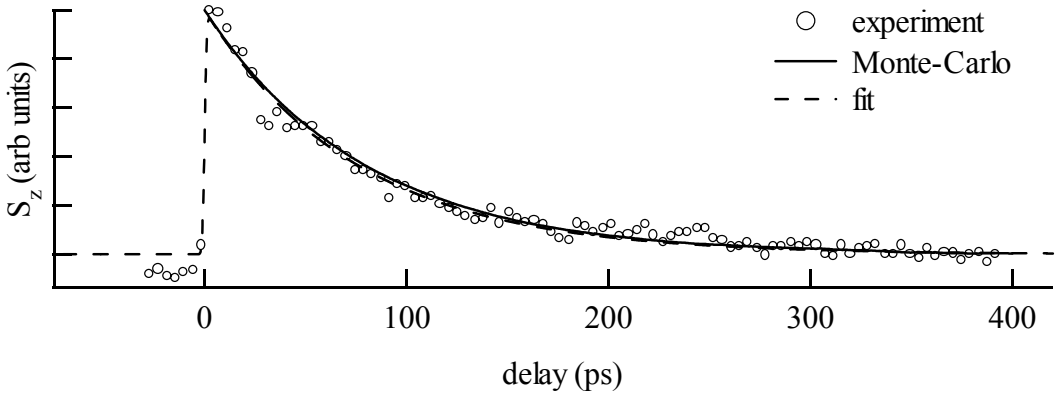

Figure 4.11f: Spin evolution at 70 K, see caption to figure 4.11a for description.

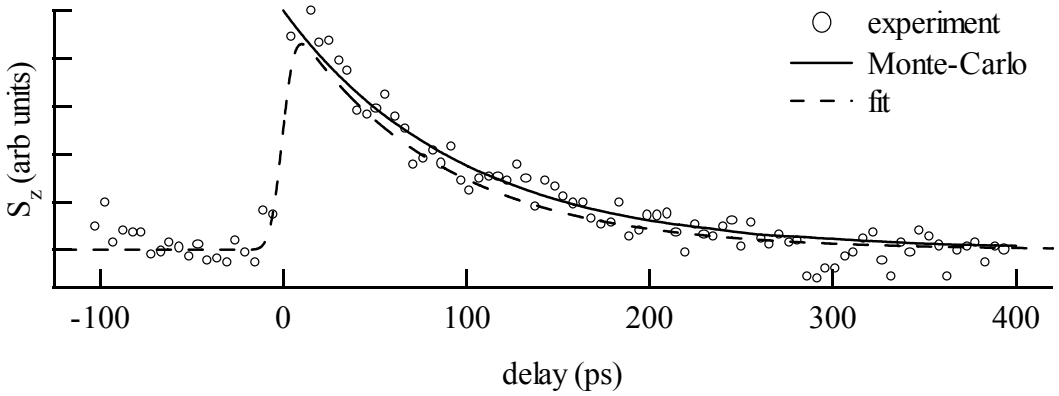

Figure 4.11g: Spin evolution at 100 K, see caption to figure 4.11a for description.

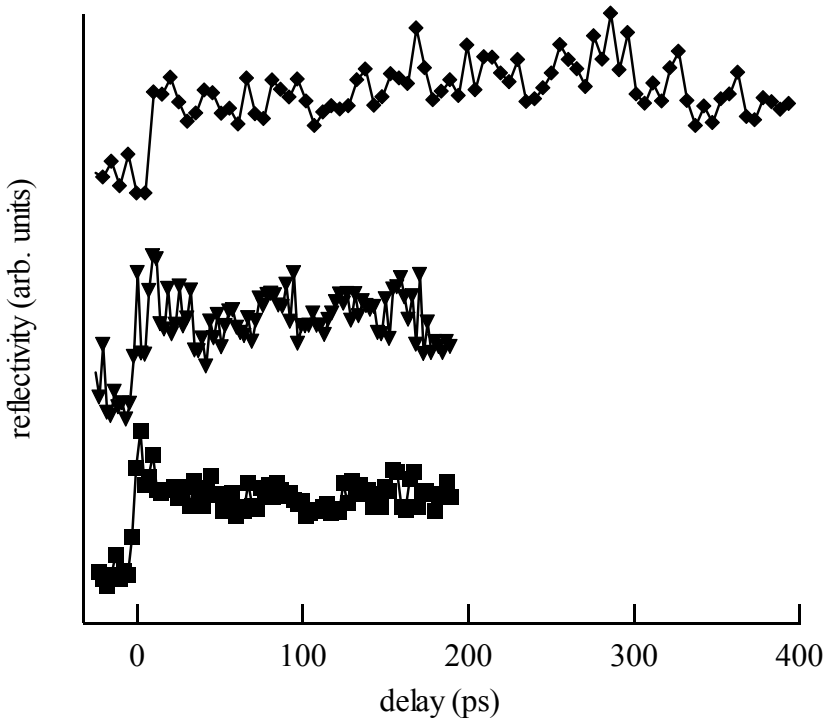

Figure 4.12: The change in reflectivity (squares 10 K, triangles 30 K, and diamonds 100 K) of the probe due to pump absorption (ΔR).

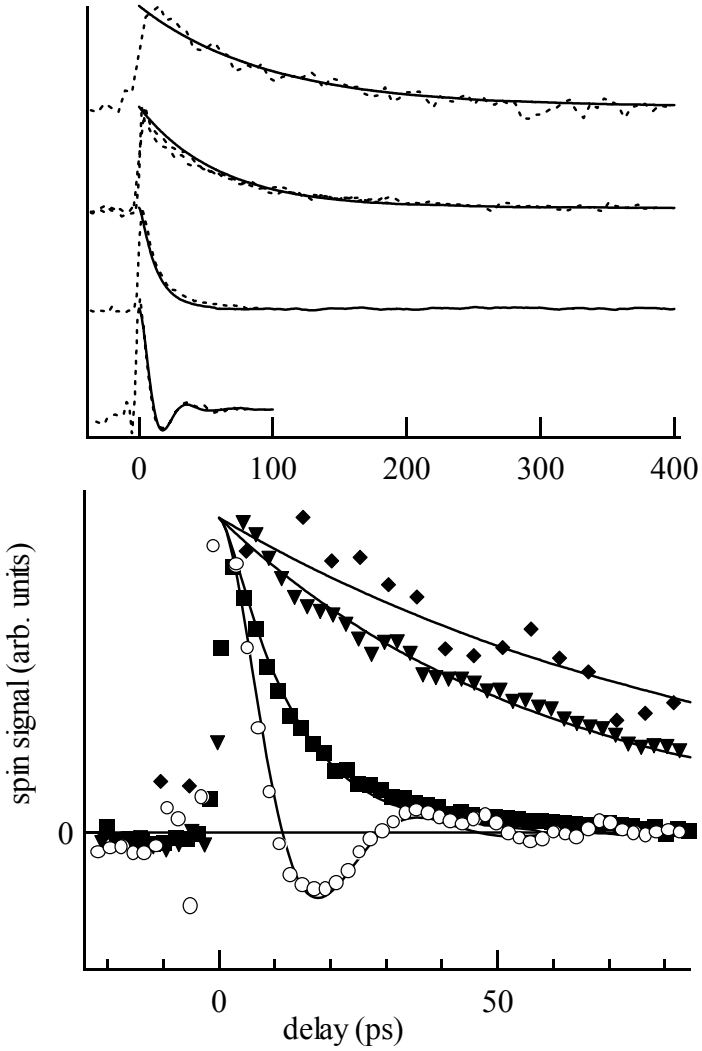

Figure 4.13: Top: Spin evolution at selected temperatures (1.8, 10, 30 and 100 K in ascending order) with the results of Monte Carlo simulations overlaid. The motional slowing of spin evolution as the scattering (temperature) increased is evident. Bottom: As top but with: open circles 1.8 K, squares 10 K, triangles 30 K and diamonds 100 K and focused on first 90 ps.

4.7 Analysis

In this section the results of the mobility and time-resolved measurements are brought together to show that there are two types of scattering that must be distinguished in spin

measurements; scattering which affects the mobility (mobility scattering, τ_p) and, scattering that affects the D'Yakonov-Perel type spin dynamics (spin scattering, τ_p^*).

4.7.1 Monte-Carlo simulation

Spin evolution under the D'Yakonov-Perel mechanism was simulated using a Monte-Carlo algorithm with 100,000 particles. Each particle, labelled by subscript i, was assigned the same precession frequency, $|\underline{\Omega}|$ (where $\underline{\Omega}$ represents the effective magnetic field vector around which the electron spin precesses); a random wave-vector in the x-y plane, $\underline{k}_i$; and an initial spin vector, $\underline{S}_i$, of unit length and initially along the z-direction, with zero spin component in the x and y directions. After increments of time, dt, suitably short to satisfy the Nyquist criterion, the direction of each electron wave-vector was scattered in the plane at random with probability dt/τ_p^*, and then the spin vector of each electron was updated according to the formula:

$$\underline{S}_i(t+dt) = \underline{S}_i(t) + (\underline{\Omega}(\underline{k}_i) \times \underline{S}_i(t))dt, \qquad (4.13)$$

which rotates the spin vector, simulating precession. Time was then incremented to t+dt. The process was repeated until a specified simulation time was reached.

Running the model with systematic variation of choice for the values of parameters $|\underline{\Omega}|$ and τ_p^* reveal that spin evolution at 1.8 K was best modelled with values 0.19±0.02 rad ps^{-1} and 6 ±1 ps respectively (figure 4.10).

For temperatures of 5 K and above, the spin relaxation rates obtained from the exponential fit (equation 4.12) were divided by the value of $|\underline{\Omega}|^2$ obtained from the 1.8 K data to yield the scattering, τ_p^*, that was effective (see equation 4.2) in motional slowing of spin precession for each temperature. The Monte-Carlo simulation was then repeated seven times with the value of $|\Omega|$ fixed but with τ_p^* set to the calculated values for each temperature. It can be seen that

the simulation results agree well with the measured spin evolution (figures 4.11a-g) confirming the D'Yakonov-Perel mechanism as the cause of the spin relaxation.

Values thus determined for τ_p^* are shown in figure 4.14 along with the scattering that determines the mobility, τ_p. At very low temperatures two scattering times appear to converge. At high temperatures it is seen that the spin system is subject to greater scattering than that which inhibits the mobility of the electron gas.

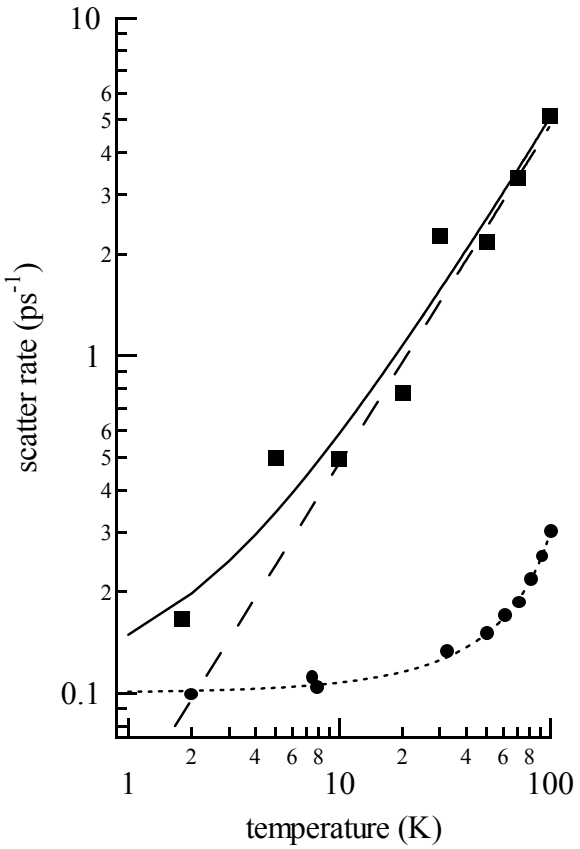

Figure 4.14: Momentum scattering rate from Hall mobility measurements, τ_p^{-1} (circles) with linear fit (dotted line) and the scattering rate effective in precessional slowing, τ_p^{*-1} (squares). The solid line is sum of τ_p^{-1} and the electron-electron scattering rate, $\tau_{e\text{-}e}^{-1}$ (dashed line) assumed to vary linearly with temperature.

4.7.2 Electron-electron scattering

With reference to figure 4.14, discussion of the results so far show that at temperatures much above ~2 K the electron wavevector is subject to a scattering process which is faster than that which affects the mobility. Its rate is small at low temperatures, increases linearly with temperature at high temperatures and, it does not affect the centre-of-mass momentum of the electron gas. A scattering process which possesses all of these properties is electron-electron scattering.

Due to the Pauli exclusion principle the electron-electron scattering rate for electrons at the Fermi energy ($\tau_{e\text{-}e}^{-1}$) approaches zero as the temperature reduces towards 0 K because of the sharpness of the Fermi edge [14, 15]. The elastic electron-electron scattering rate ought to be proportional to the integral of the product of the number of occupied and unoccupied conduction band states:

$$\tau_{e\text{-}e}^{-1} \sim \int (1-f) f \, dE \propto T, \tag{4.14}$$

where f is the Fermi-Dirac distribution of the electrons (the linear dependence of the integral on T was determined by numerical integration). The total scattering that is effective in randomising the spin-splitting experienced by the electron is given by the sum of the e-e and the momentum scattering:

$$\tau_p^{*-1} = \tau_p^{-1} + \tau_{e\text{-}e}^{-1}, \tag{4.15}$$

and is plotted as a solid curve in figure 4.14.

Glazov and Ivchenko [6] present our data along with a more detailed theory of D'yakonov-Perel-Kachorovskii type spin relaxation which includes the electron-electron scattering. They obtained good theoretical estimates of both the mobility scattering and spin scattering and find that the electron-electron scattering vanishes with temperature as $\sim T^2.\ln T$ and varies as ~T at high temperatures.

4.7.3 Spectral sampling of the conduction band spin-splitting and anisotropy

The conduction band spin-splitting increases with the electron energy but is also a function of the wave-vector direction (equation 4.1). Thus, although the spectral distribution of the resonantly excited electrons is sharply grouped around the Fermi energy at low temperature, a range of conduction band spin-splitting strengths may still be sampled. This will lead to coherent dephasing of the precessing spin population in the absence of any wave-vector scattering. In this section the rate of decay of the spin signal due to these processes is estimated.

Wavevector dependence of the effective field (equation 4.1) acting on the spin of an electron is easier to visualise in polar co-ordinates, obtained by substituting the separate components of the wave-vector:

$$\begin{aligned} k_x &= k.\cos(\theta), \\ k_y &= k.\sin(\theta), \end{aligned} \tag{4.16}$$

where k is the magnitude and θ is the angle in the plane of the well of the electron wave-vector, the effective field then expresses as:

$$\begin{aligned} \Omega_x &= Ak.\cos(\theta) - Bk^3\cos(\theta)\sin^2(\theta) - Ck.\sin(\theta), \\ \Omega_y &= -Ak.\sin(\theta) + Bk^3\cos^2(\theta)\sin(\theta) + Ck.\cos(\theta), \\ A &= 2a_{42}\langle k_z^2\rangle/\hbar, \\ B &= 2a_{42}/\hbar, \\ C &= 2a_{46}/\hbar. \end{aligned} \tag{4.17}$$

The expectation value $\langle k_z^2\rangle$ can be found from photoluminescence measurements. The quantum confinement energy is given by:

$$\hbar^2\langle k_z^2\rangle/(2m^*) = E_c^e = (E_{PL} - E_{BG})/(1 + m_e/m_h), \tag{4.18}$$

where E_{PL} is the peak of the photoluminescent emission and E_{BG} is the low temperature bulk GaAs band-gap with a value of 1.5190 eV [25]. Using values of 0.067 and 0.112 [24] for the

effective electron and hole masses, the measured confinement energy is 28.3 meV which indicates a value of 4.92×10^{16} rad^{2}m^{-2} for $\langle k_z^2 \rangle$. The values of parameters A and B are 2.39×10^3 ms^{-1} and 4.9×10^{-14} m^{-3} s^{-1} respectively; and parameter C can be written as $17.E_z$ in units of ms^{-1}, where E_z is the electric field in the growth direction in kV cm^{-1}.

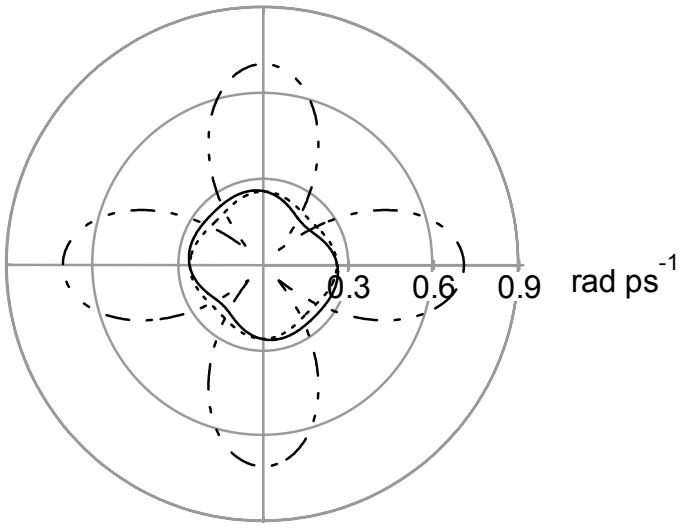

Figure 4.15: Polar plot of the calculated conduction band spin-splitting for electrons at the Fermi energy (6.64 meV) with an electric field of 0 (dashed) and 15 (solid) kVcm^{-1}. At 50 meV (dash dot) with electric field of 0 kVcm^{-1} the anisotropy becomes much more pronounced. The angle-averaged values are 0.238 and 0.241 rad ps^{-1} for 0 and 15 kV cm^{-1} respectively for electrons at the Fermi energy.

Examination of the angular variation of the calculated effective field strength, shown in figure 4.15, illustrates that anisotropy was strong at high temperatures, where the tail of the Fermi distribution extends to high energies. Assuming an isotropic distribution for the electron in-plane wavevector of the photoexcited population leads to an angle averaged squared spin splitting:

$$\langle\Omega^2\rangle_\theta = k^2(8A^2 - 4ABk^2 + B^2k^4 + 8C^2)/8, \quad (4.19)$$

which can be used to obtain the average squared frequency as a function of the electron energy only; this is plotted in figure 4.17 as for two values of electric field. The average $\langle|\Omega|\rangle$ has the value 0.241 rad ps^{-1} at the Fermi energy assuming the estimated built-in electric field of ~15 $kVcm^{-1}$ [26], which is close to the measured value of 0.19±0.02 rad ps^{-1}.

A simple method of averaging the spin splitting over the photoexcited electron spin population can be obtained by assuming full thermalisation within the pulse duration. This is most likely not achieved at low temperatures [14, 15] because $\tau_{e\text{-}e}^{-1}$ is small for non-equilibrium carriers injected at the Fermi energy. Within a thermalised electron distribution each spin state can be represented as a separate Fermi population, and the spin polarisation as the difference of state occupation for each spin state:

$$g(E) = 1/\{1 + \exp[(E-\mu^{+/-})/k_BT]\} - 1/\{1 + \exp[(E-\mu^{+/-})/k_BT]\}, \quad (4.20)$$

$\mu^{+/-}$ is the chemical potential, given by equation 4.5, for each spin state. Fermi energies of the spin-up and spin-down populations under the conditions of the experiment are calculated (as described in section 4.3.3) as 6.75 and 6.64 meV respectively, the corresponding chemical potentials are plotted in figure 4.16, and the distribution g(E) in figure 4.17.

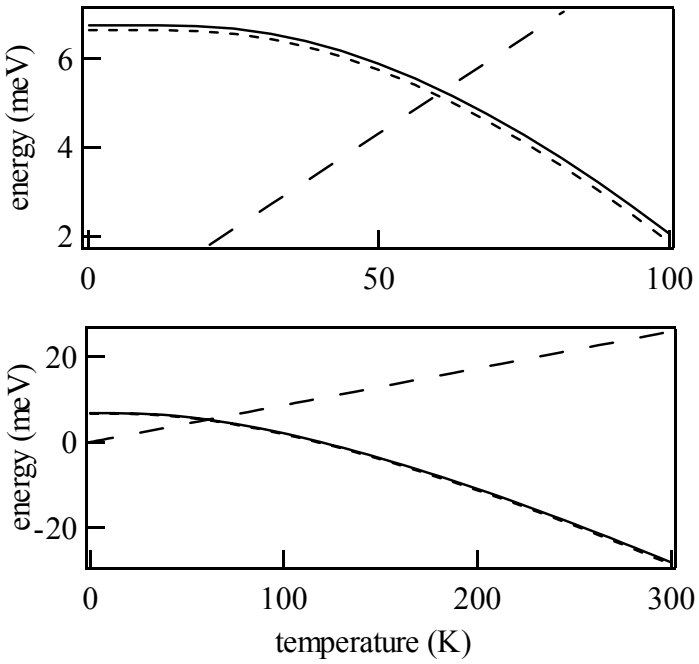

Figure 4.16: Temperature dependence of the chemical potential for the spin-up (solid curve) and spin-down (short dash) electron populations. Also shown is the value of k_BT (long dash). The electron gas can be approximated as non-degenerate if the chemical potential is of the order of k_BT below the bottom of the conduction band (defined as zero meV on this scale) which holds above 200 K.

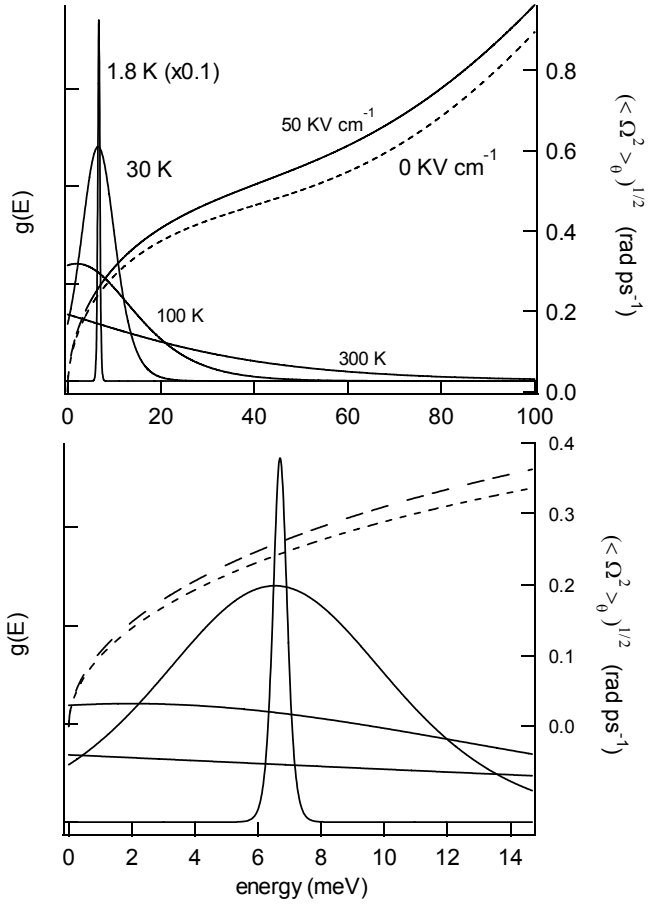

Figure 4.17: Spectral distribution of the spin polarisation (plotted as solid curves against the left axis and defined as the difference between spin state populations, e.g. figure 4.5) for temperatures of 1.8, 30, 100 and 300 K. In conjunction with the calculated conduction band spin-splitting (against right axis) for electric field values of 0 (short dash) and 50 (long dash) $kVcm^{-1}$ as a function of the electron energy this illustrates that at high temperatures a distribution of spin-splittings is sampled – leading to natural dephasing of the precessing spin population even in the absence of wave-vector scattering.

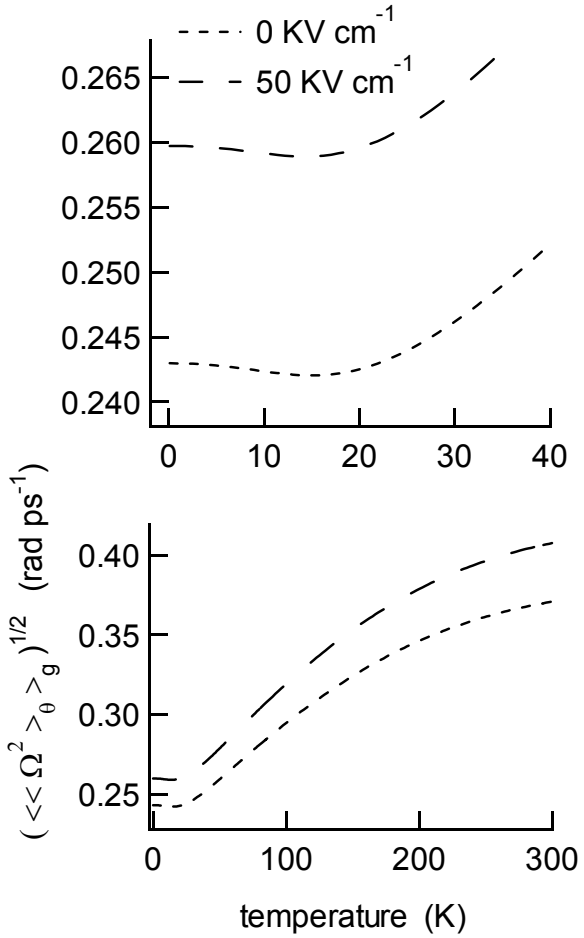

Figure 4.18: Temperature dependence of the square root of the average square spin-splitting (equation 4.21), evaluated for electrons at the Fermi energy in sample T315 for electric fields of 0 (short dash) and 50 (long dash) KV cm^{-1}. The frequency decreases slightly up to ~15 K then increases by ~20 % up to 100 K.

In the absence of excitation the spin states are equally populated (due to the doping) and have equal chemical potentials. That of the pumped state is considered to increase (figure 4.5) upon absorption of the circularly polarised pump. Within this picture, the spin polarisation is narrowly bunched around the Fermi energy at low temperatures and the spin splitting is approximately constant over the strongly polarised energy region. With increasing temperature

the distribution spreads in energy and the sampled spin splitting becomes significantly inhomogeneous, account of this can be taken by averaging over the spin population:

$$<\underline{\Omega}^2> = \{\int_0^\infty <\underline{\Omega}^2>_\theta \cdot g(E)dE)\} / \{\int_0^\infty g(E)dE\}, \tag{4.21}$$

plotted in figure 4.18. For the present case, the integral in the denominator has the constant value 0.11 meV for temperatures below 130 K.

Precession of the spin vectors of the energy distributed electrons occurs at different rates because the precession rate is a function of the electron energy. The net effect of such differential precession is to reduce the magnitude of spin polarisation in each direction as time progresses. Decrease of the spin signal due to this process is termed natural dephasing to distinguish it from spin processes which are non-reversible such as those involving momentum and electron-electron scattering.

Two contributions of natural spin dephasing are present, one due to the energy distribution of spin polarisation, and the other due to the anisotropy of the spin splitting. The former vanishes with vanishing temperature because the electrons become tightly bunched in a narrow energy range around the Fermi energy. The remaining anisotropy driven dephasing ought to cause loss of spin signal even at vanishing temperatures. To estimate its effectiveness the sum of many harmonic terms at frequencies $\Omega(\theta)$ was evaluated:

$$S(t) \sim \sum_{\theta=0}^{2\pi} \cos(\Omega(\theta).t), \tag{4.22}$$

plotted in figure 4.19 for two value of the electric field E_z. It is the theoretical temporal evolution of the spin signal in the absence of scattering for electrons at the Fermi energy subject to the spin-splitting anisotropy. The calculated natural dephasing time (i.e. the half-life of the signal intensity) is clearly much longer than the decay observed experimentally (figures 4.10 and 4.14), indicating that it is not the limiting factor on the spin lifetime and that

scattering processes are indeed the most important. The figure also indicates the type of signal to expect from ultra pure samples at ultra low temperatures where both momentum and electron-electron scattering are weak.

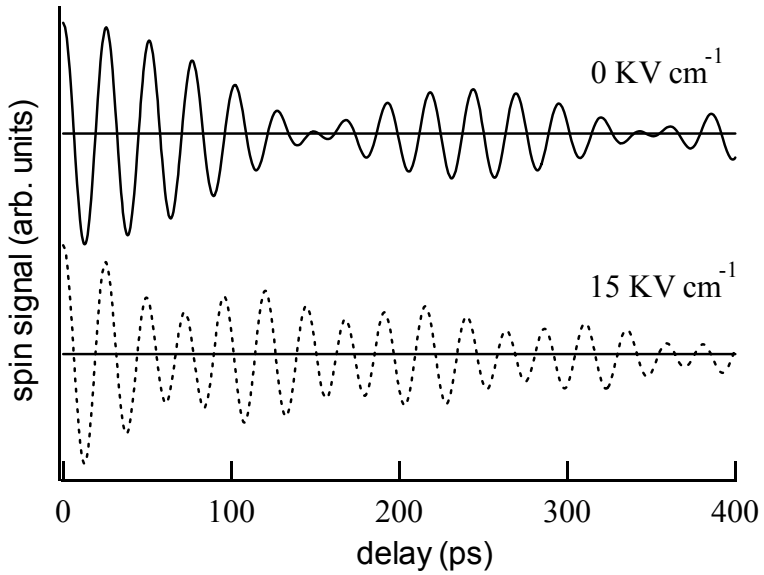

Figure 4.19: The calculated spin signals in the absence of scattering for an electric field across the 2DEG of 0 (solid curve) and 15 $kVcm^{-1}$ (dashed curve) indicate that the natural dephasing due to the anisotropy of the conduction band spin-splitting was too weak to produce the fast decay observed experimentally (figure 4.10), which occurred fully within ~100 ps.

4.8 Summary and conclusions

Spin evolution in a high mobility 2DEG has been investigated experimentally. On the basis of existing theoretical descriptions we expected to observe quasi-free precession at temperatures up to 100 K due to the high mobility of the sample. In fact we only observed precession, which was heavily damped, at the lowest temperature, 1.8 K; otherwise the spin polarisation decayed exponentially. We were able to calculate the rate of scattering suffered by the electrons, which caused the observed spin evolution, and found this was faster than that

indicated by the mobility. The results suggest that it was the electron-electron scattering that resulted in the slow spin decays.

4.9 References

1. **"Spin relaxation of conduction electrons in noncentrosymmetric semiconductors"**, M. I. D'yakonov and V.I. Perel, *Sov. Phys. Sol. Stat.* ***13*** *3023 (1972)*;

"Spin orientation of electrons associated with the interband absorption of light in semiconductors", M. I. D'yakonov and V. I. Perel, *Sov. Phys. JETP 33 1053 (1971).*

2.**"Spin relaxation of two-dimensional electrons in noncentrosymmetric semiconductors"**, M. I. D'yakonov and V. Yu. Kachorovskii, *Sov. Phys. Semicond.* ***20*** *110 (1986).*

3. **"Optical Orientation, Modern Problems in Condensed Matter Science"**, edited by F. Meier and B. P. Zakharchenya, North-Holland, Amsterdam, (1984).

4. **"Precession and Motional Slowing of Spin Evolution in a High Mobility Two-Dimensional Electron Gas",** M. A. Brand, A. Malinowski, O. Z. Karimov, P. A. Marsden, R. T. Harley, A. J. Shields, D. Sanvitto, D. A. Ritchie, and M. Y. Simmons. *Physical Review Letters,* ***89*** *239901 (2002).*

5. **"Precession spin relaxation mechanism caused by frequent electron-electron collisions"**, M. M. Glazov and E. L. Ivchenko, *JETP Letters* ***75*** *403 (2002).*

6. **"D'yakonov-Perel' spin relaxation under electron-electron collisions in n-type QWs",** M. M. Glazov, E. L. Ivchenko, M. A. Brand, O. Z. Karimov and R. T. Harley. *To be published (2002).*

7. **"Electron-spin decoherence in bulk and quantum-well zinc-blend semiconductors"**, W. H. Lau, J. T. Olesberg and M. E. Flatté, *Phys. Rev. B* ***64*** *161301® (2001).*

8. **"Room-temperature spin memory in two-dimensional electron gases"**, J. M. Kikkawa, I. P. Smorchkova, N. Samarth and D. D. Awschalom, *Science* ***227*** *1284 (1997).*

9. **"Spin relaxation of electrons due to scattering by holes"**, G. L. Bir, A. G. Aronov, and G. E. Pikus, Sov. Jetp. **42** 705 (1976).

10. "Theory of the effect of spin-orbit coupling on magnetic resonance in some semiconductors", R. J. Elliot, Phys. Rev. 96 266 (1954).

11 .**"g-factors and spin-lattice relaxation of conduction electrons"**, Y. Yafet, Solid State Phys. **14** 1 (1963).

12. "Investigation of narrow-band semiconductor quantum well structures using a synchronously-pumped optical parametric oscillator", P. A. Marsden, *Ph.D. thesis, University Of Southampton (2001).*

13. **"Spin-orbit coupling effects in Zinc Blende structures"**, G. Dresselhaus, Phys. Rev. **100** 580 (1955).

14. "Ultrafast spectroscopy of semiconductors and nanostructures", J. Shah, *Springer, (1998).*

15. **"Carrier-carrier scattering in a degenerate electron system: Strong inhibition of scattering near the Fermi edge"**, D. S. Kim, J. Shah, J. E. Cunningham, T. C. Damen, S. Schmitt-Rink, W. Schäfer, *Phys. Rev. Lett.* ***68*** *2838 (1992).*

16. **"Exciton vs free-carrier spin-relaxation in III-V quantum wells"**, A. Malinowski, P. A. Marsden, R. S. Britton, K. Puech, A. C. Tropper and R. T. Harley, *Proc. 25th Int. Conf. Phys. Semicond., Osaka, Part* ***1*** *631 (2001).*

17. **"Electron-states in GaAs/$Al_{1-x}Ga_xAs$ heterostructures – Non parabolicity and spin-splitting"**, F. Malcher, G. Lommer and U. Rossler, Superlattices Microstruct. **2** (**3**): 267-272 (1986).

18. See for example: **"Spin orientation at semiconductor heterointerfaces"**, B. Jusserand, D. Richards, G. Allan, C. Priester and B. Etienne, *Phys. Rev. B* ***51*** *4707 (1995)*.

19. ***"Spin Dynamics in Semiconductors"*** **in** ***"Spintronics and Coherence"***, M. E. Flatté, J. M. Byers and W. H. Lau, edited by D. D. Awschalom and N. Samarth, *Springer (2002).*

20. **"Hole polarization and slow hole-spin relaxation in an n-doped quantum-well structure"**, Ph. Roussignol, P. Rolland, R. Ferreira, C. Delalande, G. Bastard, A. Vinattieri, J. Martinez-Pastor, L. Carraresi, M. Colocci, J. F. Palmier and B. Etienne, *Phys. Rev. B* ***46*** *7292 (1992).*

21. **"Hole spin relaxation in n-modulation doped quantum wells"**, B. Baylac, T. Amand, X. Marie, B. Dareys, M. Brousseau, G. Bacquet and V. Thierry-Mieg, *Solid State Com.* ***93*** *57 (1995).*

22. **"Spin relaxation in low-dimensional systems"**, L. Viňa, *J. Phys., Condens. Matter,* ***11*** *5929 (1999).*

23. "**Electron density dependence of the excitonic absorption thresholds of GaAs quantum well",** R. Kaur, A. J. Shields, J. L. Osborne, M. Y. Simmons, D. A. Ritchie and M.Pepper, Phys. Stat. Sol. **178** 465 (2000).

24. **"Laser Spectroscopy of Semiconductor quantum Wells"**, A. S. Plaut, *Ph.D. thesis, Oxford (1988).*

25. GaAs band-gap value taken from **"Survey of Semiconductor physics"**, K. W. Böer, *Van Nostrand Reinhold (1990).*

26. Private communication, A. Shields. Also calculated using *"1D Poisson/Schrödinger"* solver written by Greg Snider, Department of Electrical Engineering, University of Notre Dame, public domain software (2001).

5. Spin relaxation in undoped InGaAs/GaAs quantum wells

5.1 Introduction

In InGaAs/GaAs and InGaAs/InP nanostructures it is the tertiary InGaAs layer that forms the quantum well region. Malinowski et al. [1] (also see Marsden [2]) have reported measurements of resonant spin dynamics in GaAs/AlGaAs and InGaAs/InP quantum wells. At low temperatures, where exciton spin dynamics dominate, the spin relaxation rates in the two systems were similar, but with increasing temperature they observed in GaAs/AlGaAs the development of a long-lived tail in the spin signal, which they interpreted as the signature of an unbound electron population with a spin lifetime (~50 ps) as predicted by the D'Yakonov-Perel mechanism (see chapter 4). Such a long-lived component of spin was not observed in the InGaAs/InP system, indicating electron spin relaxation about one order of magnitude faster than in GaAs/AlGaAs.

A significant difference between the two systems is that in GaAs/AlGaAs the anions and cations in the quantum well layer are the same as in the barrier, whereas in InGaAs/InP the this is not true. This leads to an extra term in the conduction band spin splitting (the Native Interface Asymmetry, see section 4.3.1) and thus to increased spin relaxation. The work of this chapter investigates spin dynamics in an InGaAs/GaAs nanostructure, which has no native interface asymmetry, and was designed to determine if electrons in InGaAs wells have an intrinsically short spin lifetime or if the nature of the interface between the well and barrier causes the observed fast relaxation in InGaAs/InP. Measurements of spin evolution in two

undoped $In_{0.11}Ga_{0.89}As/GaAs$ quantum wells are described with pump/probe wavelength maintained resonant with the n=1 heavy-hole exciton at temperatures from 5 to 150 K.

The low Indium content (11%) of the wells results in a very weak confining potential and at high temperatures the carriers are no longer confined to the quantum wells, carrier emission processes becomes important. This necessarily adds some complications to the processes and measurement of spin relaxation, which are discussed in the text. Over a small range of temperatures, high enough for the exciton to ionise but low enough that carrier emission is negligible, we measure the electron spin relaxation rate which can be compared to the results of Malinowski et al. [1]. We find a long electron spin life-time of ~700 ps in the InGaAs/GaAs quantum well of similar width (100 Å) to theirs, suggesting that the conduction band spin-splitting due to the native interface asymmetry was the factor causing the fast decay observed in their InGaAs/InP nanostructure.

An interpretation of the temperature dependence over the full range investigated is offered which breaks the existence of the photoexcited population in the well into three epochs separated by the exciton-acoustic phonon scattering time; the exciton-LO phonon scattering time; and bounded by the scattering time of the resulting electron-hole plasma with LO-phonons, which results in their emission from the well. It is argued that at low temperatures the decay of the ΔR signal indicates the rate of exciton dephasing by acoustic phonon scattering and that in conjunction with the measured $\Delta\theta$ decay, these can be used in the exchange driven motional narrowing exciton spin relaxation mechanism of Maialle et. al. [3] to obtain the long-range exchange strength.

5.2 Background and theory

Optical properties in quantum wells are strongly modified by the presence of excitons, the resonant enhancement of the optical response at the band edge and the Sommerfeld

enhancement of the unbound states is well known. In doped samples the attraction between the electron and hole of an exciton is screened by the Coulomb field of the electrons (holes) added by the n- (p-) doping, it results in a weakening of the exciton binding energy. With moderate doping the formation of charged excitons is possible. With heavy doping, the phase space filling effect can block exciton formation; this can be schematically thought of in terms of the real space that is left devoid of electrons in comparison to the cross sectional area of the exciton. Spin dynamics also are modified when conditions favour the formation of excitons with the most obvious effects being the exchange enhancement of spin decay due to the close proximity of the electron and hole constituents and the inhibition of hole spin relaxation by the exchange splitting.

5.2.1 Exciton spin dynamics

Heavy-hole excitons can be created through resonant excitation, and by varying the polarisation of the exciting light their initial spin polarisation can be selected. The z-component of angular momentum of an exciton, J^{ex}_z, is equal to the sum of the components of its constituents, $S_z+J^h_z$, where S_z and J^h_z are the z-components of the electron and hole angular momentum respectively. Four spin configurations of the heavy-hole exciton are possible:

J^h_z	S_z	J^{ex}_z
+3/2	+1/2	+2
+3/2	-1/2	+1
-3/2	+1/2	-1
-3/2	-1/2	-2

(5.23)

Since the ground state of the system has $J^h_z = S_z = 0$, the $J^{ex}_z=\pm2$ states cannot couple to light in a single photon process (as a photon carries only ±1 unit of angular momentum). Consequently these states are commonly termed dark or optically inactive exciton states. On

the other hand, the $J^{ex}_z=\pm1$ states can couple to a photon and are termed bright or optically active exciton states. Degeneracy of the $J^{ex}_z=\pm1$ and $J^{ex}_z=\pm2$ exciton doublets is broken by the spin-exchange interaction[1], they are split by the exchange energy Δ [3]. The heavy-hole exciton spin energy structure is illustrated in figure 5.1.

A spin-polarised population of excitons in the $|+1>$ (i.e. $J^{ex}_z = +1$) state may be generated by resonant σ^+ excitation. The spin polarisation can diminish by independent single particle spin flip of the electron or hole constituent to form optically inactive excitons, or via a coupled electron-hole spin relaxation mechanism which arises from the close spatial proximity of the electron and hole mediated by the exchange interaction and generates oppositely polarised optically active excitons, $|+1>$.

Spin relaxation of unbound electrons (at rate τ_e^{-1}) in III-V systems is determined by the motional narrowing D'yakonov-Perel mechanism, and hole spin relaxation (at rate τ_h^{-1}) by the combination of valence band mixing and momentum scattering. In general it is usually assumed that $\tau_h << \tau_e$, but at low temperatures this may not hold. In bulk materials or wide quantum wells, the strong valence band mixing at $\underline{k}=0$ causes rapid hole spin relaxation. Lifting of the hh-lh degeneracy and displacement of the mixing to higher wave-vectors by quantum confinement increases τ_h considerably and for holes which remain at $\underline{k}=0$, the hole spin-lifetime is infinite [4]. However, at low temperatures in undoped systems the effects exciton binding, for example the coupled electron-hole spin-flip mechanism is usually more important than these single particle processes.

Because the electron and hole wave functions in the exciton state are localised by the Coulombic binding force, Fourier arguments require that a wider spread of wave-vector states

---

[1] Δ is the growth direction component of exchange, effects of the weaker in-plane exchange components are ignored. They give rise to further splittings which are the subject of chapter 6.

(of the order of the inverse Bohr radius, ~15.10^7 m^{-1} in GaAs wells [5]) be sampled by the single particles compared to when in the unbound (quasi plane-wave) states. This would modify τ_h^{-1} and τ_e^{-1} (rates pertaining to single particle processes modified by the effects of exciton binding are denoted W_e and W_h) and values measured for unbound particles would be inappropriate for single particle processes inside the exciton. More importantly, single particle spin-flip within an exciton is strongly inhibited by the requirement of transfer of an amount of energy Δ to overcome the exchange splitting [6].

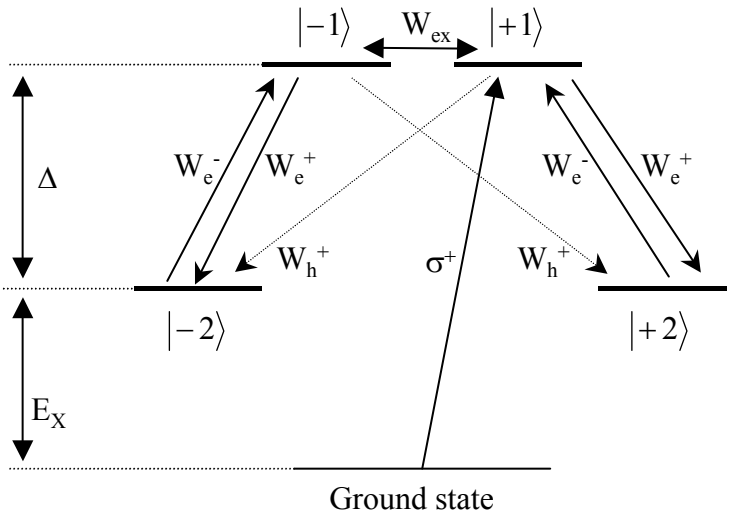

Figure 5.1: Schematic of the energy structure of the heavy-hole exciton spin states, $|J^{ex}_z>$. Parameters $W_e^{\pm}$, $W_h^{\pm}$, are the rates for exciton spin relaxation via the single particle channels of electron and hole spin flip respectively, and W_{ex} is the rate of the mutual e-h (exciton) exchange spin flip mechanism. Superscripts + and – indicate the thermodynamic factor required to overcome the exchange energy Δ (typically ~ 200 μeV), and E_X is the optical energy of the heavy-hole exciton state, energies are not to scale.

An important model of exciton spin relaxation due to Maialle et. al [3] considers the effects of single particle electron and hole spin relaxation and correlated electron-hole exciton spin flip on the evolution of occupation of the four exciton spin states. To account for the exchange splitting of the optically active and inactive heavy-hole exciton spin states by energy Δ (figure 5.1), which necessitates energy interchange during separate electron or hole spin-flips within tightly bound excitons, a thermodynamic factor scales the single particle spin-flip rates:

$$W_{e,h}^{\pm} = W_{e,h}.[1 + \exp(\pm\Delta_h/k_BT)]^{-1}. \quad (5.1)$$

where the symbol $W_{e,(h)}$ is the single particle spin-flip time of the electron (hole) when bound in an exciton state (it would equal $\tau_{e,(h)}^{-1}$ in the limit of zero exciton binding energy); and $W_{e,(h)}^{\pm}$ is the rate of electron (hole) spin-flip which results in the transition between exciton states as indicated by the arrows in figure 5.1.

The exchange spin-flip of the exciton, at rate W_{ex}, is driven by two factors, a long and a short range interaction. The short-range contribution is expected to be of the order of 50 times weaker than the long-range exchange interaction [3]. The short range contribution to exchange involves mutual spin-exchange between the electron and hole within the exciton, converting a heavy- into a light-hole exciton in a weak process:

$$|3/2, -1/2> \rightarrow |1/2, 1/2>. \quad (5.2)$$

Because of mixing of the hh-lh valence sub-bands away from $\underline{k} = 0$, expressed by the quantum amplitude $<-3/2, 1/2|$hh-lh mixing at $k\neq0|1/2, 1/2> \neq 0$, the increased bandwidth of wave-vector space sampled by the hole when bound in the exciton state implies that a finite amplitude channel for heavy-hole exciton spin-flip between the optically active states via short-range exchange exists in the form of a two-step process:

$$|3/2, -1/2> \rightarrow |1/2, 1/2> \rightarrow |-3/2, 1/2>. \quad (5.3)$$

Exchange has in addition a long-range manifestation; as off-diagonal matrix elements in the exciton spin Hamiltonian which directly mix the optically active heavy-hole exciton spin states. Long range spin mixing has a strength proportional to the exciton in-plane wave-vector; it can be regarded as an effective magnetic field acting transverse to the optically-active exciton spin states, causing precession. Momentum scattering can then produce a motional narrowing dynamic to the exciton spin relaxation in much the same way as for electrons experiencing the conduction band spin-splitting (see chapter 4). Exciton spin relaxation via the exchange interaction should therefore be exponential with rate [3]:

$$W_{ex} = \Omega_{\|}^{2}.\tau^{*}, \tag{5.4}$$

as long as the condition:

$$\Omega_{\|}\tau^{*} << 1, \tag{5.5}$$

holds, where $\Omega_{\|}$ is the exchange induced spin mixing and τ^{*} is the exciton in-plane centre-of-mass momentum scattering time. Depending on the relative sizes of W_{ex} and $W_{e,h}$ spin may relax with either a single or double exponential decay.

Vinattieri et al. have studied [7] low temperature exciton dynamics in GaAs quantum wells experimentally, and extended the 4-state model of Maialle et al. to one with 8-states. Their extra four states represent those excitons with wave-vector large enough that they do not interact with light, and become populated due to phonon absorption (thermalisation). They observed a fast spin decay, which they attribute to W_{ex}, and a two component decay in the intensity. Interpreting the intensity decay, they associated the fast component to enhanced radiative recombination of small wave-vector excitons ($K_{\|}$) and the long-lived component to the repopulation of low $K_{\|}$ states by the slower phonon-emission process. Through application of an electric field in the growth direction they observed the development of a tail in the spin signal. Its decay time was unchanged, but that of the faster component reduced, with

increasing electric field. This was explained as due to the decrease of overlap of the electron and hole wave-functions and thus a reduction in the exchange interaction (i.e. W_{ex} reduces with applied electric field but $W_{e,h}$ are relatively unaffected). This electric field dependence provided strong evidence that both exciton and uncorrelated spin flips can play a role in the relaxation of exciton spin polarisation, but that with no electric field applied $W_{ex} >> W_{e,h}$.

5.2.2 Effects of temperature

At temperatures lower than ~ 40 K exciton localisation within the plane of a quantum well affects the temperature dependence of many mechanisms, in particular those whose strengths are wave-vector dependent. Interruption between growth of the well and barrier layers for times of the order of 100 seconds allows settling of the deposited atoms and for the formation of smooth islands in the interface plane with monatomic thickness and a lateral extent of the order of the exciton Bohr radius. These fluctuations in the width of the quantum well provide sites of exciton localisation and result in an inhomogeneous broadening of the exciton emission spectrum and a Stokes shift between the peak of absorption and emission [8,9,10], both of the order of a few meV. Similar localisation effects can result from alloy disorder and aggregation in the structure.

One of the main differences between InGaAs/GaAs and GaAs/AlGaAs quantum wells is that the alloy disorder occurs in the well for the former, due to the indium location. Low temperature localisation is increased by both interface roughness and alloy disorder. Due to the alloy location, scattering by alloy fluctuations is stronger in the well than the barrier for InGaAs/GaAs. Since the amplitude of the exciton wave-function in the well increases (for shallow, narrow wells) with increasing well width, the exciton mobility is lower in wider wells. An opposite dependence is expected in GaAs/AlGaAs structures [11]. Indeed, measurements

[3, 12] show that the low temperature exciton mobility is an order of magnitude lower in InGaAs/GaAs than in GaAs/AlGaAs for wide wells and the opposite is true for narrow wells.

Takashi et al. have studied [11] the temperature and well width dependences of exciton scattering in InGaAs/GaAs quantum wells and compared the results with those obtained in GaAs/AlGaAs wells. They found that the low temperature radiative decay time in InGaAs/GaAs was nearly constant with well width, decreasing by at most 20 % from 20 to 100 Å (figure 3 of ref. 11) and suggested that there may by some compensation between the effects of decreasing Bohr radius and decreasing overlap integral in the determination of the radiative decay time (T_R), related by [13, 11]:

$$T_R^{-1} \sim A_c|\int f_e(z)f_h(z)dz|^2/a_0^2(L_z), \qquad (5.6)$$

where A_c is the exciton coherence area, a_0 is the exciton Bohr radius and $f_{e,h}$ are the electron and hole envelope wave functions in the growth direction.

Hegarty et al. [8] have shown in GaAs/AlGaAs quantum wells that states with energy lower than the inhomogeneous line centre are localised and those with higher energy are delocalised (itinerant) – the two regimes being separated by a sharp mobility edge at the line centre. Localisation can increase the dephasing time of excitons by about a factor of 10 [14] to ~70 ps.

Thus two classes of exciton can be distinguished, localised and itinerant. Mechanisms of spin and radiative decay are influenced strongly by the amount of localisation of the exciton population. The exchange driven motional narrowing spin relaxation mechanism of Maialle et al. [3] ought to be inhibited for strongly localised excitons since their in-plane wavevector is small. Malinowski et al. [1] measured the exciton spin relaxation rate at 5 K in two GaAs/AlGaAs samples, one indicating localisation and the other not. The results illustrated that exciton localisation decreases the exciton spin relaxation rate by a factor of ~100. The exciton radiative life-time is also extended, by around a factor of 3 [15].

At high temperatures resonantly excited excitons become thermodynamically unstable. The ratio of unbound to bound e-h pairs at equilibrium in quantum wells is given by the Saha equation [16]:

$$N_e N_h / N_x = \mu_r k_B T . \exp(-E_B / k_B T) / 2\pi \hbar^2, \qquad (5.7)$$

where N_e, N_h and N_x are the densities of unbound electrons, holes and of bound e-h pairs respectively, μ_r is the reduced electron-hole mass and E_B is the exciton binding energy.

When the optical phonon (OP) states are significantly populated the exciton-OP scattering rate increases. Having typical energies of ~ 30 meV, about three times the exciton binding energy, this scattering causes ionisation of the exciton constituents into unbound (free) e-h states where the electron and hole occupy plane wave states. Once the exciton is ionised the spin relaxation should occur at the separate rates τ_h^{-1} and τ_e^{-1}.

In contrast to relatively deep GaAs/AlGaAs and InGaAs/InP, the low indium content InGaAs/GaAs wells studied in this chapter are shallow enough that thermal emission of the electron and/or hole from the well into the barrier becomes relevant at relatively low temperatures. Botha and Leitch [17] studied the temperature dependence of the photoluminescence intensity as a function of temperature in $In_{0.19}Ga_{0.81}As/GaAs$ wells and found that the onset of intensity decrease occurs when the temperature is high enough to eject the least confined carrier (the hole) from the well. In their data, emission of holes onsets at ~65 and 100 K in well widths of 33 and 100 Å respectively.

Classically, a particle bound in a potential well may escape with significant probability if it can acquire the energy to do so, illustrated in figure 5.2. The depth of the potential trapping the electron, the well depth (ΔE_C), and that trapping the hole (ΔE_V) are related by:

$$Q = \Delta E_C / \Delta E_g, \text{ and} \qquad (5.8)$$

$$1-Q = \Delta E_V / \Delta E_g,$$

where Q is the conduction band offset ratio and ΔE_g is the difference of the fundamental band gap of the well and barrier materials:

$$\Delta E_g = E^B{}_g - E^W{}_g. \tag{5.9}$$

Neglecting the exciton binding energy the activation energies ought roughly to be:

$$\begin{aligned} E^h{}_A &\approx \Delta E_V - E_{1h}, \text{ and} \\ E^e{}_A &\approx \Delta E_C - E_{1e}. \end{aligned} \tag{5.10}$$

If the activation energies $E^h{}_A$ or $E^e{}_A$ are less than the longitudinal optical phonon (LO) energy, then it may be expected that the hole and/or electron will be emitted from the well into the barrier following a single exciton-LO phonon scattering event.

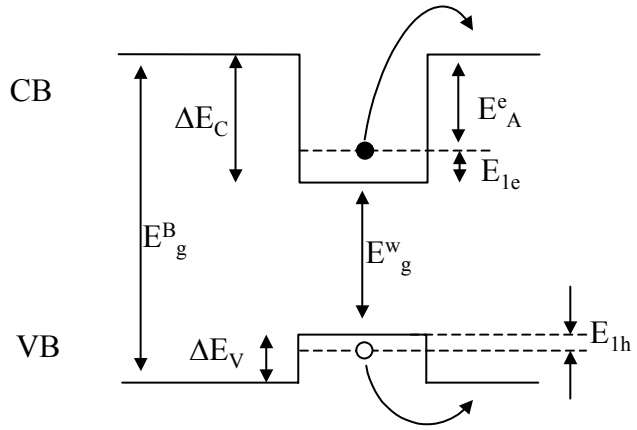

Figure 5.2: Schematic diagram of the electron and hole in the ground conduction and valence band bound states of a potential well which considers the particle escape process classically. The energies indicated are the conduction band well depth (ΔE_C), valence band well depth (ΔE_V), fundamental band gap of the well ($E^B{}_g$) and barrier materials ($E^B{}_g$), the electron (E_{1e}) and hole quantum confinement energies (E_{1h}), and the activation energies required to put the electron ($E^e{}_A$) or hole ($E^h{}_A$) into the barrier.

5.3 Sample description

Sample DB918 was a molecular beam epitaxy (MBE) grown InGaAs/GaAs multi-single quantum well sample having 11 % indium content in the wells, and with nominal well-widths 30, 60, 100 and 200 Å, separated by 300 Å GaAs barriers. The structure was grown on an n-type GaAs substrate and a 0.5 μm GaAs buffer layer with the 200 Å well closest, separated from the buffer by a 300 Å GaAs barrier layer. Traynor [18] has noted the photoluminescence peak positions and widths, reproduced in table 5.1. The 200 Å well did not show any photoluminescence [19 ,18].

Well width (Å)	PL peak position (eV, nm)	width (meV)
30	1.446, 845.8	3.1
60	1.442, 859.9	3.0
100	1.421, 872.6	2.6

Table 5.1: Photoluminescence peak positions and widths of the hh-exciton at low temperature taken from Traynor [18].

5.4 Experimental procedure

Time-resolved pump-probe spectra were obtained from the 30 and 100 Å wells of the sample over a temperature range of 5 to 150 K using the experimental arrangement described in chapter 3. For each temperature the laser was scanned over the region of the n=1 heavy-hole exciton absorption with the delay set to ~20 ps. Figure 5.3 shows the wavelength dependence of the ΔR and $\Delta\theta$ signals at different delays for the 30 Å well at 10 K, from which it is clear that the wavelengths of strongest probe rotation and reflectivity change did not coincide exactly. The time-resolved spectra were measured with the laser tuned to the best compromise of signal strength. Circularly polarised pump pulses excited a spin polarisation that was probed

by delayed linearly polarised probe pulses. Rotation of the plane of polarisation of the probe and its change in reflection intensity were recorded as a function of the pump-probe delay. Signal strengths decreased rapidly with increasing temperature and the signals were undetectable above 150 K.

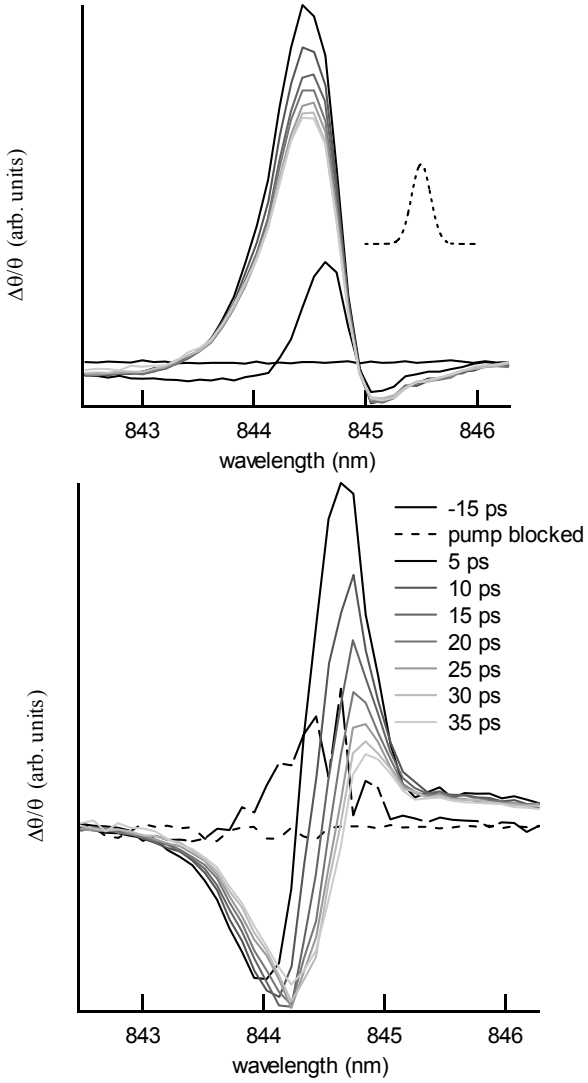

Figure 5.3: Non-linear response (reflectivity change, top, and probe rotation, bottom) at 10 K as the laser was scanned over the resonance of the 30 Å $In_{0.11}Ga_{0.89}As$ well for different pump-probe delays. Inset of upper plot illustrates the spectral width of the pulse, ~0.12 nm FWHM based on Fourier limited 2 ps duration.

5.5 Results

The two measured signals (ΔR and $\Delta\theta$) are displayed (figures 5.4 to 5.22) along with the derived spin signal ($\Delta\theta/\Delta R$) and, where a satisfactory fit was possible, the exponential decay function used to extract the decay rates.

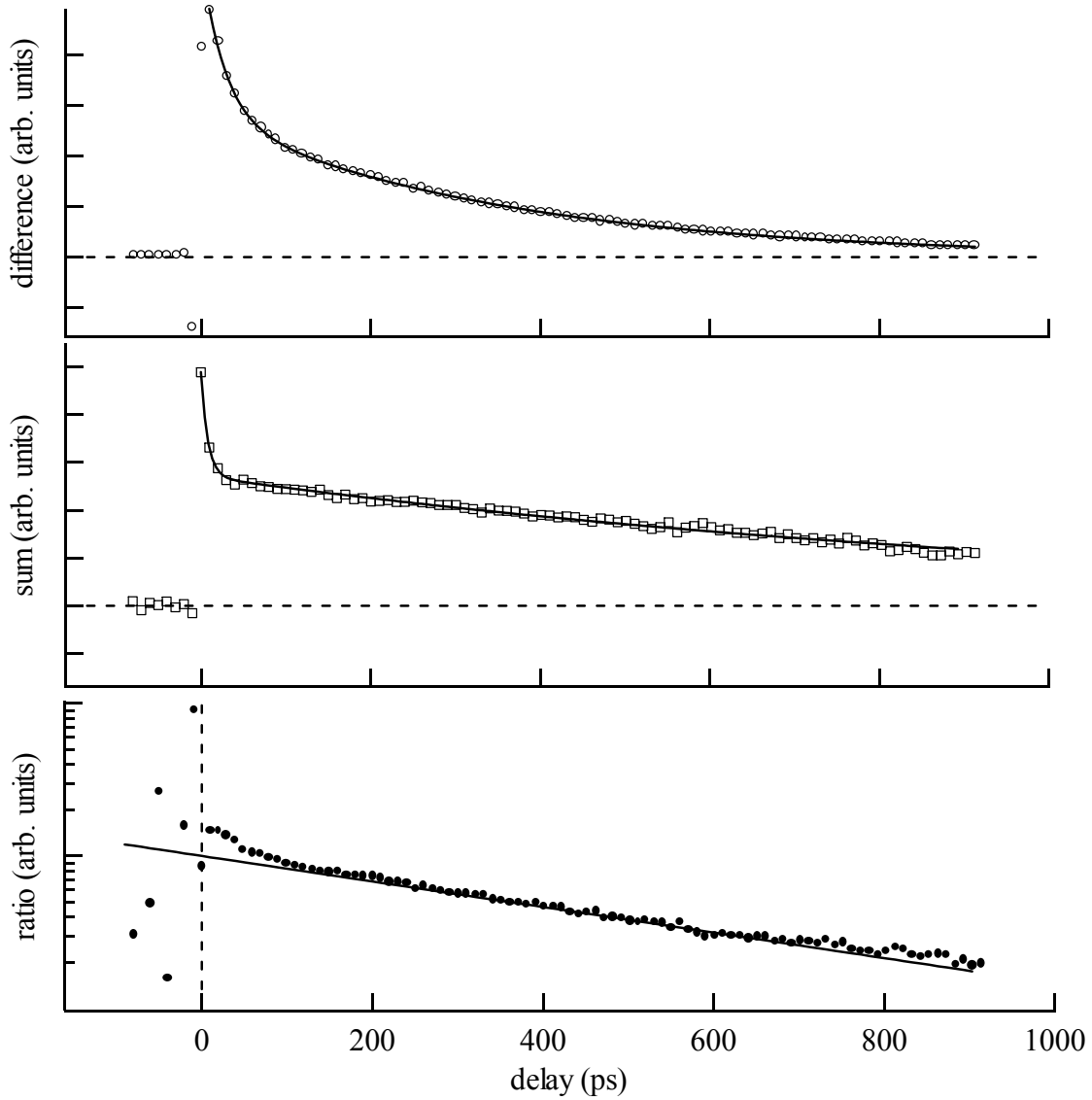

Figure 5.4: Plots with linear scales of time-resolved $\Delta\theta$ (top, circles) and ΔR signals (middle, squares) at 5 K in the 30 Å $In_{0.11}Ga_{0.89}As$ quantum well of sample DB918 with fits (lines), and (bottom, closed circles) semi-logarithmic plot of evolution of the spin signal, defined as the ratio of difference to sum, with single exponential decay (line) of rate equal to the difference of the long-lived components of the difference and sum signals.

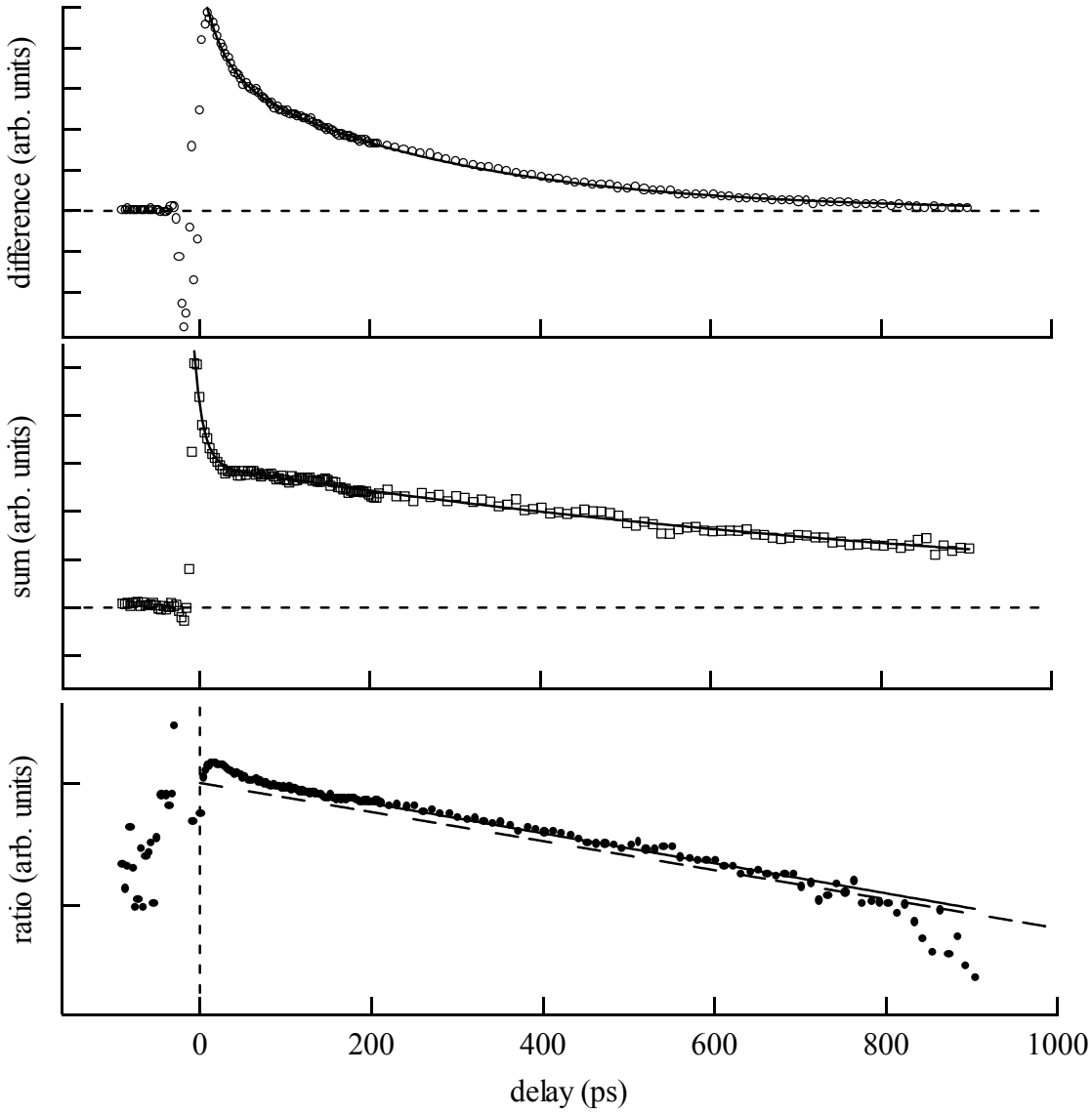

Figure 5.5: Plots with linear scales of difference (top, circles) and sum signals (middle, squares) at 10 K in the 30 Å $In_{0.11}Ga_{0.89}As$ quantum well of sample DB918 with fits (lines), and (bottom, closed circles) semi-logarithmic plot of the spin signal evolution with single exponential decay (dashed line) of rate equal to the difference of the long-lived components of the difference and sum signals and exponential fit (solid line).

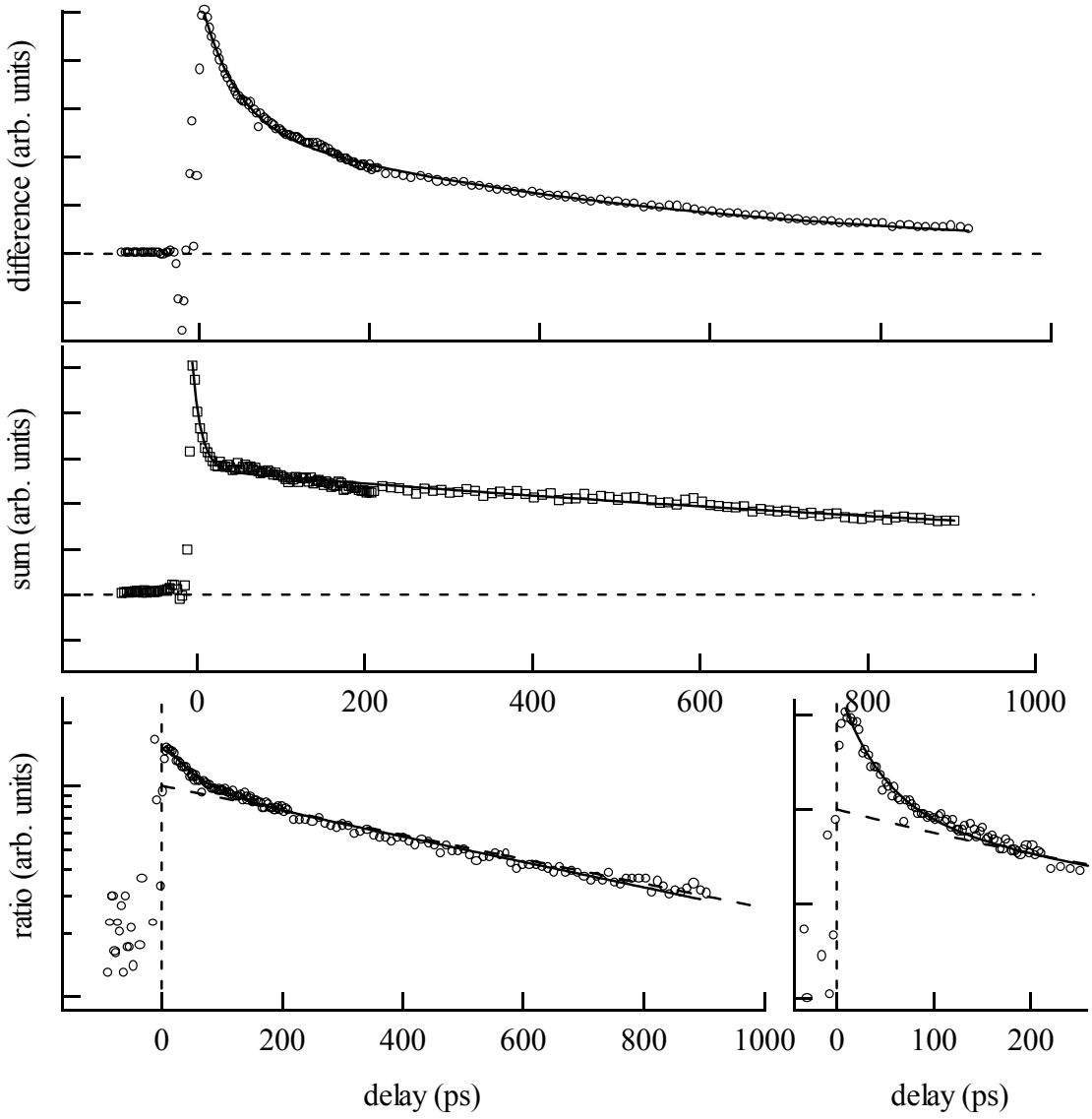

Figure 5.6: Plots with linear scales of difference (top, circles) and sum (middle, squares) signals at 30 K in the 30 Å $In_{0.11}Ga_{0.89}As$ quantum well of sample DB918 with fits (lines), and (bottom, open circles) of the spin signal evolution with single exponential decay (dashed line) of rate equal to the difference of the long-lived components of the difference and sum signals and a two-component exponential fit (solid line). Bottom right displays the spin evolution over the first 200 ps with linear axis scales.

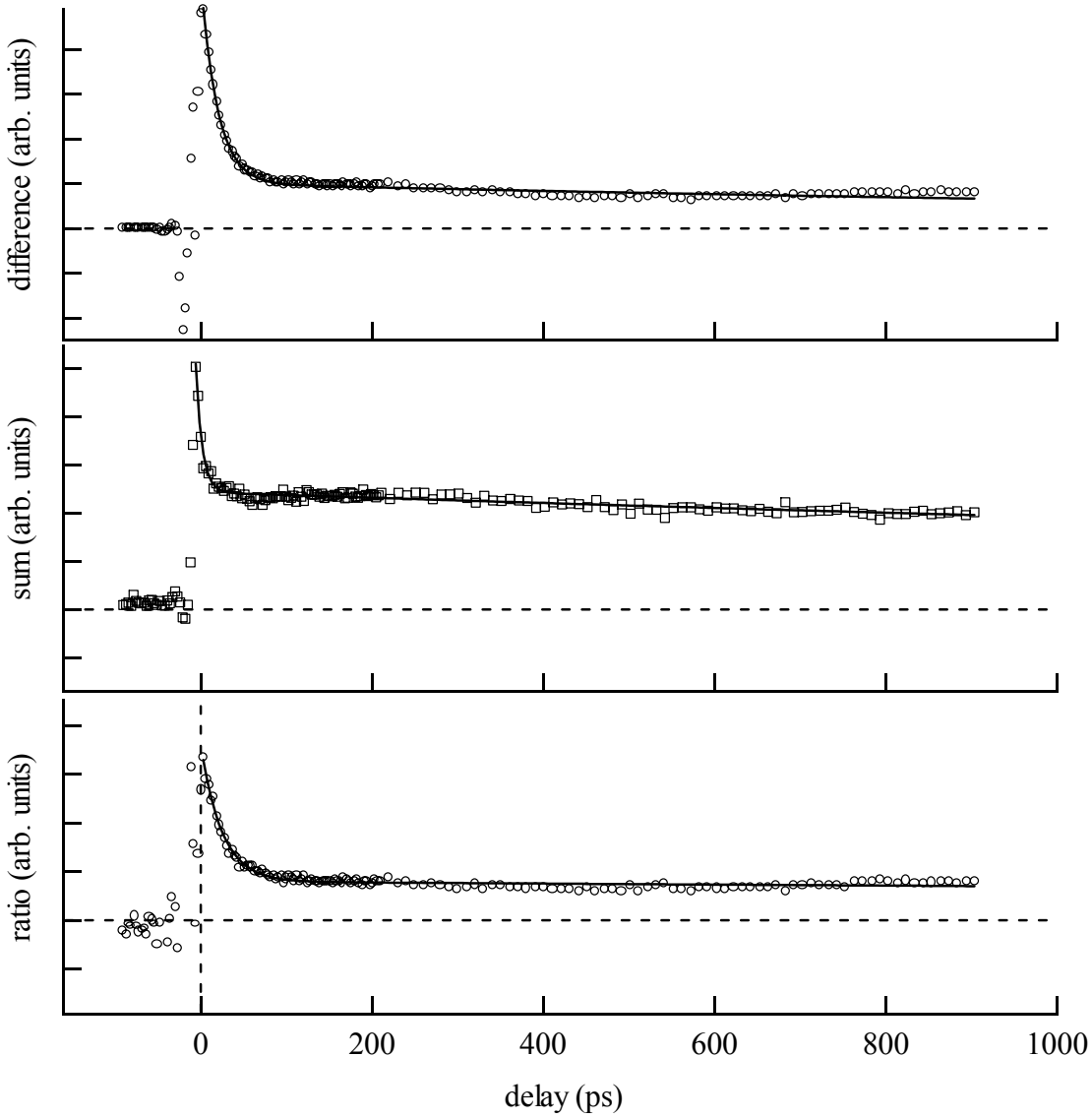

Figure 5.7: Plots with linear scales of difference (top, circles) and sum (middle, squares) at 50 K in the 30 Å $In_{0.11}Ga_{0.89}As$ quantum well of sample DB918 with fits (lines), and (bottom, circles) of the spin signal evolution with exponential fit (solid line).

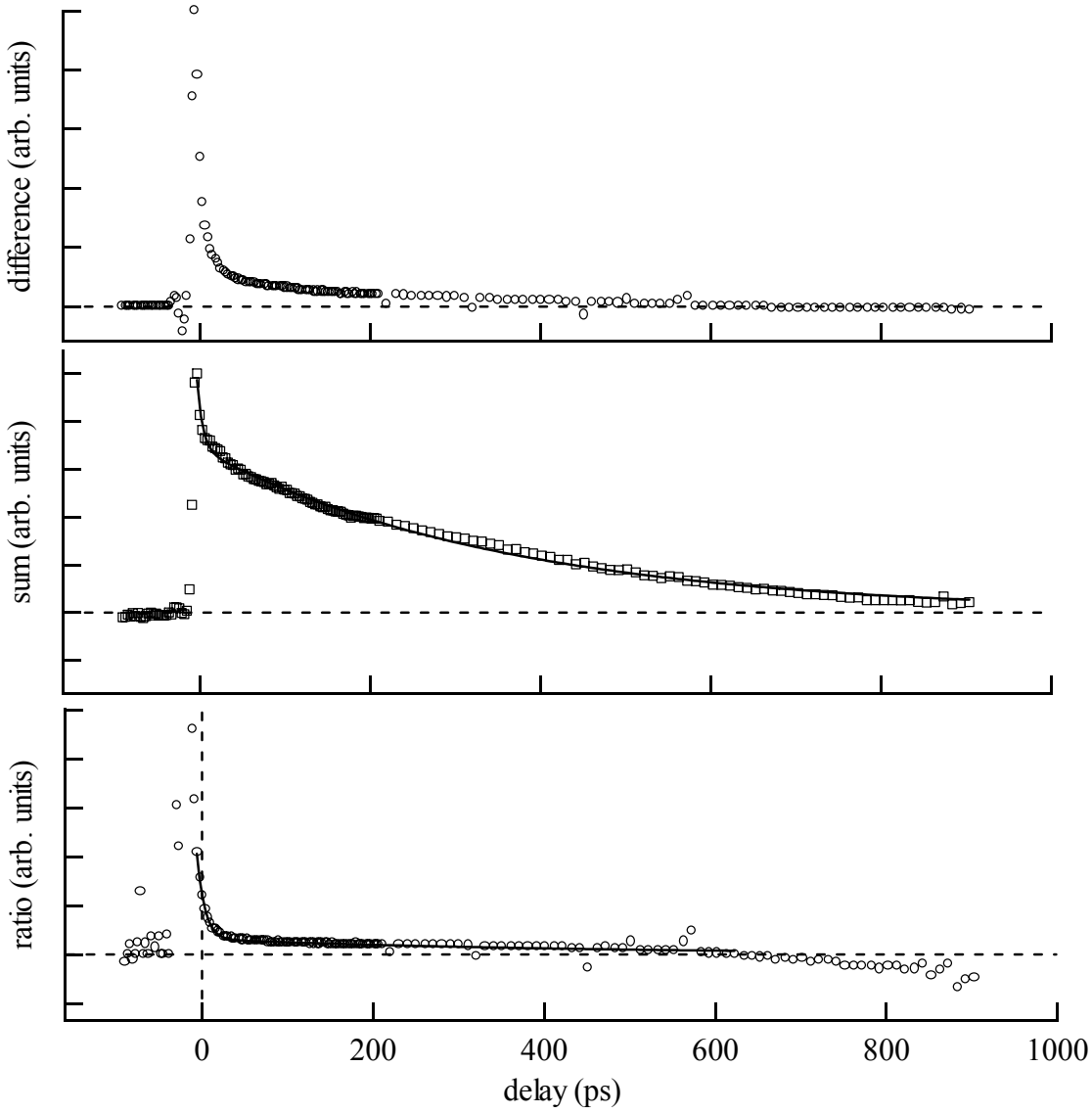

Figure 5.8: Plots with linear scales of difference (top) and sum (middle, squares) with fit (line) at 65 K in the 30 Å In0.11Ga0.89As quantum well of sample DB918, and (bottom, circles) of the spin signal evolution with exponential fit (solid line) up to ~ 400 ps.

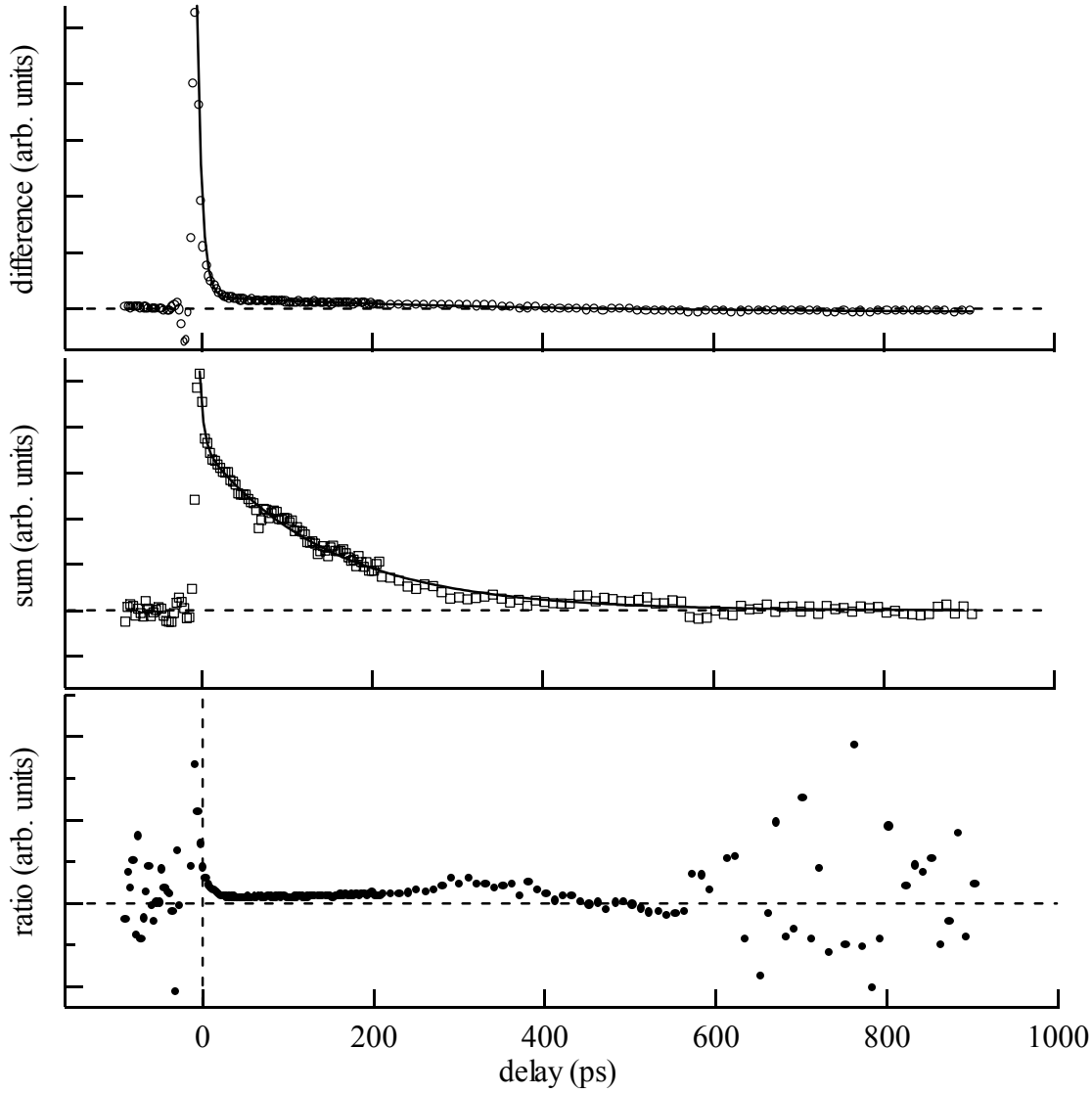

Figure 5.9: Plots with linear scales of difference (top) with fit (line) and sum (middle, squares) at 80 K in the 30 Å $In_{0.11}Ga_{0.89}As$ quantum well of sample DB918, and (bottom, circles) of the spin signal evolution.

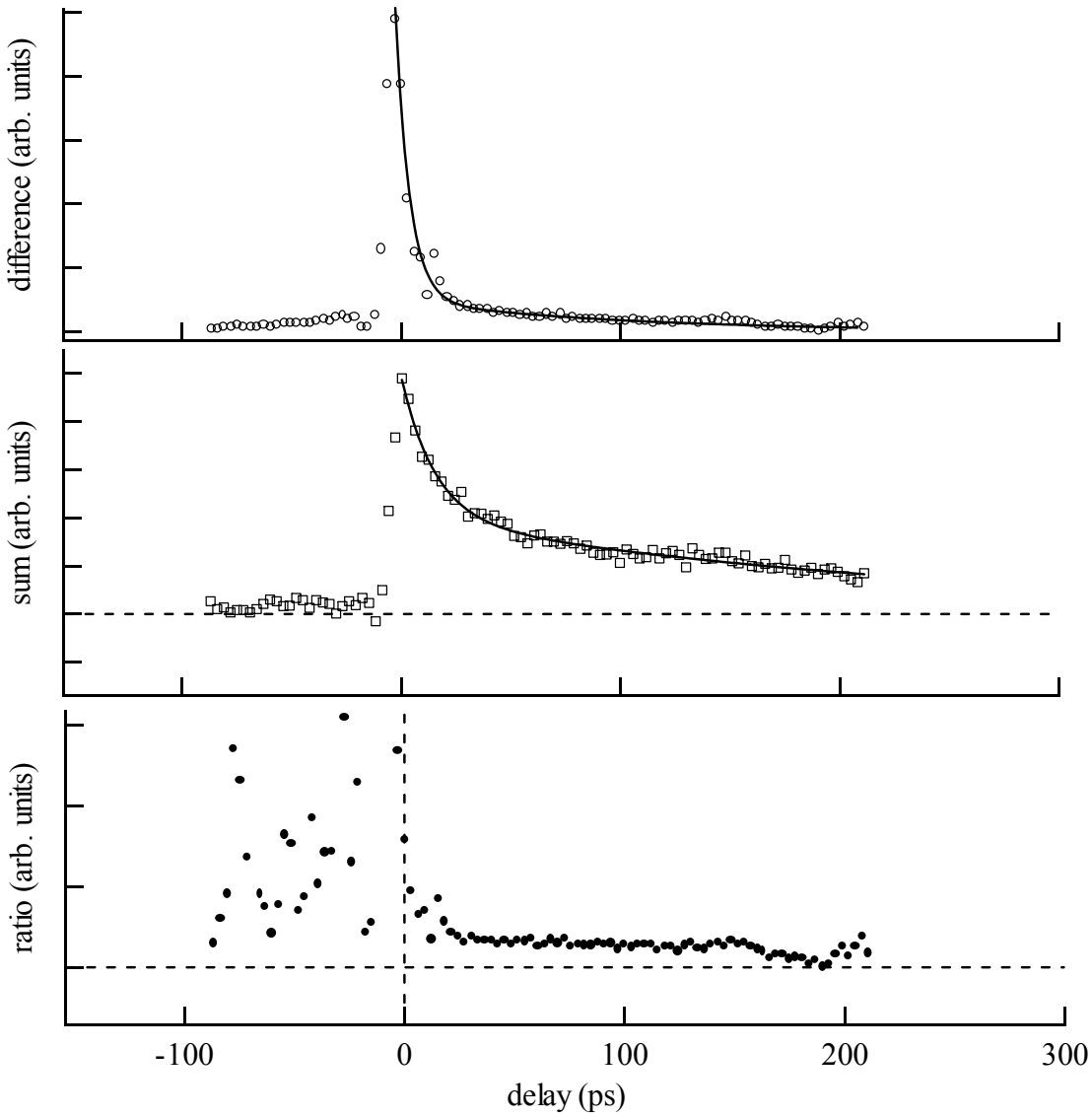

Figure 5.10: Plots with linear scales of difference (top) and sum (middle, squares) with fits (lines) at 100 K in the 30 Å $In_{0.11}Ga_{0.89}As$ quantum well of sample DB918, and (bottom, circles) of the spin signal evolution.

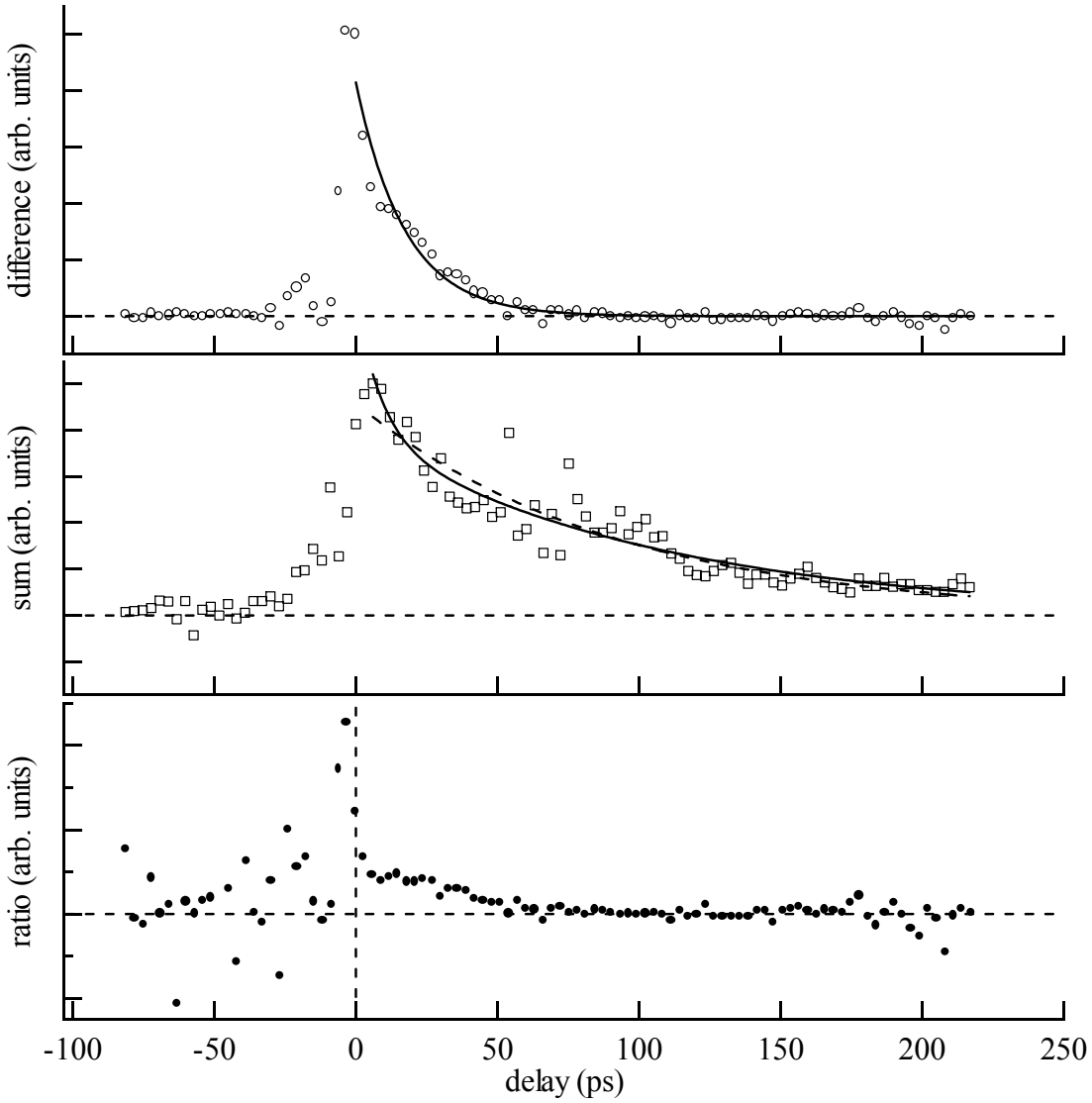

Figure 5.11: Plots with linear scales of difference (top) and sum (middle, squares) with fits (two-component decays solid lines, single component dashed) at 120 K in the 30 Å $In_{0.11}Ga_{0.89}As$ quantum well of sample DB918, and (bottom, circles) of the spin signal evolution.

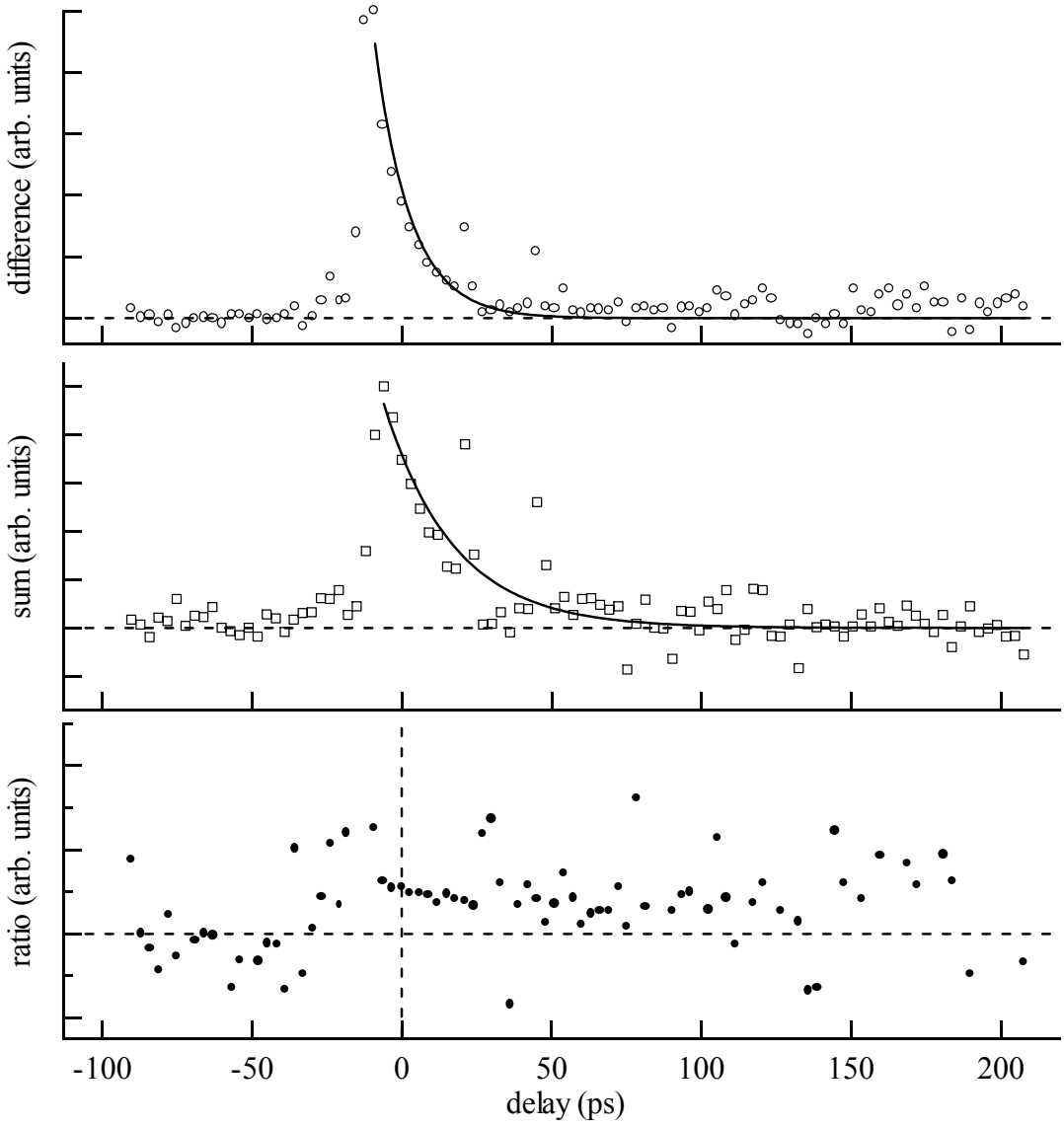

Figure 5.12: Plots with linear scales of difference (top, circles) and sum (middle, squares) with fits (lines) at 150 K in the 30 Å In0.11Ga0.89As quantum well of sample DB918, and (bottom, circles) of the spin signal evolution.

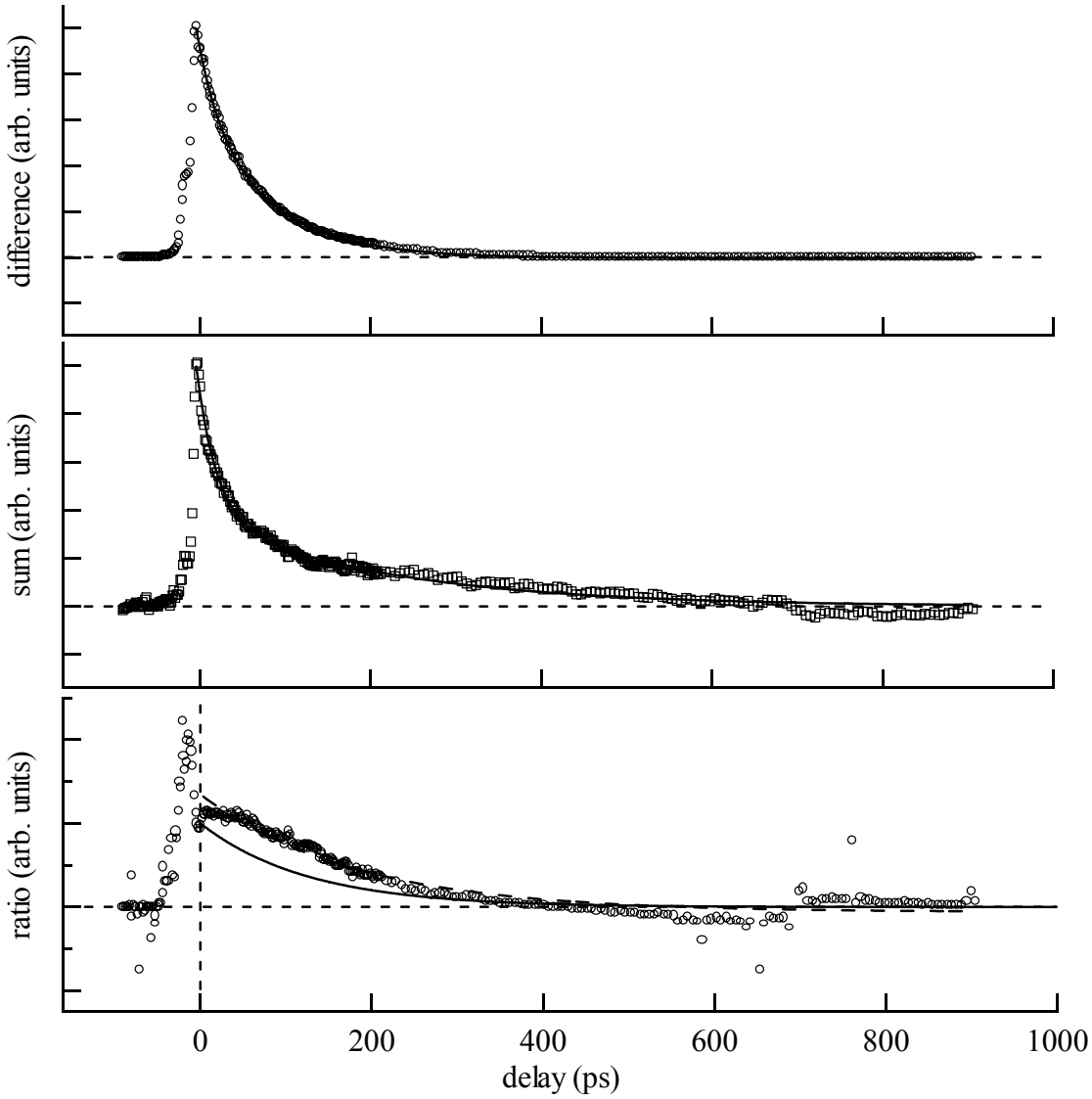

Figure 5.13: Plots with linear scales of sum (top, circles) and difference (middle, squares) signals at 10 K in the 100 Å $In_{0.11}Ga_{0.89}As$ quantum well of sample DB918 with fits (lines), and (bottom, circles) of the spin signal evolution with single exponential decay (solid line) of rate equal to the difference of the long-lived components of the difference and sum signals and a single exponential fit (dashed line). Note that the spin signal decays towards a negative value.

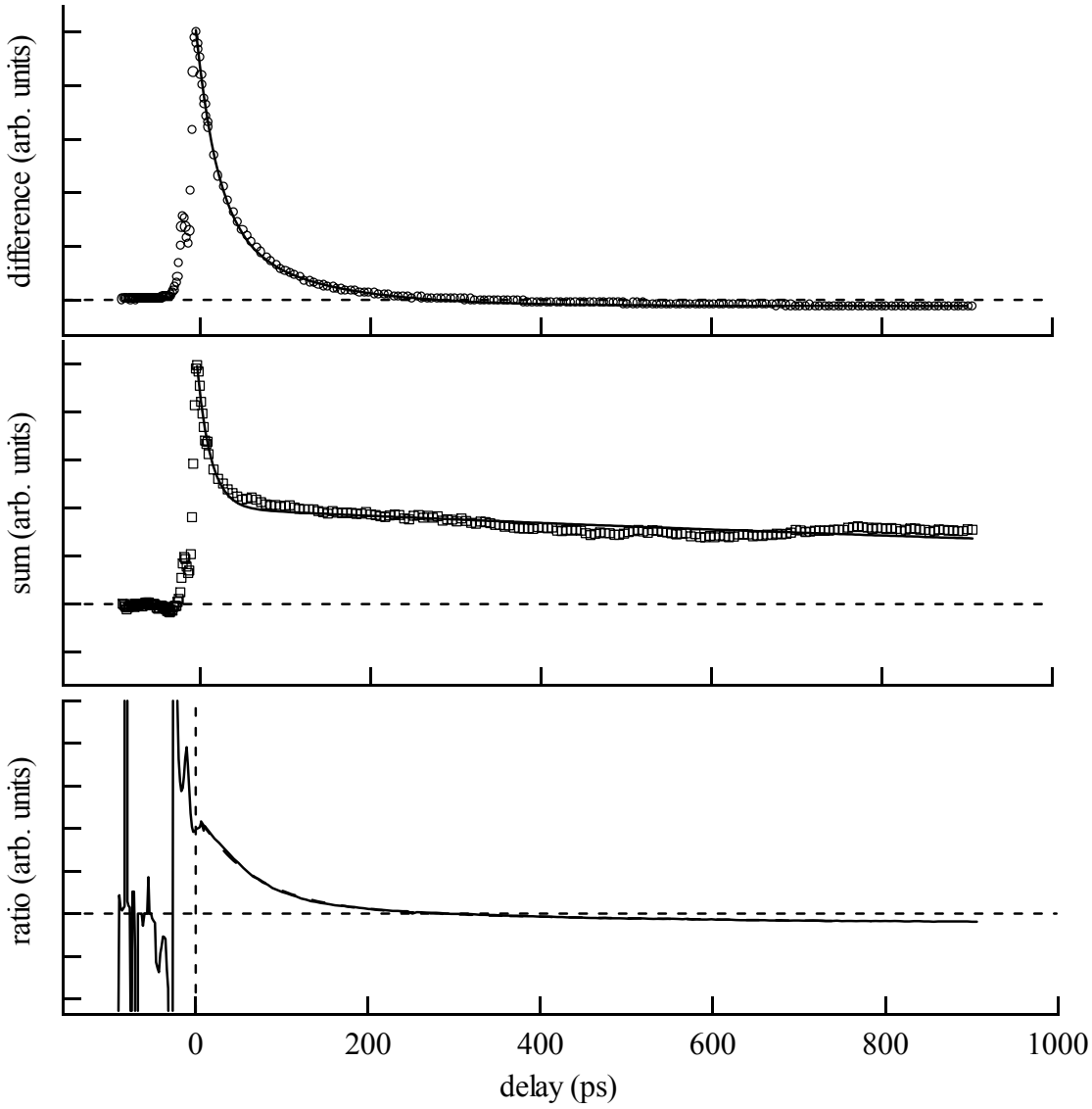

Figure 5.14: Plots with linear scales of difference (top, circles) and sum (middle, squares) at 30 K in the 100 Å $In_{0.11}Ga_{0.89}As$ quantum well of sample DB918 with fits (lines), and (bottom, solid line) of the spin signal evolution with exponential fit (dashed line).

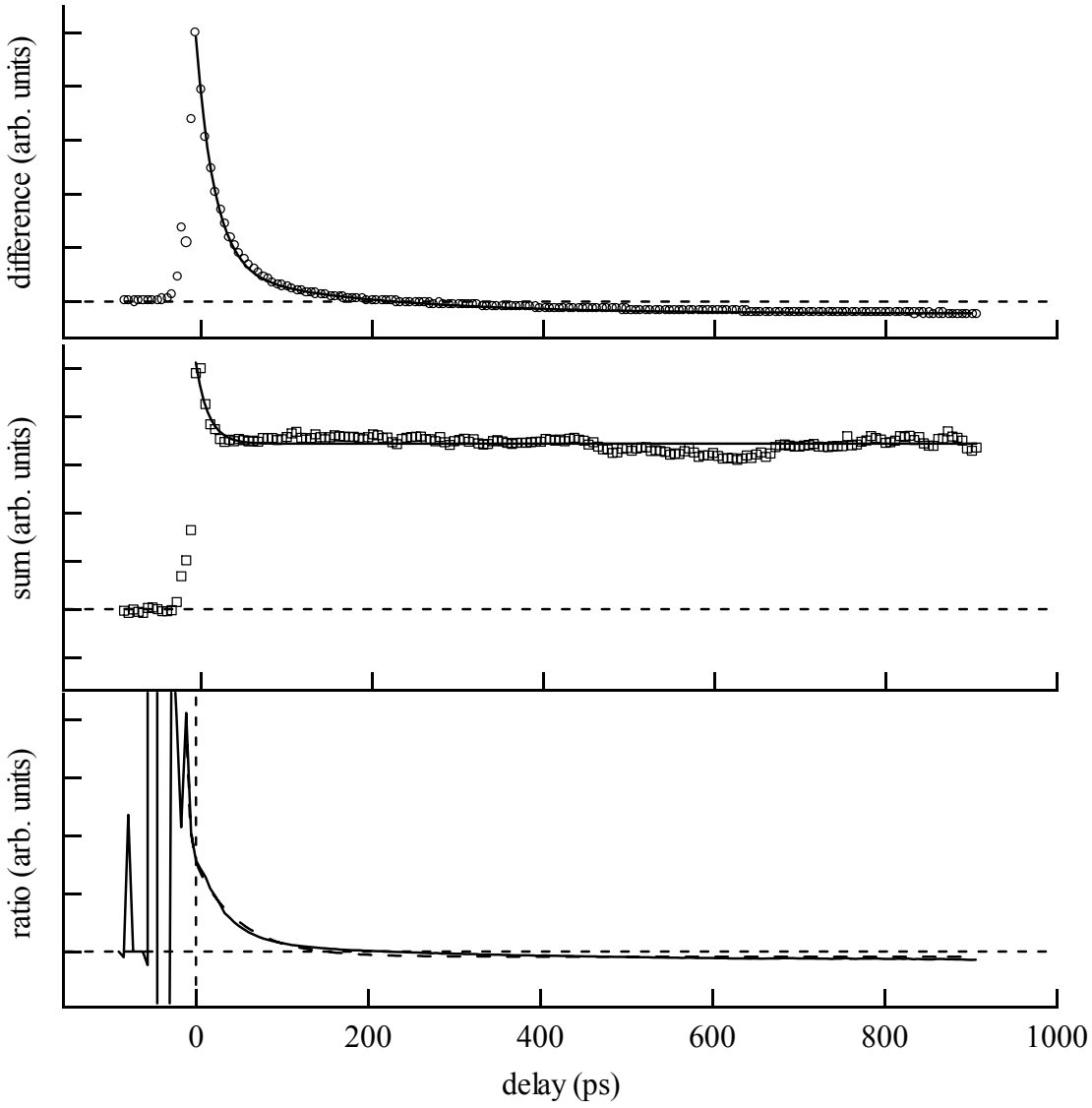

Figure 5.15: Plots with linear scales of difference (top, circles) and sum (middle, squares) at 40 K in the 100 Å $In_{0.11}Ga_{0.89}As$ quantum well of sample DB918 with fits (lines), and (bottom, solid line) of the spin signal evolution with exponential fit (dashed line).

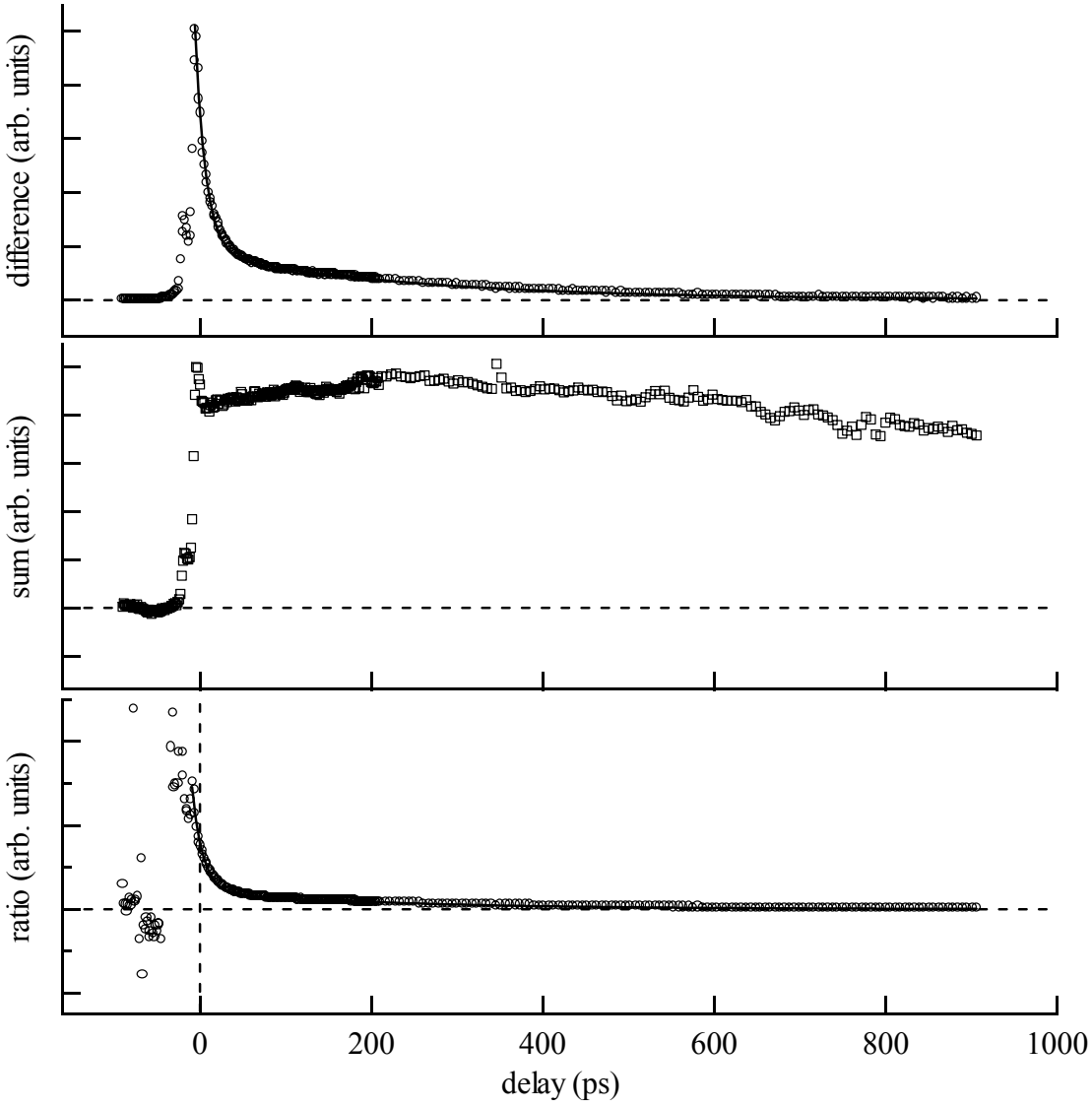

Figure 5.16: Plots with linear scales of difference (top, circles) and sum (middle, squares) at 50 K in the 100 Å $In_{0.11}Ga_{0.89}As$ quantum well of sample DB918 with fit to difference (line), and (bottom, circles) of the spin signal evolution with exponential fit (solid line).

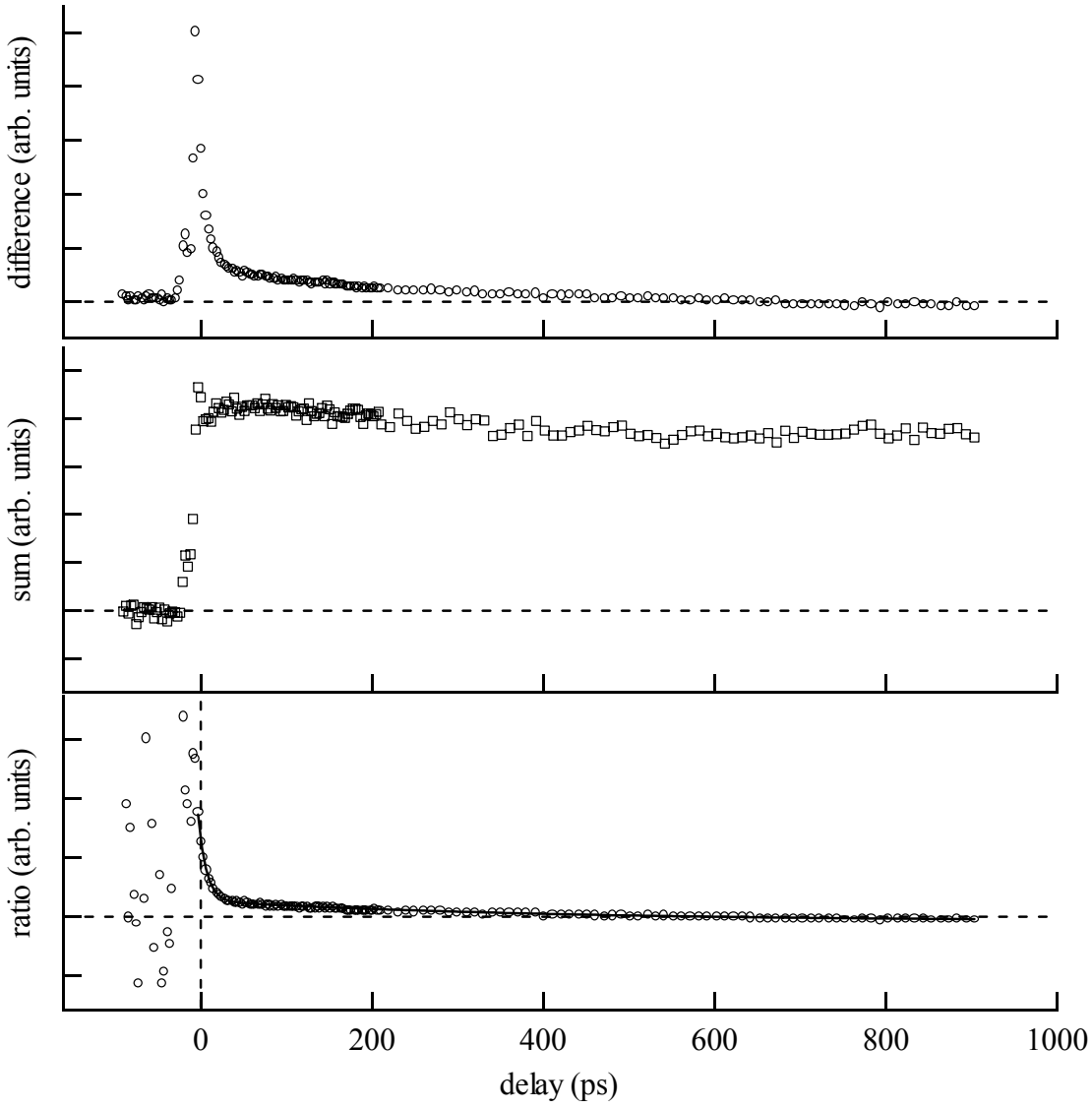

Figure 5.17: Plots with linear scales of difference (top, circles) and sum (middle, squares) at 60 K in the 100 Å $In_{0.11}Ga_{0.89}As$ quantum well of sample DB918, and (bottom, circles) of the spin signal evolution with exponential fit (solid line).

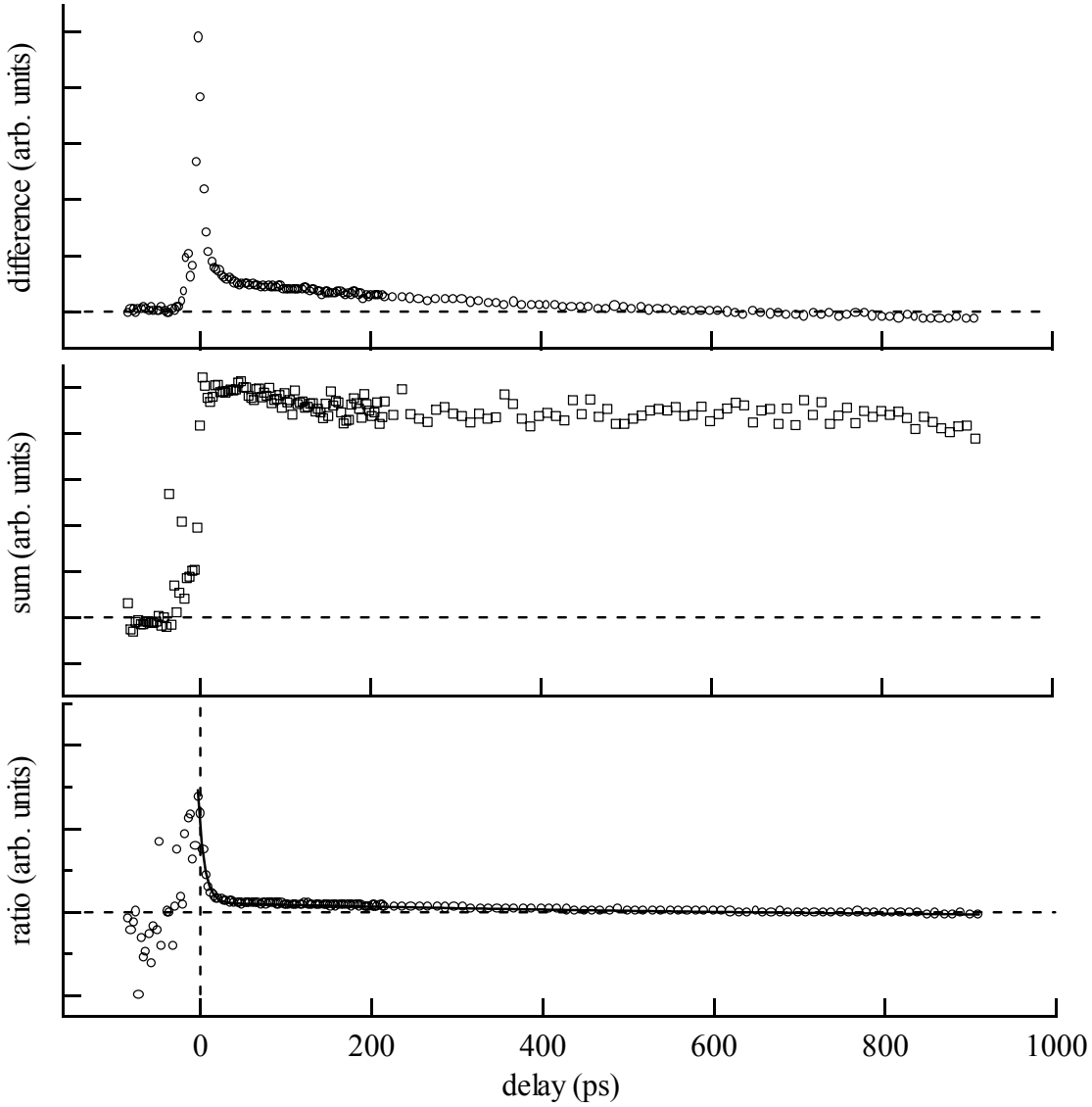

Figure 5.18: Plots with linear scales of difference (top) and sum (middle, squares) at 70 K in the 100 Å $In_{0.11}Ga_{0.89}As$ quantum well of sample DB918, and (bottom, circles) of the spin signal evolution with exponential fit (solid line).

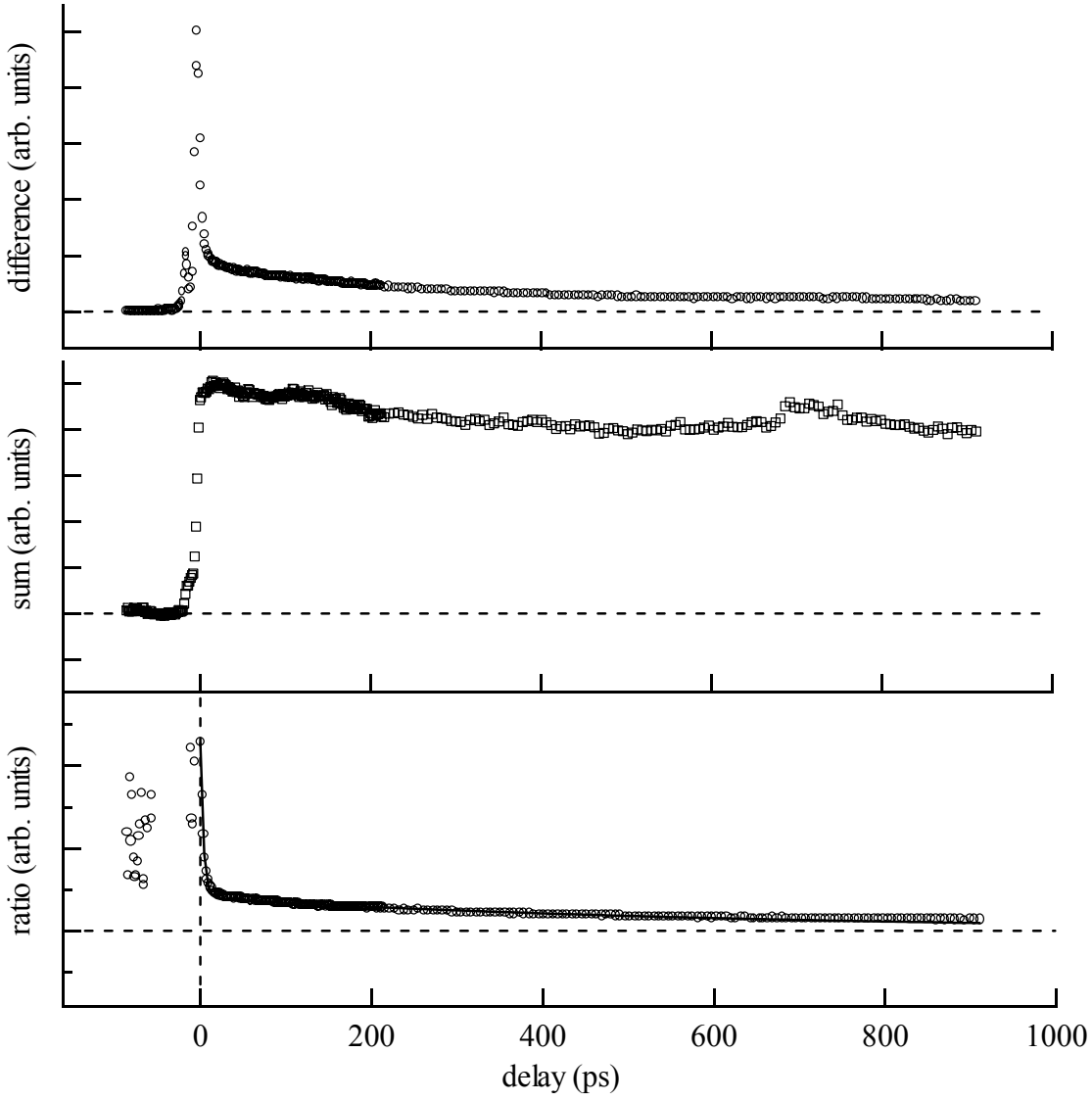

Figure 5.19: Plots with linear scales of difference (top) and sum (middle, squares) at 80 K in the 100 Å $In_{0.11}Ga_{0.89}As$ quantum well of sample DB918, and (bottom, circles) of the spin signal evolution with fit (line).

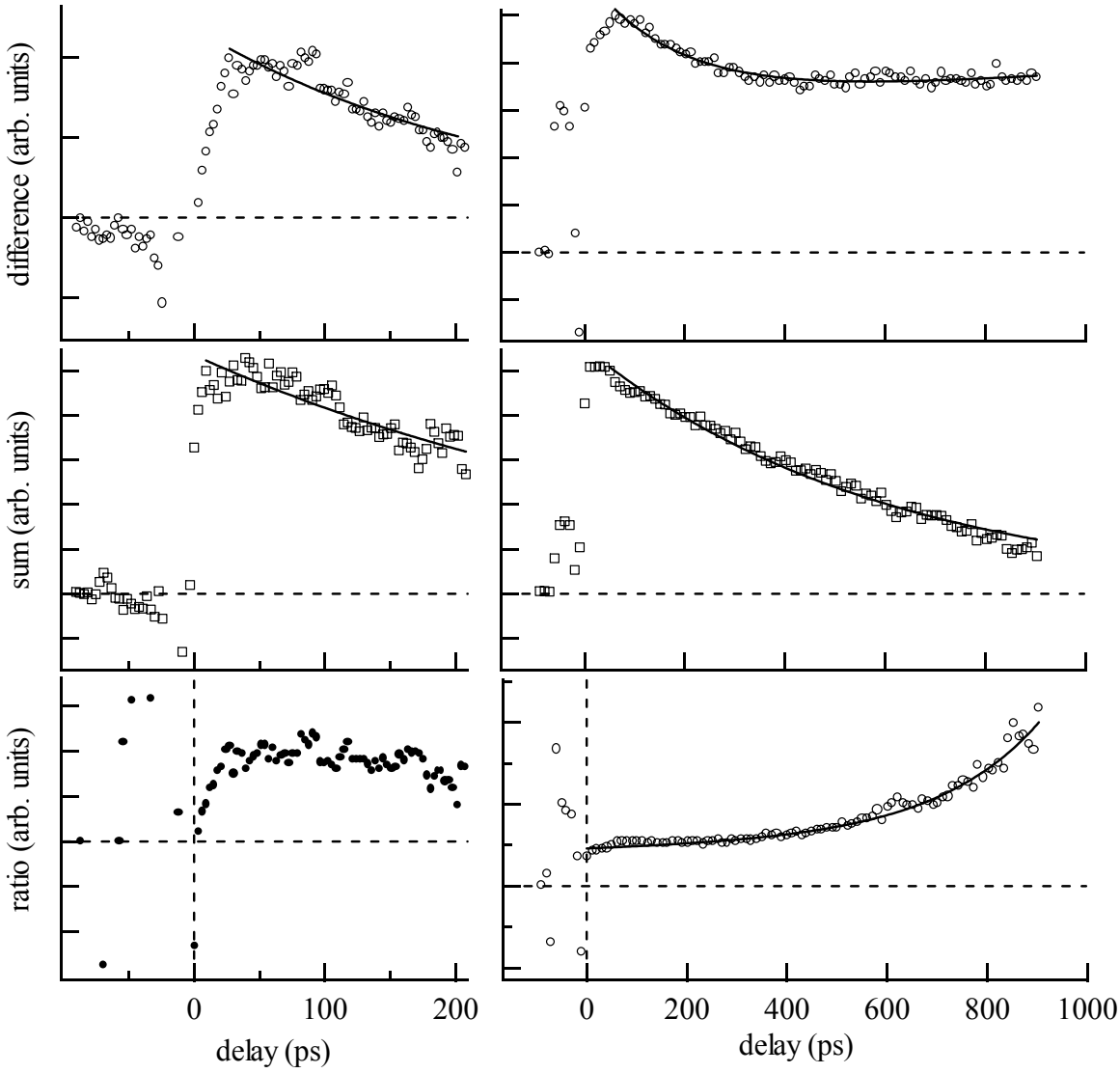

Figure 5.20: Plots with linear scales of difference (top) and sum (middle, squares) with fits (lines) at 100 K in the 100 Å $In_{0.11}Ga_{0.89}As$ quantum well of sample DB918, and (bottom, circles) of the spin signal evolution for two nominally similar consecutive experiments with different ranges of delay.

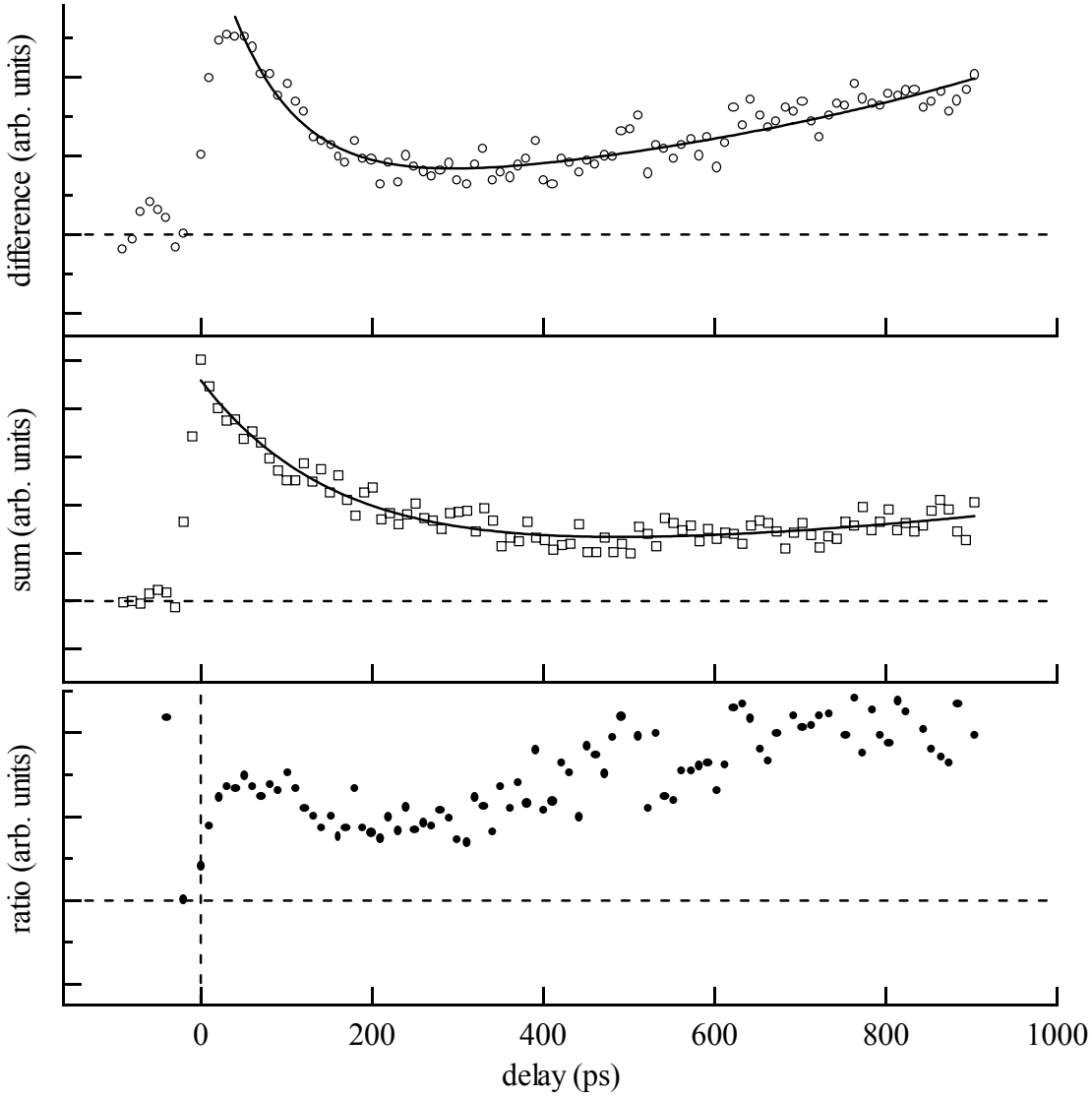

Figure 5.21: Plots with linear scales of difference (top, circles) and sum (middle, squares) with fits (lines) at 120 K in the 100 Å $In_{0.11}Ga_{0.89}As$ quantum well of sample DB918, and (bottom, circles) of the spin signal evolution.

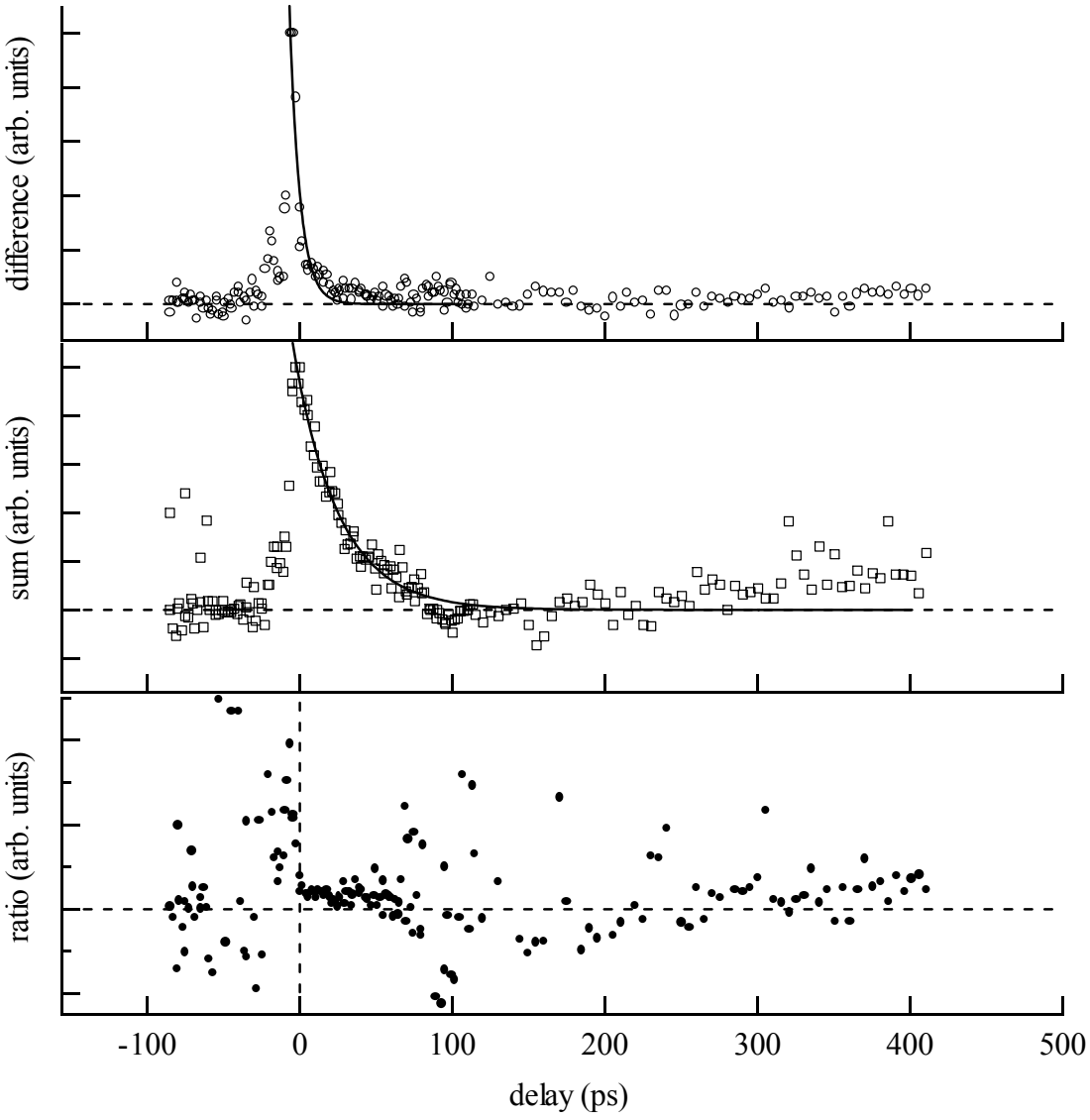

Figure 5.22: Plots with linear scales of difference (top, circles) and sum (middle, squares) with fits (lines) at 150 K in the 100 Å $In_{0.11}Ga_{0.89}As$ quantum well of sample DB918, and (bottom, circles) of the spin signal evolution.

5.6 Analysis

Carrier spin and population dynamic mechanisms are extremely intricate and in general several physical processes occur, at different rates, which themselves can be functions of time. It was possible to obtain good fits to both the $\Delta\theta$ and ΔR decays for most temperatures using double or single exponential decay functions of the form:

$$A_1\exp(-\tau_1 t) + A_2\exp(-\tau_2 t) + A_3, \qquad (5.11)$$

yielding characteristic decay rates for the spin and sum signal decays. In the other cases it is clear that the dynamics were indeed more involved and would require a more intricate analysis to extract sensible values for empirical quantities. Errors reported in the analysis are those from standard non-linear least square fits representing one standard deviation, they are most probably not representative of the greatest errors in the experiment. The fitted decay times are plotted in figures 5.23 to 5.26, other curves in these plots are discussed below.

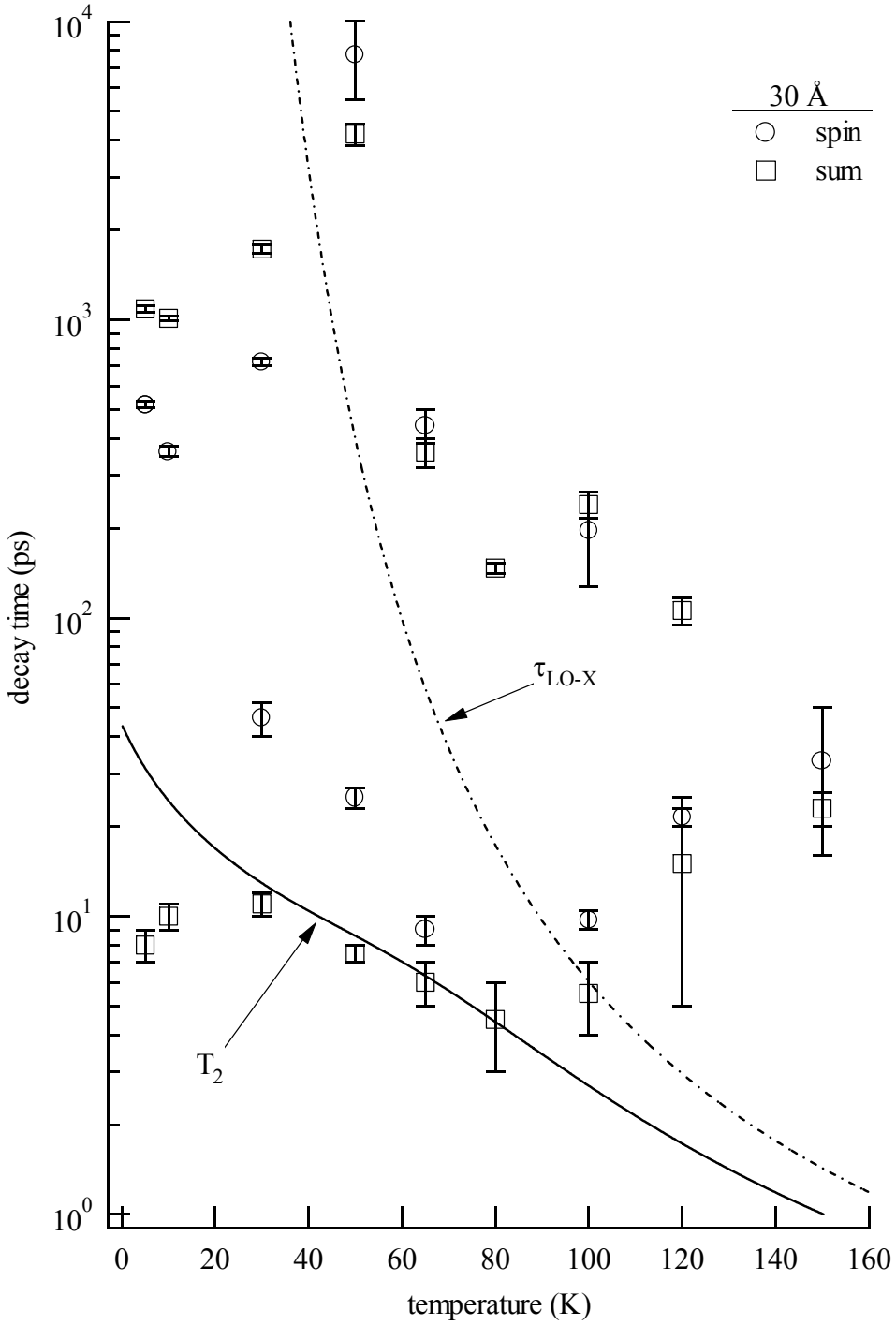

Figure 5.23: Extracted spin (circles) and sum (squares) signal decay times for the 30 Å $InGa_{0.11}/Ga_{0.89}As$ quantum well of sample DB918, estimated thermalisation time T2 (solid curve) and exciton ionisation time τ_{LO-X} (dashed curve).

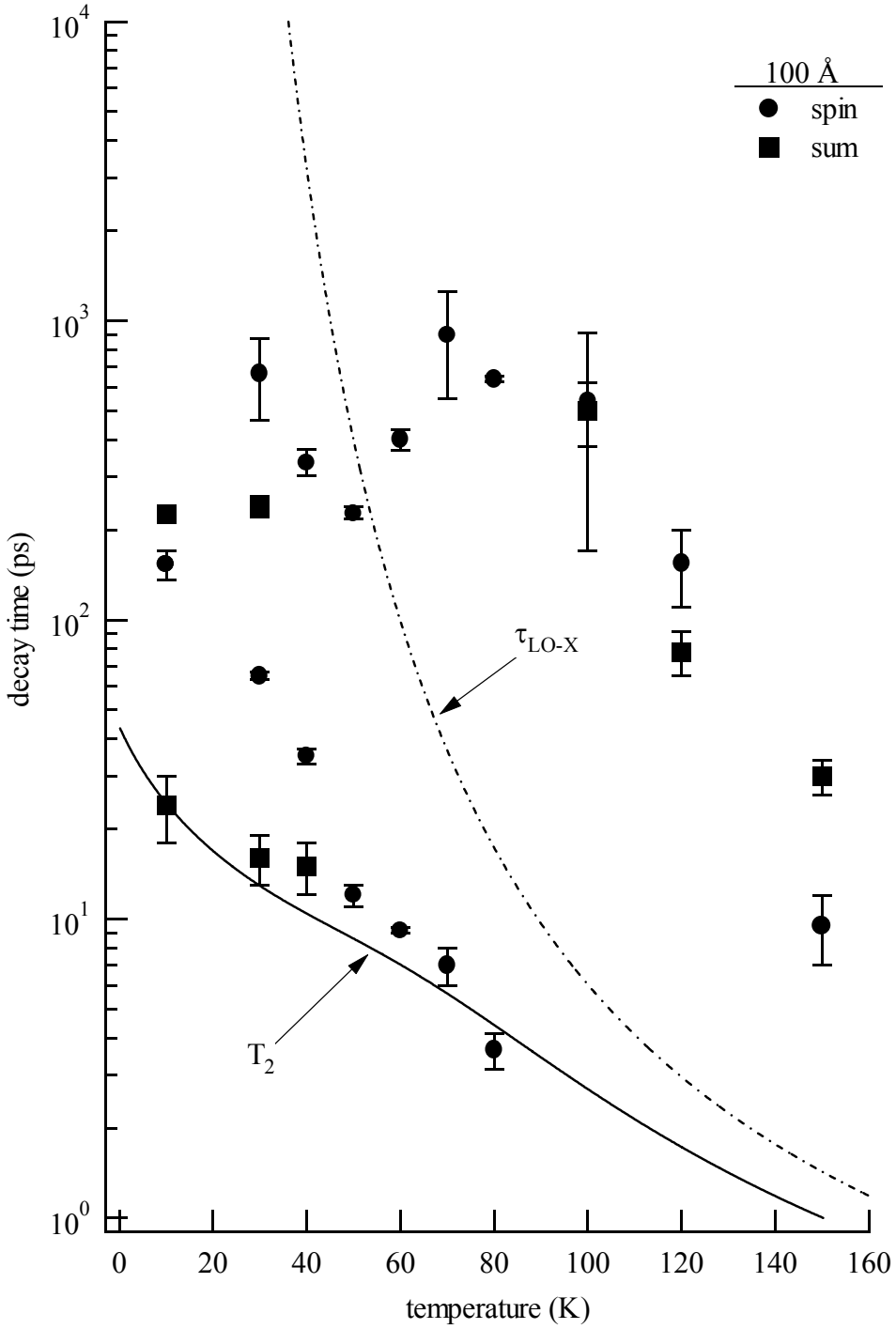

Figure 5.24: Extracted spin (circles) and sum (squares) signal decay times for the 100 Å $InGa_{0.11}/Ga_{0.89}As$ quantum well of sample DB918, also indicated are the estimated exciton dephasing time, T_2 and the exciton ionisation time τ_{LO-X}.

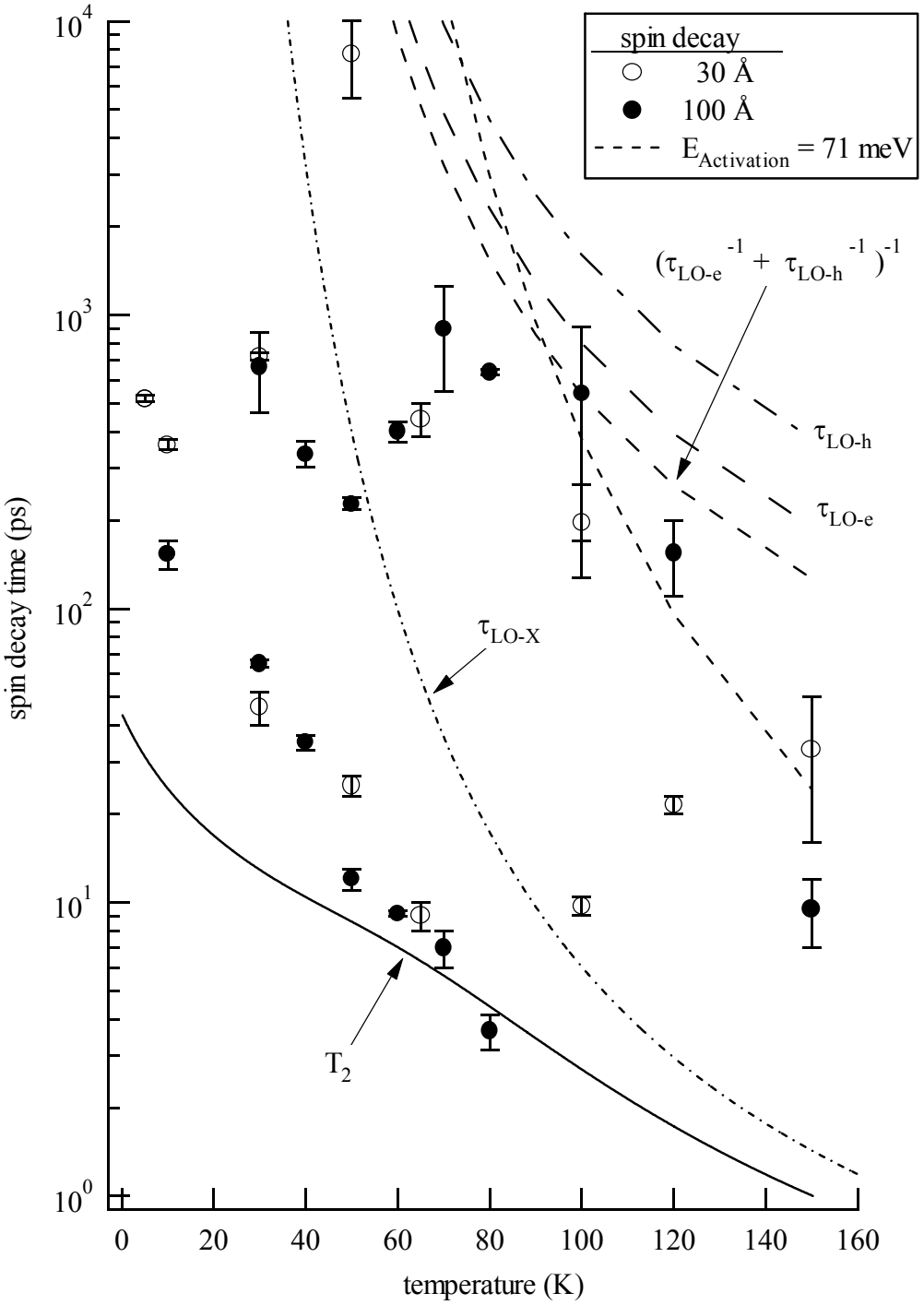

Figure 5.25: Extracted spin signal decay times for the 30 Å (open circles) and 100 Å (closed circles) $InGa_{0.11}/Ga_{0.89}As$ quantum wells of sample DB918, estimated exciton dephasing time (T_2) exciton ionisation time ($\tau_{LO\text{-}X}$), calculated electron-LO phonon ($\tau_{LO\text{-}e}$) and hole-LO phonon ($\tau_{LO\text{-}h}$) scattering time and their combined effect, $(\tau_{LO\text{-}e}^{-1} + \tau_{LO\text{-}h}^{-1})^{-1}$.

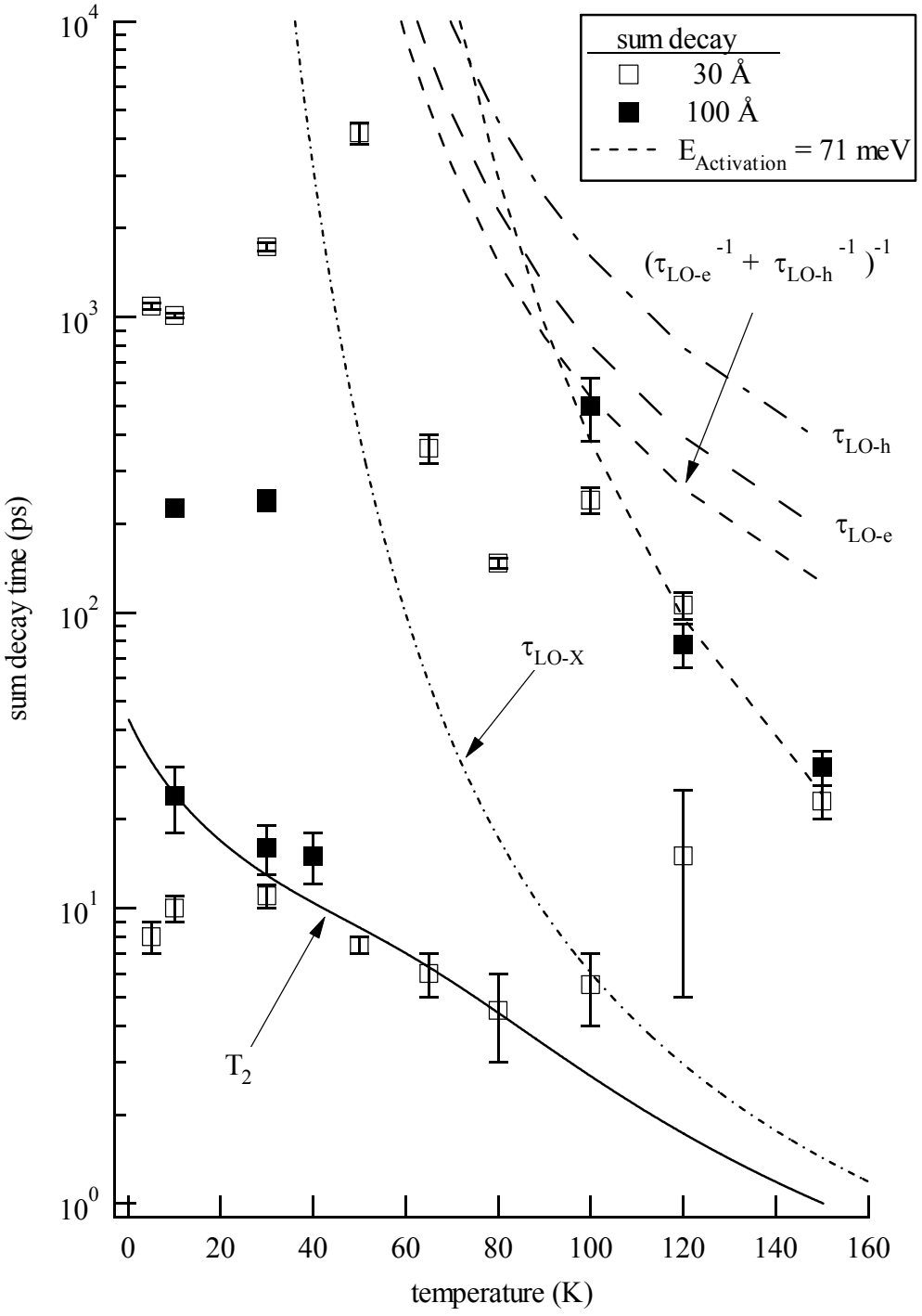

Figure 5.26: Extracted sum signal decay times for the 30 Å (open squares) and 100 Å (closed squares) $InGa_{0.11}/Ga_{0.89}As$ quantum wells of sample DB918, estimated exciton dephasing time (T_2) exciton ionisation time ($\tau_{LO\text{-}X}$), calculated electron-LO phonon ($\tau_{LO\text{-}e}$) and hole-LO phonon ($\tau_{LO\text{-}h}$) scattering time and their combined effect, $(\tau_{LO\text{-}e}^{-1} + \tau_{LO\text{-}h}^{-1})^{-1}$.

5.7 Interpretation

Absorption of the circularly polarised pump pulse resulted in filling of σ^+ (say) optically active states and since light absorption is proportional to the number of available final states, absorption of the σ^+ component of the delayed probe pulse decreased. The measured reflection intensity change (ΔR) was largest while many states within the spectral width of the pulse were occupied. As the non-equilibrium photo excited carriers moved away from this region through recombination or conversion into optically inactive (large k or $J^h_z=\pm 2$ excitons) states, ΔR decreased. Spin imbalance in the filled states modified the optical density and refractive index for the two polarisations, resulting in elliptisation and rotation of the polarisation plane of the linearly polarised probe. It was shown in chapter 3 that rotation of the probe polarisation was registered by the difference signal ($\Delta\theta$), and argued that the measuring system was insensitive to elliptisation. Thus $\Delta\theta$ measured the amount of spin polarisation in the system.

In simple cases of a single particle species possessing two spin states mapping directly onto the opposite circular polarisations, ΔR is proportional to the total number of particles and $\Delta\theta$ to the imbalance of spin state occupation, expressed as:

$$\Delta R \sim N^+ + N^-, \qquad (5.24)$$

$$\Delta\theta \sim N^+ - N^-,$$

where N^+ and N^- are the number of particles in each spin state. The ratio $\Delta\theta/\Delta R$ measures the spin polarisation, S, of the population. With more than one particle species, extracting the spin polarisation and population of each state from the recorded ΔR and $\Delta\theta$ is more complicated. Considering for example the case where excitons, unbound e-h pairs and perhaps other species co-exist, ΔR would be proportional to the total population that couples to light:

$$\Delta R \sim P_x + a_1 P_{e\text{-}h} + \ldots, \qquad (5.25)$$

where P_x, $P_{e\text{-}h}$ are the populations of optically active excitons and unbound e-h pairs with a_1 representing the different strength of effect of e-h pairs compared to excitons. The other terms may arise from the effects of other states, such as having a hole in the barrier and electron in the well. $\Delta\theta$ would be proportional to the imbalance in occupation of states coupling to σ^+ and σ^- photon states:

$$\Delta\theta \sim (N_x^+ - N_x^-) + a_1(N_{e\text{-}h}^+ - N_{e\text{-}h}^-) + \ldots, \qquad (5.26)$$

where $N_{X,(e\text{-}h)}^{\pm}$ is the number of excitons (e-h pairs) that couple to $\sigma^{\pm}$ photons and other terms may also be present. Thus some caution must be taken when assigning the evolution of ΔR and $\Delta\theta$ to the dynamics of individual species. The spin signal, defined by $\Delta\theta/\Delta R$, is in some sense proportion to the spin polarisation of the aggregate population, and ΔR an aggregate measure of the number of photo excited particles.

In summary, at low temperatures where the exciton is stable the long-lived decay component of ΔR probably can be interpreted as the life-time of the exciton, and that of $\Delta\theta/\Delta R$ as the exciton spin-life-time. As the temperature is raised, exciton unbinding and carrier escape are likely to become significant and numerical solution of coupled rate equations may be required, perhaps in conjunction with further experiments, to confirm assignment of the rates obtained from simple fits to the correct physical processes.

5.7.1 Phases in the evolution of the excited population

Time evolution of the photoexcited population can be broken qualitatively into three stages following the resonant excitation. The initial exciton population is cold, it has a spectral shape that is more like an image of the narrow exciting pulse than of a wide thermalised gas at the lattice temperature. During the first phase, scattering with acoustic phonons warms the exciton gas and its spectral distribution widens. Some radiative decay occurs during this phase, which is enhanced because of the high occupation of states within the radiative linewidth. The

boundary to the second phase is roughly delimited by rate of exciton scattering with acoustic phonons.

During the second phase, the thermalised exciton population decays radiatively (it still interacts with the acoustic phonons but by this stage is thermalised) at the non-enhanced radiative decay rate for a thermalised population. If the exciton recombination time is much shorter than $\tau_{LO\text{-}X}$, the exciton-optical phonon scattering time, then unbinding will obviously not occur significantly and the population will only experience the first two phases. Otherwise a third phase may be entered during which there are a significant number of unbound electron-hole pairs which will dominate the measurements at long delays. The unbound electron-hole particles can spin relax, escape from the well through their interaction with optical phonons, or recombine. The long-term equilibrium ratio of excitons to unbound pairs is predicted by the Saha equation (equation 5.7) which takes account of the equilibrium between the ionisation and its reverse process, $\tau_{LO\text{-}X}$ is the average amount of time an exciton remains bound.

In this context figures 5.23 to 5.26 can be interpreted as timeline diagrams showing how the photoexcited population evolves, the abscissa gives the sample temperature and the time following excitation is given by the ordinate. For example, bearing in mind the 2 ps exciting pulse width it is clear that at 100 K (see the curve labelled $\tau_{LO\text{-}X}$ in figure 5.26, described later) the excitons ionise during the pulse duration and, the unbound electron-hole pair are scattered by LO phonons after around 400 ps (given by the curve labelled $\tau_{LO\text{-}e}^{-1}$, also described later).

5.7.2 Exciton thermalisation

At low temperatures and short delays exciton localisation and thermalisation are the relevant processes affecting exciton spin dynamics. Thermalisation occurs at the acoustic phonon scattering rate. The exciton dephasing time (T_2) is related to the homogeneous linewidth (γ) by $T_2=2\hbar/\gamma$ [20], where the exciton line width as can be expressed as:

$$\gamma_0 = \gamma_{00} + A_1 T + A_2/(\exp(\hbar\omega_{LO}/(k_B T)) - 1), \quad (5.27)$$

γ_{00} is a temperature independent contribution and A_1 and A_2 are the coupling strengths of acoustic and optical phonon modes respectively to the exciton. For temperatures above γ_{00}/A_1 (around 10 K) the main contribution to T_2 is from phonon scattering and, since below $\hbar\omega_{LO}/k_B$ LO scattering is negligible, thermalisation occurs on a time scale of $2\hbar/A_1T$ and ΔR ought to have a fast decaying component of this magnitude. Borri et al. [20] measured the parameters γ_{00}, A_1 and A_2 in a set of 5 $In_{0.18}Ga_{0.82}As/GaAs$ quantum wells and found that A_1 increased from ~1.6 to 3.2 μeVK^{-1} and that A_2 varied between 8 and 20 meV over a small increase of well width from 10 to 40 Å. Since their measured variation of the linewidth parameters with well width is weak, the values 2.4 μeVK^{-1} and 19 meV are used here for A_1 and A_2 respectively. Parameter γ_{00} ought to be strongly sample dependant, reflecting scattering due to processes such as alloy disorder, impurity and exciton-exciton scattering. Measurements of it are not available for the sample studied here, but because the linewidth is not strongly influenced at elevated temperatures by reasonable variations of γ_{00}, the value of 30 μeV as found by Borri et al. [20] is used. The dephasing time roughly expected in the present sample as a function of temperature is plotted on figures 5.23 to 5.26, it coincides remarkably well with the fast decay component detected in the sum signal for both wells from 20 to 80 K. Deviations at temperatures below around 20 K may indicate a difference in the amount localisation.

Below ~60 K, the exciton dephasing is dominated by scattering with acoustic phonons, acting to thermalise the excitons to the lattice temperature. Coincidence with the estimated T_2 indicates that the fast decay of the sum can be used as a measure of the exciton thermalisation time, the rate at which the energy distribution of cold exciton population, warming to the lattice temperature, widens. That this fast decay component of the sum is not accompanied by spin

relaxation at a similar rate also indicates that it is most likely due to thermalisation, rather than hole spin flip. Were it the result of the creation of optically inactive states due to the process $|J^{ex}_z=+1> \rightarrow |J^{ex}_z=+2>$ via hole spin flip, then the spin signal would also decay at a similar rate.

5.7.3 Thermalised excitons

The observed slow decay of ΔR at low temperatures on timescales at least 20 times longer than T_2 is a measure of the radiative recombination rate of the thermalised exciton population, τ_r. Its constancy with temperature below 40 K is consistent with the idea of a localised exciton population at low temperatures. Increased itinerancy with temperature leads to the eventual increase of radiative life-time with temperature expected for a smaller occupation of low-k radiative states [13, 11]. τ_r in the 30 Å well is approximately five times longer than that in the 100 Å well at low temperature, the direction of this well width dependence is consistent with measurements by Amand et al. [21] who find exciton lifetimes in strained $In_{0.12}Ga_{0.88}As/GaAs$ wells of ~450 and ~375 ps for widths of 40 and 120 Å respectively. At low temperatures, interface morphology and alloy disorder can influence the radiative life time greatly, making it difficult to compare samples without some characterisation of these parameters.

Spin relaxation is plotted as a function of the estimated dephasing rate T_2 in figure 5.27. There is no distinct well width dependence to the fast component. When the LO scattering is weak but acoustic phonon scattering is strong, around $4 < T_2 < 7$ ps, spin polarisation of the exciton population decays at the scattering rate T_2. The most likely spin relaxation process that occurs at the scattering rate is that of holes at $k>>0$ (see for example reference 4).

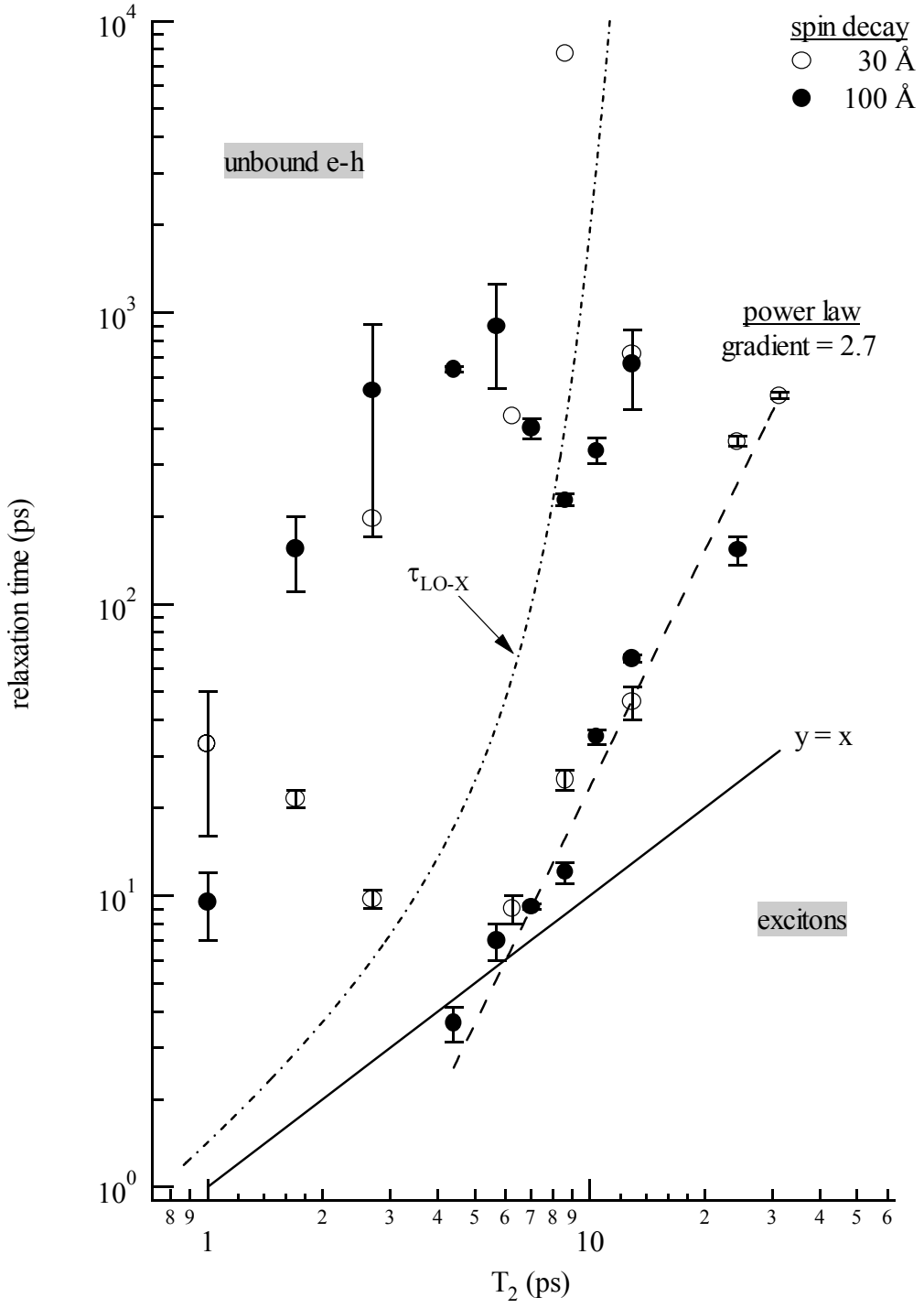

Figure 5.27: Extracted Δθ decay times for the 30 (open circles) and 100 (closed circles) Å wells as a function of the exciton dephasing time T_2. Fast spin decays ($\tau_{\Delta\theta}$) have the power law dependence on T_2 indicated by the dashed line. Frequent exciton scattering coincides with faster spin relaxation.

Where T_2 is long (at low temperatures) the spin life-time is ~10 times longer. This is also expected of holes in a quantum well, since at low temperature only low k states are occupied and lifting of lh-hh degeneracy by confinement implies weak spin relaxation. But, hole-spin flip would result in ΔR signal decay at an equal rate, which is absent in these measurements; therefore it cannot be assigned to hole-spin flip. Exciton spin-flip is expected to be the most important relaxation mechanism at low temperatures and this is indicated by the data.

There appears a clear empirical trend relating the spin relaxation rate to T_2:

$$\tau_{\Delta\theta} = 0.05\ T_2^{2.70\pm0.02}, \qquad (5.28)$$

indicated by a dashed line in figure 5.27. This dependence is opposite to that expected of W_{ex} (see equation 5.4) if it is assumed that the exchange strength does not vary strongly with temperature. However, both the exchange strength (indicated by $\Omega_{\|}$) and the hole spin flip rate (W_h) may be temperature dependent. W_h, driven by momentum scattering (T_2), ought to increase with temperature. Many factors could influence the temperature dependence of $\Omega_{\|}$, particularly the exciton localisation and electron-hole wave function overlap, which reduces due to screening in the presence of a significant unbound e-h population.

The ratio $\Omega_{\|}/W_h$ can be used as a measure of the relative importance of the effects of long-range exchange and hole spin-flip on spin relaxation within the exciton phase; in a weak exchange regime ($\Omega_{\|}/W_h << 1$) the spin polarisation will decay as W_h; for $\Omega_{\|}/W_h >> 1$, spin polarisation is lost at the rate W_{ex}.

That the fast decay of $\Delta\theta$ (at rate $\tau_{\Delta\theta}^{-1}$) was not accompanied by a similar decay of ΔR (at rate $\tau_{\Delta R}^{-1}$) at low temperatures, indicates that this dynamic was due to exciton spin relaxation, $|J^{ex}_z=+1\rangle \rightarrow |J^{ex}_z=-1\rangle$, at rate W_{ex} and that the fast decay component of ΔR was caused by thermalisation: $\tau_{\Delta R} = T_2$. At temperatures where $\tau_{\Delta\theta} \sim T_2$, the two signals do decay at similar

rates. $\tau_{\Delta\theta} \sim T_2$ is therefore interpreted as the process $|J^{ex}_z=+1> \rightarrow |J^{ex}_z=+2>$ caused by hole spin flips at the rate $W_h=T_2$.

From the above considerations it may be possible to use the relation $\tau_{\Delta\theta}^{-1} = \Omega_{\|}^2 T_2$ in conjunction with the fast decaying component of ΔR to obtain the long-range exchange energy as $\hbar(\tau_{\Delta\theta}.\tau_{\Delta R})^{-1/2}$, this is plotted in figure 5.28 as a function of the lattice temperature. Assuming the hole spin-flip occurs at the momentum scattering rate then it may be obtained as $\hbar.\tau_{\Delta R}^{-1}$ (also in figure 5.28).

The observed increase of $\hbar(\tau_{\Delta\theta}.\tau_{\Delta R})^{-1/2}$ with temperature supports the idea that it is a measure of $\Omega_{\|}$, as the exchange strength ought to increase with increased exciton centre-of-mass momentum which is expected at elevated temperatures where the excitons become more itinerant. In addition, exchange is expected to be stronger in the narrower well due to increased wave function overlap. The hole spin-flip is expected to increase with increased valence band mixing induced by finite in-plane momentum associated with increased itinerancy. That $(\hbar/\tau_{\Delta R})^{-1}$ increases with temperature supports its assignment as a measure of W_h. This interpretation, of the measured quantities $\hbar(\tau_{\Delta\theta}.\tau_{\Delta R})^{-1/2}$ and $\hbar/\tau_{\Delta R}$ as $\Omega_{\|}$ and W_h respectively, implies a transition from a weak exchange regime ($W_h > \Omega_{\|}$), at low temperatures, towards a less weak exchange regime ($W_h \approx \Omega_{\|}$) at higher temperatures.

Maialle et al. [3] calculate the long-range exchange energy in GaAs wells as ~35 and 20 μeV for well widths of 30 and 100 Å respectively, an enhancement factor of 1.75, these compare with those measured here of 29.3 and 20.4 μeV (in $In_{0.11}Ga_{0.89}As$) for the 30 and 100 Å wells respectively, an enhancement of 1.45.

Enhanced valence band mixing in the wider well ought to cause a faster hole spin-flip than in the narrow well, the opposite dependence results from the above analysis. Effects other than valance band mixing (e.g. the value of $<k_{hole}^2>^{1/2}$ due to the uncertainty principle in relation to

exciton binding and amount of localisation) could have some influence and might compensate the valence band mixing effect.

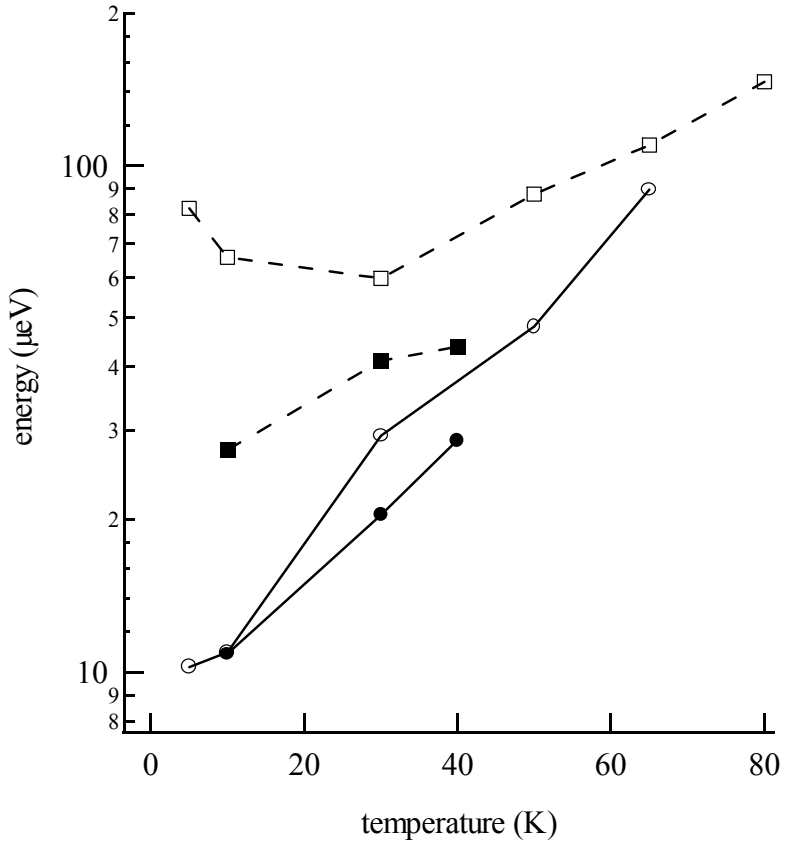

Figure 5.28: Plot of the long-range exchange strength ($\hbar\Omega_{\|}$, circles) and the hole spin-flip energy ($\hbar W_h$, squares) as a function of the lattice temperature in the 30 (open symbols) and 100 (closed symbols) Å wells.

5.7.4 Comparison with InGaAs/InP, the Native Interface Asymmetry

At temperatures between 80 and 100 K the excitons unbind relatively quickly and the spin remaining decays as a tail in the spin signal with life-time τ_e, which we find is several hundreds of picoseconds. This is long on the time-scales of the measurements by Malinowski et al. [1] in InGaAs/InP (see also Marsden [2]) and GaAs/AlGaAs of ~5 and ~50 ps respectively, and indicates that electron spin dynamics in our InGaAs/GaAs wells are qualitatively more similar to those in GaAs/AlGaAs than InGaAs/InP. Thus we conclude that the fast spin relaxation

observed in InGaAs/InP was due to the Native Interface Asymmetry and that electron spin does not relax intrinsically quickly in InGaAs wells. That the electron spin lifetime in InGaAs/GaAs in longer than in GaAs/AlGaAs is most likely due to the increased scattering in the ternary well material.

5.7.5 Dynamics of the unbound e-h plasma and carrier emission

At temperatures above ~100 K the rate $\tau_{LO\text{-}X}^{-1}$ is faster than the scattering due to other processes. LO phonon scattering results in exciton ionisation before significant thermalisation and spin relaxation can occur within the exciton phase.

Analysis of the temperature dependence of the evolution of the plasma of unbound e-h pairs requires knowledge of their interaction with the phonon population, which is weaker than the exciton-phonon interaction. Energy exchange between electrons and holes mediated via Coulomb carrier-carrier scattering is strong enough that the electrons and holes probably share a common temperature, likely different to that of the lattice. Scattering with phonons thermalises the plasma towards the lattice temperature at the plasma-phonon scattering rate. At high enough temperatures the thermalised energy distribution of the plasma in these shallow wells may have a significant tail which is above the activation energy ($E^{h,e}_A$) and some of the carriers may escape from the well into the barrier.

For temperatures above ~ 50 K the LO phonons are the dominant (over acoustic phonons) courier of energy from the lattice to the plasma. Shah [14] discusses the interaction of optical phonons with electrons and holes. In 3D, the characteristic electron-optical phonon scattering rate is given by:

$$\tau^{3D}_{LO}{}^{-1} = (1/\xi_\infty - 1/\xi_0)e^2(2m\hbar\omega_{LO})^{1/2}/(4\pi\hbar^2), \qquad (5.29)$$

where ξ_∞ and ξ_0 are the optical and static dielectric permittivities. In 2D the interaction is modified by a constant:

$$\tau^{2D}{}_{LO}{}^{-1} = (\pi/2)\tau^{3D}{}_{LO}{}^{-1}; \qquad (5.30)$$

the characteristic scattering rate in 2D GaAs is 80 fs (see ref. 14). The actual rate of scattering of the plasma, which includes both phonon emission and absorption, is a function of the carrier energy and to be more accurate a dynamic model of the evolution of the carrier distribution would be required. An estimate can be obtained from the product of the phonon occupation number and the characteristic rate:

$$\tau_{LO\text{-}e}{}^{-1} = 0.080/(\exp(\hbar\omega_{LO}/(K_B T)) - 1)\ (ps^{-1}). \qquad (5.31)$$

The hole-optical phonon interaction is not simply obtained by using the hole effective mass in equation 5.29 because the hole wave functions are p-states, the hole-optical phonon rate is in fact half the value of the electron rate [14]:

$$\tau_{LO\text{-}h}{}^{-1} = \tfrac{1}{2}.\tau_{LO\text{-}e}{}^{-1}. \qquad (5.32)$$

Calculated $\tau_{LO\text{-}h}$ and $\tau_{LO\text{-}e}$ for GaAs wells are plotted in figures 5.25 and 5.26. Energy given to either the electron or hole component should be quickly distributed between both plasma components by the strong carrier-carrier scattering. It is therefore more appropriate to consider the combined rate, $\tau_{LO\text{-}h}{}^{-1} + \tau_{LO\text{-}e}{}^{-1}$, which is also plotted in those figures.

Agreement between the combined scattering rate and the fast decay of the sum at high temperatures is reasonable considering the approximations (for example, the calculated rates are for GaAs and include no knowledge of the initial plasma distribution and its evolution). The suggestion that it is the combined rate that regulates the observed decay is illustrated in figure 5.29 which displays the fast components of the high temperature signals and the calculated separate electron and hole scattering times against their combined scattering time. It is interesting that the spin polarisation decays close to this rate also.

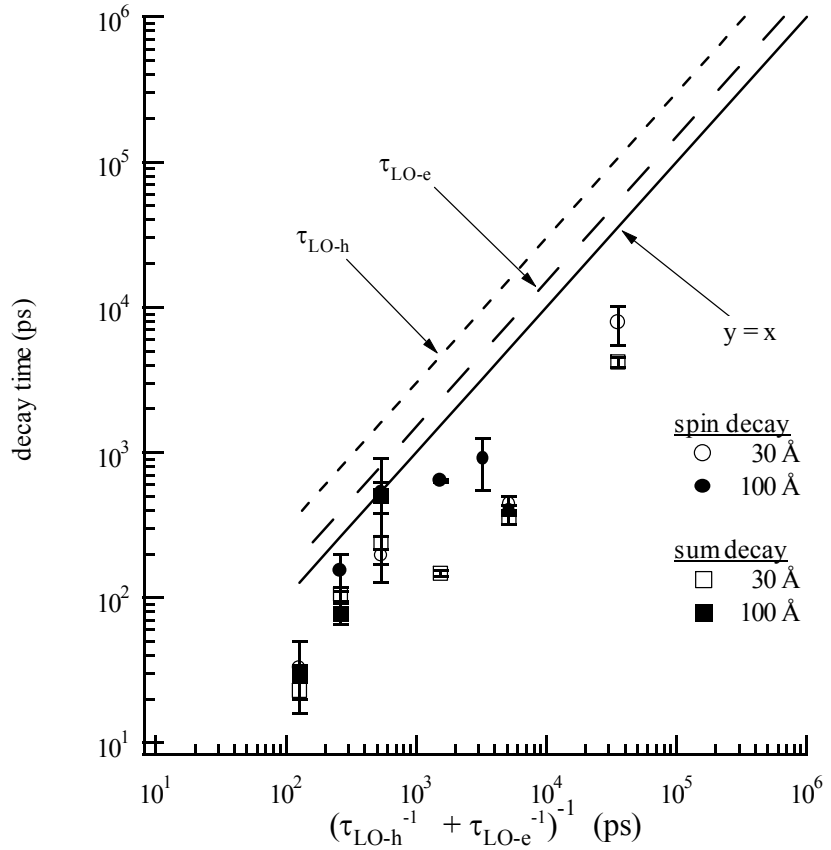

Figure 5.29: Experimental decay times at high temperatures in the unbound e-h phase plotted against the combined electron-phonon and hole-phonon scattering time. Dashed lines are the scattering times for each component and the solid line, y=x, indicates the total plasma-phonon coupling.

At temperatures where the plasma can escape from the well the ΔR signal shows a decay. The temperature of onset of significant ΔR decay is different in the two wells. In the 100 Å well, the onset occurs between ~80 and 100 K (compare figures 5.19 and 5.20) and in the 30 Å well between 50 and 65 K (compare figures 5.7 and 5.8). The temperature difference of the onset in the two wells can be explained by considering that the hole activation energy E^h_A, required to emit it into the barrier, is a decreasing function of well width. Our observed onset temperatures are consistent with the onset of decrease of PL intensity measured by Botha et al.

[17] of ~65 and 100 K in $In_{0.19}Ga_{0.81}As$/GaAs wells of 33 and 100 Å respectively which they argued was due to unipolar escape of the hole.

In the context of the above discussion, the tail of the energy distribution of the holes must stretch to a higher energy in the wider well for any carrier to escape the quantum well layer, quantum confinement pushes the hole closer to the lip of the potential well in the narrow well – giving it a head-start. Electron and hole effective masses in $In_xGa_{1-x}As$ quantum well material are given empirically by [22]:

$$m_e^* = 0.029 - 0.06x, \text{ and} \qquad (5.33)$$

$$m_{h,z}^* = 0.34 + 0.01x,$$

and in bulk $Al_yGa_{1-y}As$ as:

$$m_e^* = 0.067 + 0.083y, \text{ and} \qquad (5.34)$$

$$m_{h,z}^* = 0.34 + 0.42y.$$

The n=1 electron and heavy-hole confinement energies are calculated using the transcendental function (equation 2.7) with values for the effective masses calculated by setting x=0.11 and y=0 in equations 5.33 and 5.34. Values so obtained are 113 and 20 meV respectively in the 30 Å quantum well, and 42 and 5.4 meV in the 100 Å well for the electron and heavy-hole confinement respectively. A formula for the band gap of the $In_xGa_{1-x}As$ ternary alloy [23] is:

$$E_g^{GaAs} + x.(E_g^{InAs} - E_g^{GaAs}) - 0.84x.(1-x), \qquad (5.35)$$

where E_g^{GaAs} and E_g^{InAs} are the band gaps of GaAs and InAs with values of 1.519 and 0.418 eV respectively. Thus the band gap of $In_{0.11}Ga_{0.89}As$ is approximately 1.316 eV. Using this value in equation 5.8 with a value of 0.83 for Q [17], conduction and valence band depths are calculated as 169 and 34.5 meV respectively. The calculated electron and hole activation

energies, (equation 5.10) are 56 and 15 meV respectively in the 30 Å and 127 and 29 meV respectively in the 100 Å well.

These hole activation energies are less than the LO phonon energy and it might be expected that the holes ought to escape from the wells during the ionisation process. However, the exciton binding energy must also be supplied and may be why the holes are not emitted by the exciton-optical phonon scattering.

It is reasonable to expect that the rate of carrier escape is proportional to the number of electrons at the escape energy:

$$\tau_{escape} \sim \exp(E_{activation}/(k_B T)). \qquad (5.36)$$

The short dashed line in figures 5.25 and 5.26 is a function of this form with activation energy of 71 meV, it does follow the sum decay times in the 30 Å well at high temperature (>100 K). This activation energy is equal to the sum of the calculated electron and hole activation energies $E^e_A+E^h_A$ for the 30 Å well, suggesting that bipolar emission may occur at temperatures above ~100 K in the 30 Å well. No reasonable instance of the form 5.36 was found which matches the high temperature carrier escape rates in the 100 Å well involving any sensible combinations of the activation energies calculated for that well width.

5.8 Summary and conclusions

The work of this chapter was designed to investigate why the electron spin relaxation in InGaAs/InP is much faster than in GaAs/AlGaAs as measured by Malinowski et al. [1] and Marsden [2]. Two possible reasons are: 1) it has native interface asymmetry whilst the latter does not, or 2) InGaAs wells may have some qualitative differences to GaAs wells.

By studying the electron spin relaxation in InGaAs/GaAs we have distinguished between the two. InGaAs/GaAs does not have the native interface asymmetry but does have InGaAs wells. Since the relaxation was slower than in both GaAs/AlGaAs and InGaAs/InP we

conclude that it is the native interface asymmetry in InGaAs/InP that causes the observed fast electron spin relaxation. It was slower than in GaAs/AlGaAs due to the increased electron scattering (re. the D'Yakonov-Perel mechanism, chapter 4) by alloy disorder that is inherent to ternary compound wells.

At low temperatures the spin decayed as a single exponential whose rate of decay increased with temperature and eventually equalled the exciton dephasing rate. Measurement of ΔR allowed distinction between the process of hole-spin flip and exciton spin-flip. Hole spin-flip at the exciton scattering rate was observed at high temperature and exciton spin-flip prevailed at low temperature. A smooth transition between the two was observed and we obtained the long-range exchange strength and hole spin-flip energy from measurements of both ΔR and $\Delta\theta$.

Complications arose due to the shallow nature of the 11% Indium content quantum wells which led to thermal emission of carriers into the barrier region at high temperatures. Some calculations were presented that implicate this as the cause of decay of the ΔR signal at high temperatures.

5.9 References

1. **"Exciton vs free-carrier spin-relaxation in III-V quantum wells"**, A. Malinowski, P. A. Marsden, R. S. Britton, K. Puech, A. C. Tropper and R. T. Harley, *Proc. 25th Int. Conf. Phys. Semicond., Osaka, Part **1** 631 (2001).*

2. "Investigation of narrow-band semiconductor quantum well structures using a synchronously-pumped optical parametric oscillator", P. A. Marsden, *Ph.D. thesis, University Of Southampton (2001).*

3. **"Exciton spin dynamics in quantum wells"**, M. Z. Maialle, E. A. de Andrada e Silva and L. J. Sham, *Phys. Rev., B, **47** 15776 (1993).*

4. **"spin-flip scattering of holes in semiconductor quantum wells"**, R. Ferreia and G. Bastard, *Phys. Rev., B, **43** 9687 (1991).*

5. **"Optical nonlinearities and instabilities in semiconductors"**, edited by H. Haug, *Academic Press (1988).*

6. **"Magnetic-field dependence of exciton spin relaxation in GaAs/$Al_xGa_{1-x}As$ quantum wells"**, R. T. Harley and M. J. Snelling, *Phys. Rev, B, **50** 9561 (1996).*

7. **"Exciton dynamics in GaAs quantum wells under resonant excitation"**, A. Vinattieri, Jagdeep Shah, T. C. Damen, D. S. Kim, L. N. Pfeiffer, M. Z. Maialle and L. J. Sham, *Phys. Rev, B, **50** 10868 (1994).*

8. **"Localized and delocalized two-dimensional excitons in GaAs-AlGaAs multiple-quantum-well structures"**, J. Hegarty, L. Goldner and M. D. Sturge, *Phys. Rev. B. **30** 7346 (1984).*

9. “Resonant Rayleigh scattering by excitonic states laterally confined in the interface roughness of GaAs/$Al_xGa_{1-x}As$ single quantum wells”, N. Garro, L. Pugh, R. T. Phillips, V. Drouot, M. Y. Simmons, B. Kardynal and D. A. Ritchie, *Phys. Rev. B. 55 13752 (1997).*

10. **“Competition between radiative decay and energy relaxation of carriers in disordered In_xGa_{1-x}/GaAs quantum wells”**, M. Grassi Alessi, F. Fragano, A. Patanè, M. Capizzi, E. Runge and R. Zimmermann, *Phys. Rev. B. **61** 10985 (2000).*

11. **“Two-dimensional exciton dynamics in InGaAs/GaAs quantum wells”**, Y. Takahashi, S. Owa, S. S. Kano, K. Muraki, S. Fukatsu, Y. Shiraki and R. Ito, *Appl. Phys. Lett., **60** 213 (1992).*

12. **“Subpicosecond spin relaxation dynamics of excitons and free carriers in GaAs quantum wells”**, T. C. Damen, L. Viña, J. E. Cunningham, J. Shah and L. J. Sham, *Phys. Rev. Lett. 67 3432 (1991).*

13. **“Linewidth dependence of radiative exciton lifetimes in quantum wells”**, J. Feldmann, G. Peter, E. O. Göbel, P. Dawson, K. Moore, C. Foxon and R. J. Elliot, *Phys. Rev. Lett. **59** 2337 (1987).*

14. **“Ultrafast spectroscopy of semiconductors and nanostructures”**, J. Shah, *Springer, (1998).*

15. **“Nuclear Effects in Ultrafast Quantum-Well Spin-Dynamics”**, A. Malinowski, M. A. Brand and R. T. Harley, *Physica E **10**, 13 (2001).*

16. “**Room-Temperature Excitonic nonlinear absorption and refraction in GaAs/AlGaAs multiple quantum well structures”**, D. S. Chemla, D. A. B. Miller, P. W. Smith, A. C Gossard, and W. Wiegmann., *IEEE J. Quantum Electron. **20** 265-275 (1984).*

17. **“Thermally activated carrier escape mechanisms from In_xGa_{1-x}/GaAs quantum wells”**, J. R. Botha, and A. W. R. Leitch, *Phys. Rev. B **50** 18147 (1994).*

18. **"Magneto-Optics Of Excitons In Quantum Wells"**, N. J. Traynor, *Ph.D. Thesis, University Of Southampton (1996).*

19.**"Spin Polarised Dynamics In Quantum Wells"**, E. Blackwood, *Ph.D. thesis, University Of Southampton (1993).*

20. **"Well-width dependence of exciton-phonon scattering in InGaAs/GaAs single quantum wells"**, P. Borri, W. Langbein, J. M. Hvam and F. Martelli, *Phys. Rev. B **59** 2215 (1999).*

21. **"Well-width dependence of the excitonic lifetime in strained III-V quantum wells"**, Th. Amand, X. Marie, B. Dareys, J. Barrau, M. Brousseau, D. J. Dunstan, J. Y. Emery, and L. Goldstein, *J. Appl. Phys. **72** 2077 (1992).*

22. **"Exchange interaction of excitons in GaAs heterostructures"**, E. Blackwood, M. J. Snelling, R. T. Harley, S. R. Andrews and C. T. B. Foxon, *Phys. Rev. B **50** 14246 (1994).*

23. "Survey of semiconductor physics: electrons and other particles in bulk semiconductors", K. W. Böer, *Van Nostrand Reinhold (1990).*

6. Exciton spin precession in a magnetic field

6.1 Introduction

In this chapter the evolution of exciton spin in a 60 period 25.7 Å GaAs/AlGaAs multiple quantum well sample is studied with a magnetic field applied at various angles to the coincident growth and excitation direction. The magnetic field admixes the optically active with the optically inactive exciton spin states and thereby enables direct observation of the latter.

Previous continuous-wave measurements on our sample [1] have revealed that some of the excitons exist in an environment of less than D_{2d} symmetry. In addition to observing the optically inactive states, we investigate whether the effects of lower symmetry, such as spin-splitting of the optically active exciton spin states in absence of an applied magnetic field [2], are observable in time-resolved optical spectroscopy.

We employ the method of *reflectively probed optically-induced transient linear birefringence* pioneered at Southampton by Worsley et al. [3]. This involves excitation with linearly polarised light pulses to create a coherent linear superposition of the heavy-hole exciton spin states. The probe is linearly polarised at 45^{o} to the polarisation axis of the pump and its rotation is induced by the transient linear polarisation axis in the plane of the well left by the pump. The axis rotates in a magnetic field at the frequencies of the exciton spin-splittings, producing quantum beats in the time resolved signal. The frequencies of the beats are used to obtain values for the electron and hole g-factors and the anisotropic short-range exchange interaction.

6.2 Background and theory

g-factors and exchange splittings are important parameters in theoretical models of the band structure, spin relaxation, and coherence properties in semiconductor heterostructures. Van kesteren et al. [2] measured these parameters in type II GaAs/AlGaAs quantum wells of various widths using optically detected electron spin resonance (ODMR) and the simplified Hamiltonian:

$$H_{ex} = \sum_{i=x,y,z} [\mu_B(g_{e,i}S_i + g_{h,i}\Sigma_i)B_i - 2\Delta_i S_i \Sigma_i] \qquad (6.1)$$

to explain their results. Here, $g_{e(h),i}$ are components of the electron (hole) g-factor, S_i is the electron spin operator, Σ_i are components of the effective hole angular momentum operator with values ±1/2 corresponding to hole angular momentum $J^h_z = \pm 3/2$, B_i are magnetic field components and Δ_i are components of the short-range exchange interaction. The first term is the sum of Zeeman interactions of the electron and hole, and the second represents the electron-hole exchange interaction. Coordinate axes are oriented with unit vectors **x** along [110], **y** along [1$\underline{1}$0] in the plane of the well, and **z** along the growth direction [001]. The (arbitrary) basis in which to evaluate the Hamiltonian consists of the electron and hole spins projected along the z-direction. The basis is labelled by the total angular momentum of the exciton (J^{ex}_z) along the z-direction:

S_z	Σ_z	J^{ex}_z
+1/2	+1/2	+2
+1/2	-1/2	+1
-1/2	+1/2	-1
-1/2	-1/2	-2

(6.2)

The usual convention, that the $J^{ex}_z=\pm1$ exciton states couple directly to $\sigma\pm$ polarised light and are thus termed optically active pure circular polarised exciton states, and the $J^{ex}_z=\pm2$ states do not couple directly to light and are termed optically inactive, applies.

Considering a field in the z-x plane, the Hamiltonian evaluates as:

	|+2>	|+1>	|-1>	|-2>
|+2>	$-\mu_B B_z(g^e_z+g^h_z)+\Delta_z$	0	$-\mu_B B_x g^e_x$	$\Delta_x-\Delta_y$
|+1>	0	$-\mu_B B_z(g^e_z-g^h_z)-\Delta_z$	$\Delta_x+\Delta_y$	$-\mu_B B_x g^e_x$
|-1>	$-\mu_B B_x g^e_x$	$\Delta_x+\Delta_y$	$\mu_B B_z(g^e_z-g^h_z)+\Delta_z$	0
|-2>	$\Delta_x-\Delta_y$	$-\mu_B B_x g^e_x$	0	$\mu_B B_z(g^e_z+g^h_z)+\Delta_z$

(6.3)

The form of the eigenstates depends on the applied field and the anisotropy in the exchange interaction, determined by the symmetry of the quantum well. This is a function of the structure of the interface between the well and barrier, set through growth conditions and interface bonding. The simplest symmetry of an (001) oriented quantum well is labelled D_{2d} under which $\Delta_x = -\Delta_y$; under lower symmetry, $\Delta_x \neq -\Delta_y$. In absence of a magnetic field and with D_{2d} symmetry, the eigenstates consist of the degenerate pure $J^{ex}_z=\pm1$ doublet, |+1> and |-1>; and a mixed $J^{ex}_z=\pm2$ doublet, |+2>+|-2> and |+2>-|+2>. Under lower symmetry, the $J^{ex}_z=\pm1$ states become mixed and lose degeneracy. The centres of the two doublets are always separated by energy Δ_z. The inactive mixture states are split by energy $\Delta_x-\Delta_y$ and the active by $\Delta_x+\Delta_y$. Numerically calculated eigen energy solutions as a function of field for both types of symmetry, with magnetic field angles of 0, 45 and 90^o to the z-direction are plotted in Figure 6.1; values of the exchange parameters have been exaggerated to illustrate their effect more clearly.

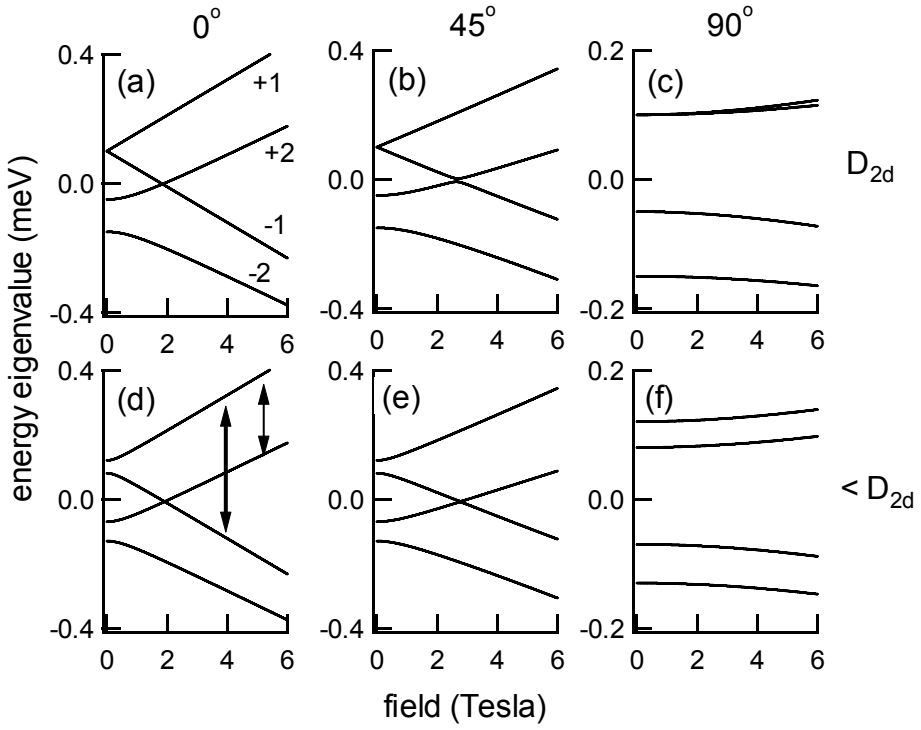

Figure 6.1: Numerically computed energy eigenvalue solutions of the exciton spin Hamiltonian (basis 6.2) with D_{2d} (a, b and c) and lower (d, e, and f) symmetry, for magnetic field applied at angles 0^o (a and d), 45^o (b and e) and 90^o (c and f) to z (the axis of excitation and growth). In (a) the zero-field values of J^{ex}_z are indicated for each state and arrows indicate the beat frequencies observed. Parameter values for this model system are 0.36, 0.17 and –1.74 for g^e_x, g^e_z and g^h_z respectively; for D_{2d} symmetry Δ_x, Δ_y and Δ_z are –50, 50 and 200 μeV, and for lower symmetry 50, -10 and 200 μeV.

Magnetic field components along the z-direction act to diagonalise the Hamiltonian in the basis 6.2 and the optically active eigenstates transform from linear towards pure circular polarisations with increasing field strength whilst the inactive states un-mix. Transverse field

components (along the x- or y-directions) mix the inactive with the active base states and all four eigen states become increasingly optically active with increasing field strength [4].

Van Kesteren et. al [2] obtained good agreement between their measured spin-splittings and the above theory only with $\Delta_x \neq -\Delta_y$ and thus concluded that the excitons in their sample could be divided into two linearly polarised states with principle axis along the x- and y-direction.

ODMR cannot be applied successfully in type-I quantum wells due to the short exciton lifetime. The work of this chapter aims firstly to investigate whether these low symmetry effects can be revealed by quantum-beats in time resolved optical measurements in a type-I quantum well and also continues a general theme of the Southampton group of measuring g-factor and exchange parameters with increasing precision in III-V quantum wells which is reviewed below.

In 1991, Hanle effect measurements were used by Snelling and Flinn et al. [5] to obtain both the sign and magnitude of the electron g-factor in GaAs/AlGaAs wells as a function of well width, revealing that it is positive in narrow wells and passes through zero at ~55 Å. In 1992 Snelling and Blackwood et al. [6] obtained the exciton g-factor by measuring the Zeeman splitting between the two opposite circularly polarised components in the photoluminescence of the heavy-hole exciton as a function of the magnetic field applied along the excitation (growth) direction. In 1994 Blackwood and Snelling et al. [1] studied the circular polarisation of the heavy-hole exciton luminescence as a function of applied magnetic field along the growth axis for both resonant and non-resonant continuous-wave circularly polarised excitation. From level-crossing signals they measured the z-component of exchange ranging from 75 to ~150 μeV in wells of different widths, with uncertainty of ~60%. They also found that up to 20 % of the excitons were in an environment of less than D_{2d} symmetry in a series of type-I GaAs/AlGaAs quantum well samples, including that studied in this chapter. Traynor et

al. (1995) [7] investigated Zeeman splittings of heavy-hole exciton luminescence in InGaAs/GaAs wells to obtain values for the exciton g-factor as a function of well width and indium concentration. Further polarised exciton luminescence measurements are described in references 8 and 9. In 1996 Worsley et al. [3, 10] devised the basic idea of the experimental technique used in this work, of utilising linearly polarised pump pulses set at 45^{o} to the probe to distinguish only the coherent part of the transient exciton population. Here, the measured signal strength (the rotation of the probe) decays at the exciton dephasing rate rather than the rate of recombination. A benefit of the time-resolved measurement method is the ease and precision with which frequencies can be extracted from the data. In 2000, Malinowski and Harley [11], through application of a magnetic field at 45^{o} to the growth direction in a GaAs/AlGaAs quantum well, measured the anisotropy of the electron g-factor using essentially the same time-resolved experiment used for the measurements presented in this thesis with circular pump.

The conditions to observe quantum beats determined by the exchange interaction and therefore the exciton g-factor, as opposed to the electron g-factor, are discussed by Amand et al. [12] and Dyakonov et al. [13], where they conclude that: *"When excitons are generated resonantly by the laser pulse the luminescence oscillations are of excitonic or electronic kind according to whether* $1/\tau < \delta/\hbar$ *or* $1/\tau > \delta/\hbar$*, respectively."* (here, τ is the hole spin-flip time and δ is the exchange interaction strength) and, *"Finally the main factors which contribute to the stabilization of the hole spin orientation within an exciton are the following: the increase of the electron-hole spin correlation via the increase of the exchange interaction related with the confinement and the corresponding decrease of the valence band mixing; the decrease of the exciton temperature"*.

Theoretical description of the interaction of a delayed linearly polarised probe pulse with the transient exciton polarisation induced by excitation with a linearly polarised pump pulse has been given by Östreich et. al [14]. They show that it is the exciton-exciton correlation alone that causes a net rotation of the probe and that the strength of this term oscillates with the frequency of the exciton Zeeman splitting and decays at the exciton dephasing rate. With magnetic field along the growth direction, the J^{ex}_z=+1 or –1 states are Zeeman split by the energy:

$$\Delta E_z = |2\mu_B(g_e+g_h)B|, \qquad (6.\mathbf{1})$$

and excitation with linearly polarised pump creates, a superposition of the two states which imposes a linear polarisation axis (a birefringent axis) in the plane of the quantum well which rotates at the Zeeman splitting frequency, $\Delta E_z/\hbar$. Rotation of the probe is due to the macroscopic linear polarisation in the sample plane imposed by the linearly polarised exciton population, and its magnitude disappears at the coherence decay rate due to any dephasing processes such as momentum scattering, spin relaxation, and recombination [3].

Excitation with circularly polarised pump would populate one of the J^{ex}_z=+1 or –1 exciton states exclusively. In which case the probe rotation would be due to the population difference of the two states, and any beating in a magnetic field along the growth direction would be due to Larmor precession of the spin population between the two states rather than the coherent polarisation vector. Such a signal decays due to spin and population relaxation which can be functions of the dephasing time but are usually much longer.

Solution of the exciton spin Hamiltonian (equation 6.**1**) for magnetic fields applied at angles away from the sample normal shows that, in general, the eigenstates are admixtures of all four exciton spin states. A Fourier limited laser pulse of duration Δt has an energy width of ~$h/\Delta t$; pulses from the Ti:Sapphire laser system have temporal width ~2 ps, corresponding to an

energy width of ~2 meV. Since the largest energy difference expected between any of the exciton spin states is expected to be less than ~1 meV, the laser pulses in our experiments flood all four spin states with light, exciting them coherently. The superposition generated ought to consist predominantly of $J^{ex}_z=\pm1$ excitons since they couple to light strongly.

6.3 Sample description

The sample under study (G50) was chosen because previous measurements [1] have indicated that the excitons in it can be in an environment of lower symmetry, and because quantum beats at the frequency determined by the exciton g-factor are observable at low temperature. The calculated exchange enhancement due to quantum confinement [1] increases with decreasing well width and has a maximum at around 20 Å with an enhancement over the bulk value of a factor of ~4; the exchange strength is relatively weak in wide GaAs/AlGaAs wells (Lz > 100 Å). Reduction of well width below ~20 Å causes wave function leakage into the barriers and the exchange strength decreases to towards the bulk value for the barrier material.

Sample G50 is a 60 period 25.7 Å multiple quantum well sample with photoluminescence (PL) width, PL excitation width, PL excitation energy and Stokes shift of 7.0, 13, 1735, and 6.0 meV respectively [15, 10] measured at 1.8 K. It is composed of a GaAs substrate, a 2500 Å GaAs buffer, a 1040 Å $Al_{0.36}Ga_{0.64}As$ layer, the 25.7 Å quantum well layers separated by 136 Å $Al_{0.36}Ga_{0.64}As$ barriers and a 1040 Å $Al_{0.36}Ga_{0.64}As$ capping layer.

The exchange strength in our sample is expected to be relatively strong due to the width of the wells and correlated electron-hole spin coherent dynamics should prevail at low temperature; the Stokes shift indicates strong exciton localisation increasing the significance of in-plane anisotropy.

6.4 Experiment

Results were obtained using the apparatus described in chapter 3 except that the sample was attached to a sample holder (figure 6.2) specially designed by Malinowski and Harley [11] which allowed application of a magnetic field at any angle to the quantum well whilst ensuring that excitation was close to normal incidence. The pump beam was linearly polarised with electric field oscillating at 45^{o} (direction $\underline{\mathbf{x}}+\underline{\mathbf{y}}$) to that of the linearly polarised probe (direction $\underline{\mathbf{x}}$) illustrated in figure 6.3, and excited a density of $\sim 10^{10}$ cm^{-2} excitons in the well. The probe intensity was of the order of 10 times weaker than the pump.

The sample, held in the VTI magnet cryostat, was cooled to 10 K in Helium vapour. Photo excitation energy was tuned to the n=1 heavy-hole exciton absorption peak, which corresponded to the strongest time-resolved optical response. Time-resolved probe rotation was measured for magnetic field strengths from 0 to 6 T applied at angles of 8, 19, 43, 74 and 87^{o} to the growth axis.

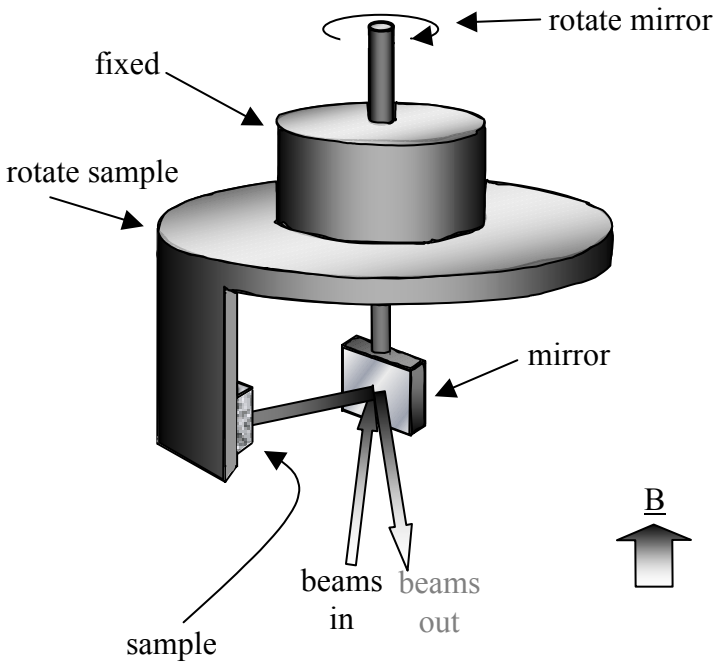

Figure 6.2: Novel sample stick arrangement used to apply a magnetic field at oblique angles to the quantum well normal whilst ensuring near normal incidence of the beams on the sample.

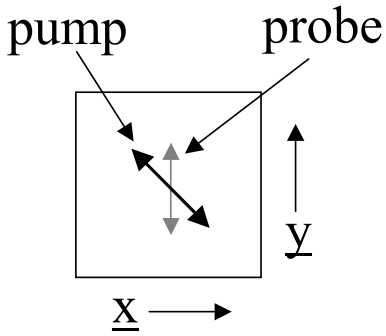

Figure 6.3: The electric field components of the linearly polarised pump and probe oscillate at a relative angle of 45^{o} as illustrated by the heavy and light shaded double headed arrows respectively. Vectors $\underline{x}$ and $\underline{y}$ indicate the unit vectors [110] and [1$\underline{1}$0] in the plane of the quantum well.

6.5 Results

For small angles between the magnetic field and growth axis, the signals (figures 6.4 to 6.9) consisted of a decaying single component oscillation. At larger angles and higher field strengths an additional frequency was observed.

The values of the frequency components reported in this thesis were obtained by the fitting the data with the function:

$$f(t) = A.(1 + B + C),$$

where:

$$A = a_1\exp(-[t-t_0]/\tau_1).[\tanh([t-t_0]/\tau_2) + 1], \qquad (6.2)$$

$$B = a_2\exp(-[t-t_0]/\tau_3).(\cos[\omega_1[t-t_0] + \varphi_1]), \text{ and}$$

$$C = a_3\exp(-[t-t_0]/\tau_4).(\cos[\omega_2[t-t_0] + \varphi_2]).$$

This is an eleven parameter fit; the parameters ω_1 and ω_2 obtained do coincide within error to those we obtained previously [16] using the less involved formula:

$$f(t) = a_0 + \exp(-t/\tau).(a_1\cos[\omega_1 t + \varphi_1) + a_2\cos[\omega_2 t + \varphi_2]) \qquad (6.3)$$

A fit function with a greater number of parameters has been used here to obtain a tighter fit to the data points. Values of the other parameters (a_1, a_2, a_3, τ_1, τ_2, τ_3, τ_4, φ_1, and φ_2) have not been investigated extensively but are reasonable. Values of ω_1 and ω_2 are plotted in figures 6.10 to 6.14, one figure for each of the field angles (8, 19, 43, 74 and 87^o) that were investigated.

The electron and hole g-factors were found using a 3 dimensional fitting procedure to be $g^e_{x,y}$=0.36±0.02, g^e_z=0.17±0.02, g^h_z=-1.74±0.01 and the exchange splittings were c_z=116±4 μeV, c_z+c_y=113±10 μeV and $|c_x+c_y|$=30±8 μeV [16, 17]. Using these parameter values, the eigen values of the Hamiltonian (equation 6.1) have been calculated numerically for each angle of applied magnetic field. Their differences are plotted in figures 6.10 to 6.14.

With the field angle set to 8^o (figure 6.10) the in-plane field component is small and no mixing between the $J^{ex}_z=\pm1$ and ±2 states is expected. A single component oscillation at the frequency of the splitting between the optically active states, at the exciton Zeeman splitting energy, observed. The finite value of the splitting measured as the field strength approaches zero indicates that the exchange interaction strength is anisotropic in the quantum well plane, $|\Delta_x+\Delta_y| > 0$, and symmetry is less than D_{2d}. With the field angle set to 19^o (figure 6.11) the beat between the $J^{ex}_z=\pm1$ is strong. When the field strength is above 3 Tesla a second beat appears at the energy of the splitting between the $J^{ex}_z=-1$ and $J^{ex}_z=-2$ states. At an angle of 43^o (figure 6.12) the beat between the optically active states is strong and again a second beat between the $J^{ex}_z=-1$ and $J^{ex}_z=-2$ states appears at field strengths above 3 Telsa. At an angle of 74^o (figure 6.13) it is less easy to attribute the beats to a particular splitting. It is expected that the strong beat which persists at all fields is between the optically active states. Finally, at 87^o where the magnetic field is mainly in the plane of the well a strong beat between the $J^{ex}_z=\pm1$ states is observed, at field strengths above 3 Tesla a second beat appears. Its energy indicates that it is between either $J^{ex}_z=+1$ and +2 or $J^{ex}_z=-1$ and –2, or both.

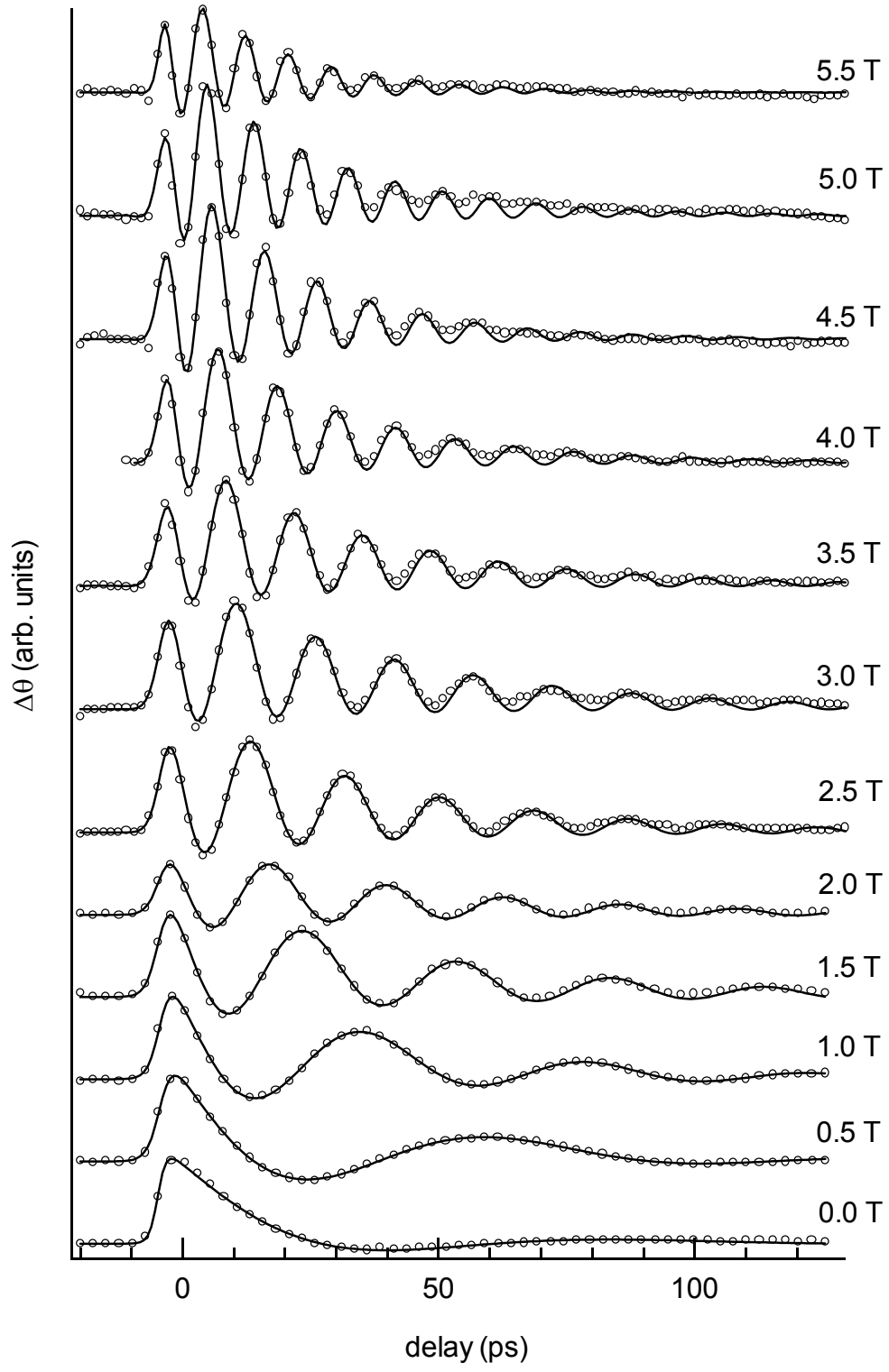

Figure 6.4: Time resolved probe rotation induced by the coherent exciton population in a magnetic applied at 8^{o} to the sample normal with field strengths from 0 to 5.5 T as indicated.

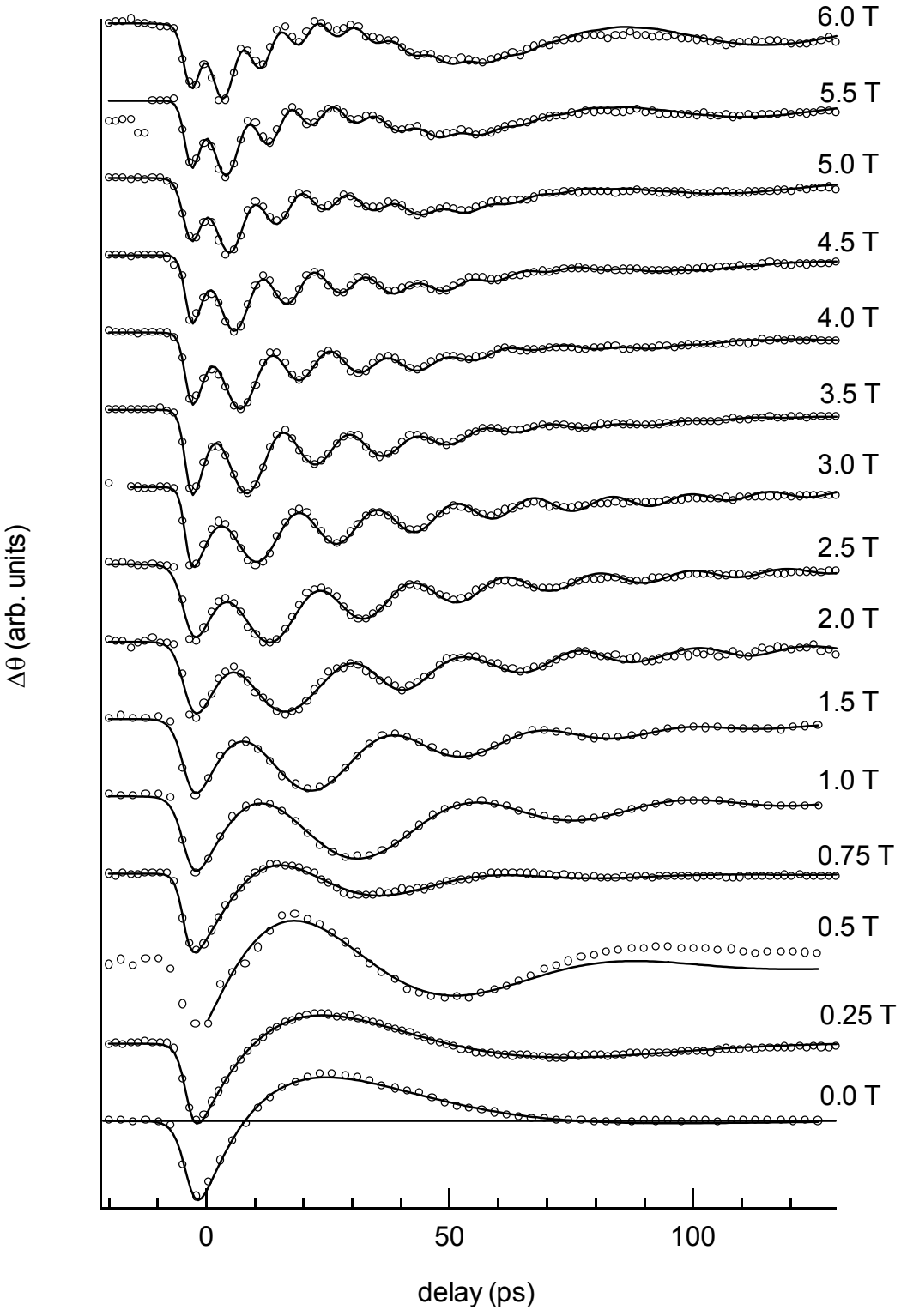

Figure 6.5: Time resolved probe rotation induced by the coherent exciton population in a magnetic applied at 19^{o} to the sample normal, with field strengths from 0 to 6 T as indicated.

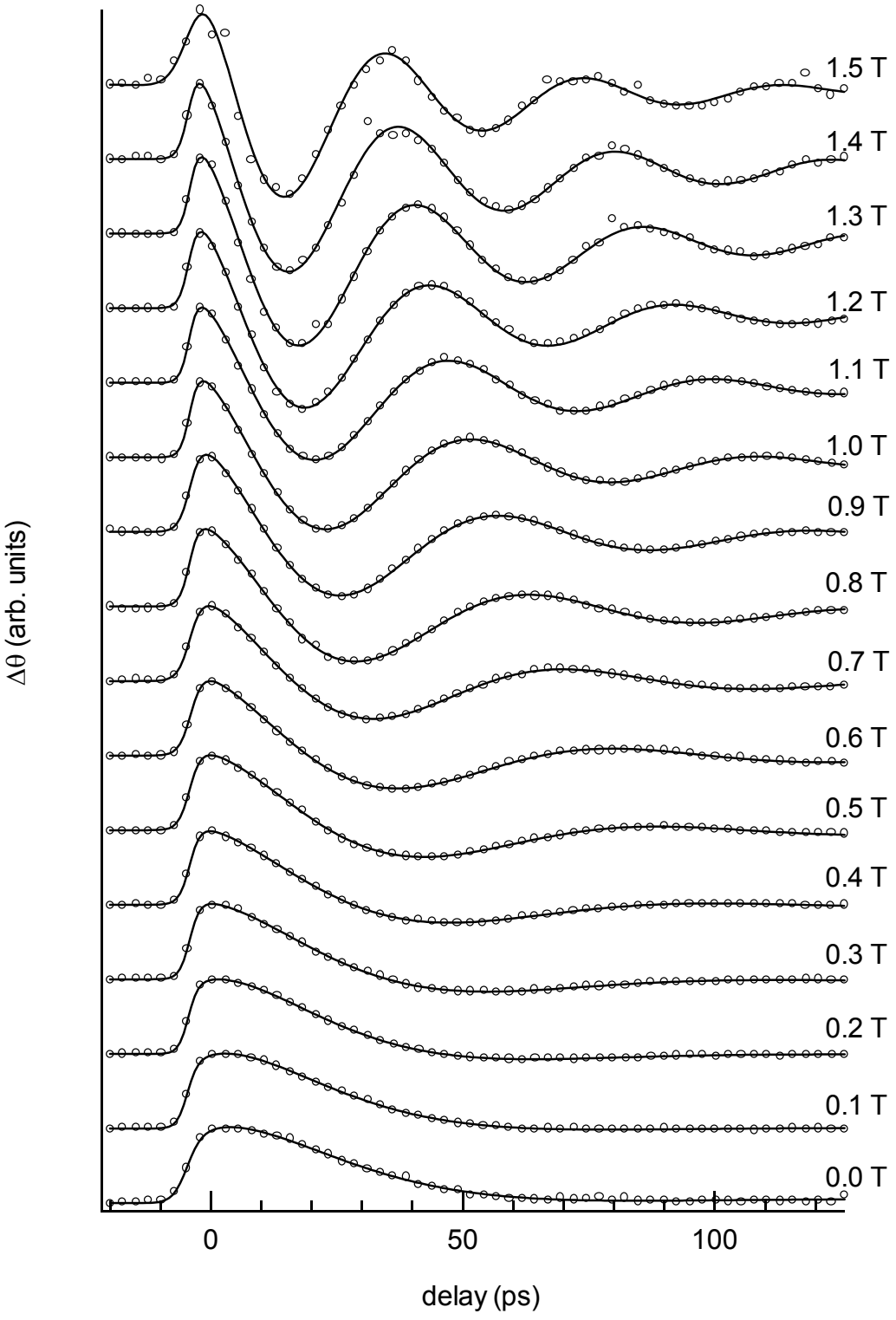

Figure 6.6: Time resolved probe rotation induced by the coherent exciton population in a magnetic applied at 43^{o} to the sample normal, with field strengths from 0 to 1.5 T as indicated.

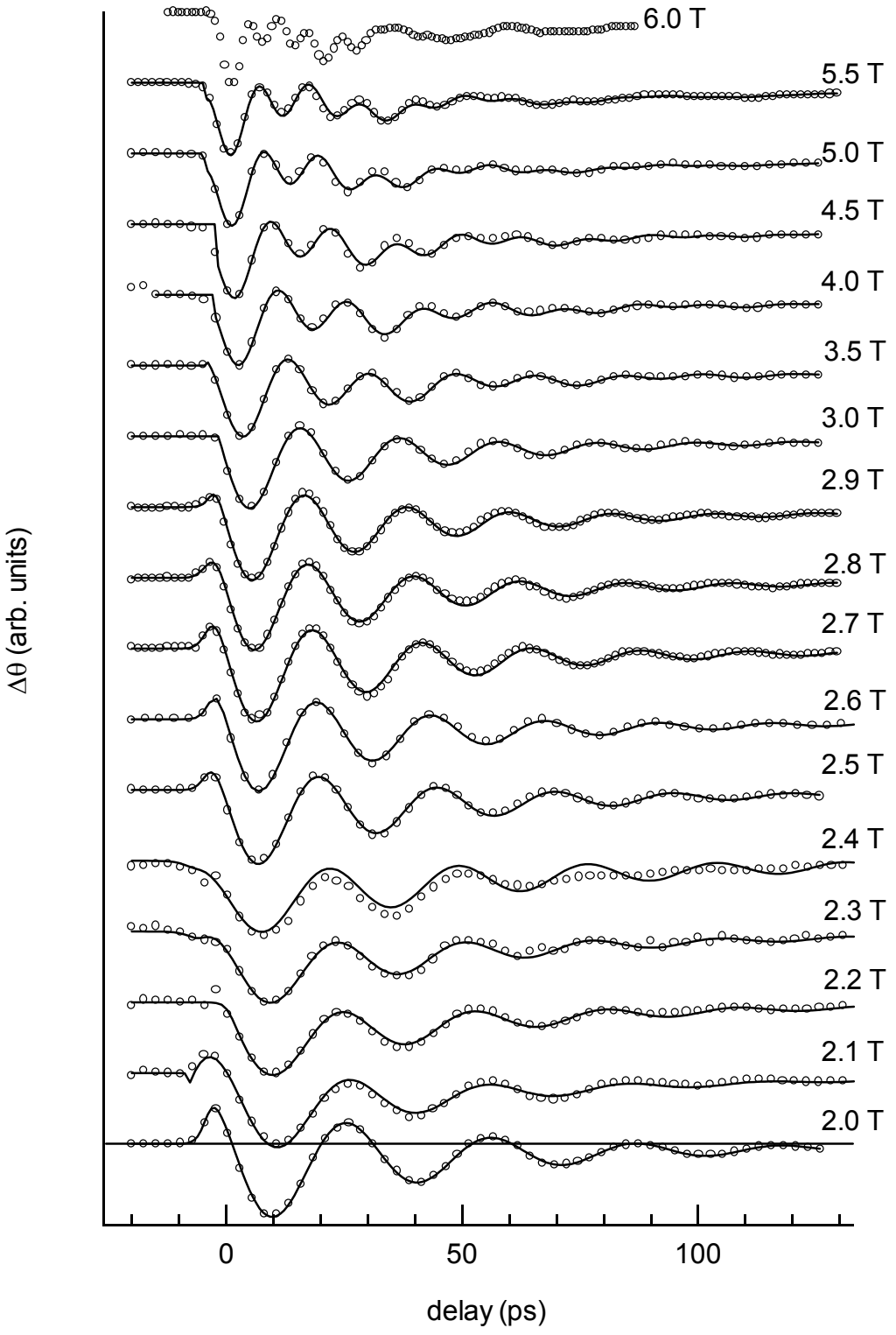

Figure 6.7: Time resolved probe rotation induced by the coherent exciton population in a magnetic applied at 43^{o} to the sample normal, with field strengths from 2 to 6 T as indicated.

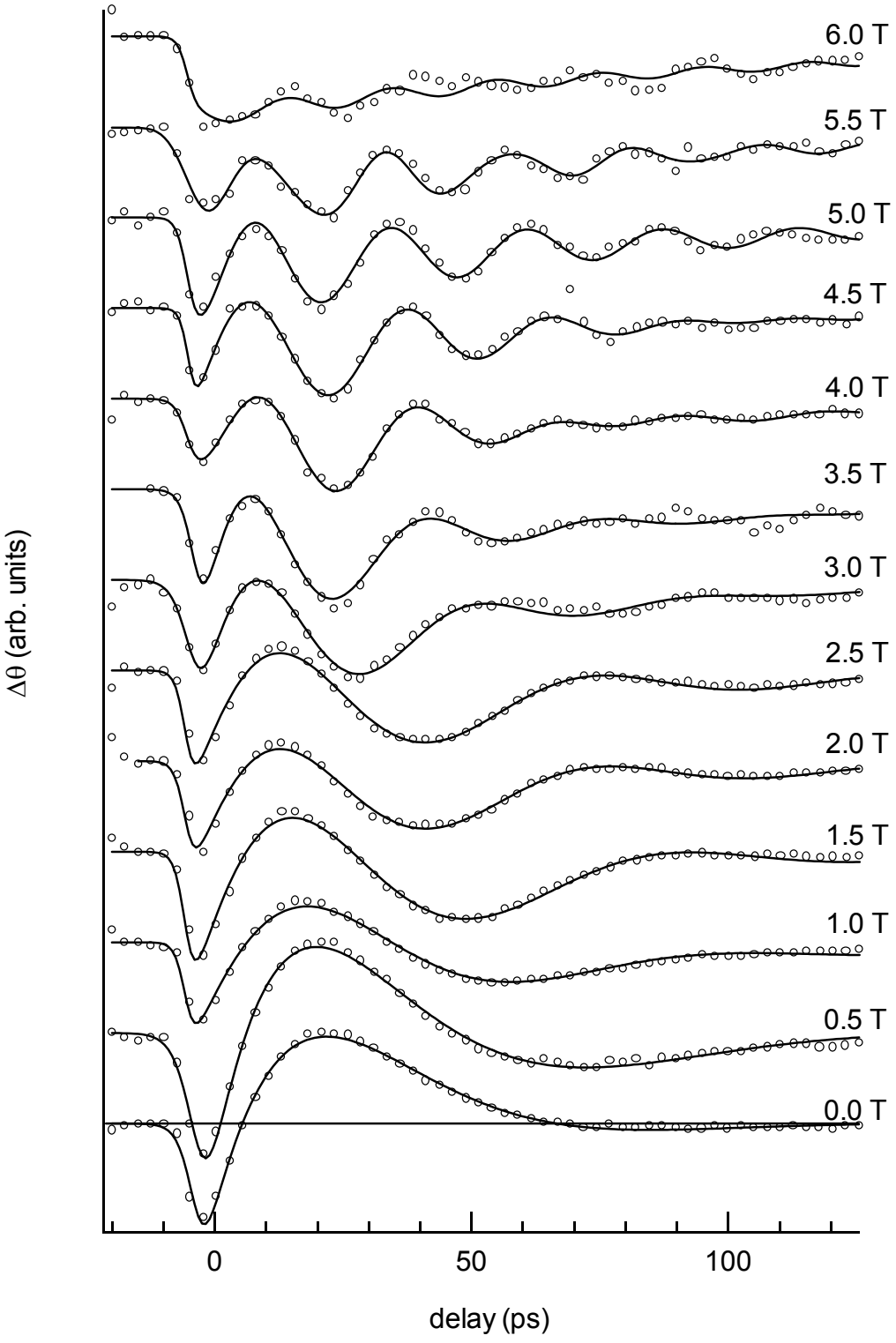

Figure 6.8: Time resolved probe rotation induced by the coherent exciton population in a magnetic applied at 73^{o} to the sample normal, with field strengths from 0 to 6 T as indicated.

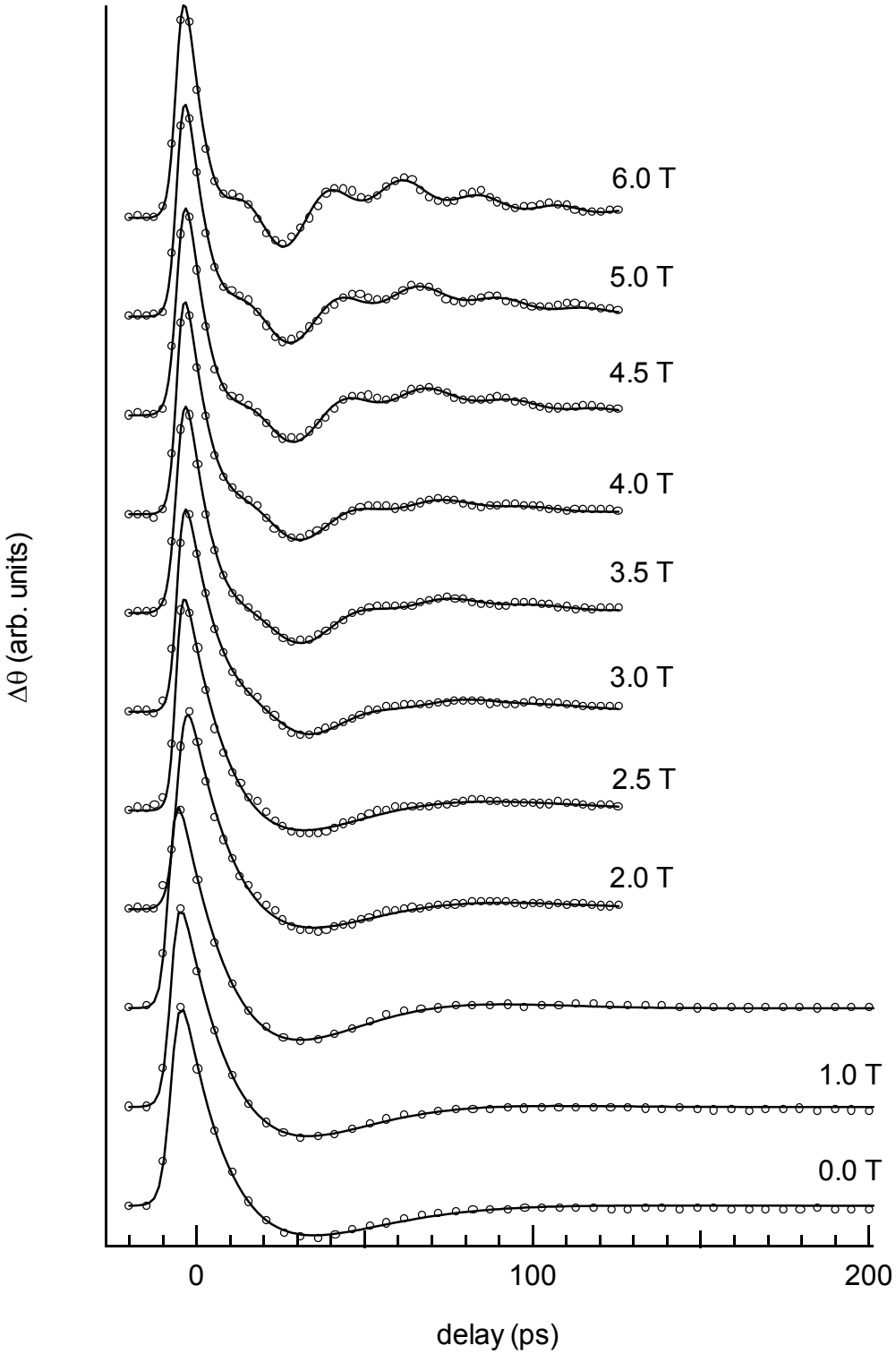

Figure 6.9: Time resolved probe rotation induced by the coherent exciton population in a magnetic applied at 87^{o} to the sample normal, with field strengths from 0 to 6 T as indicated.

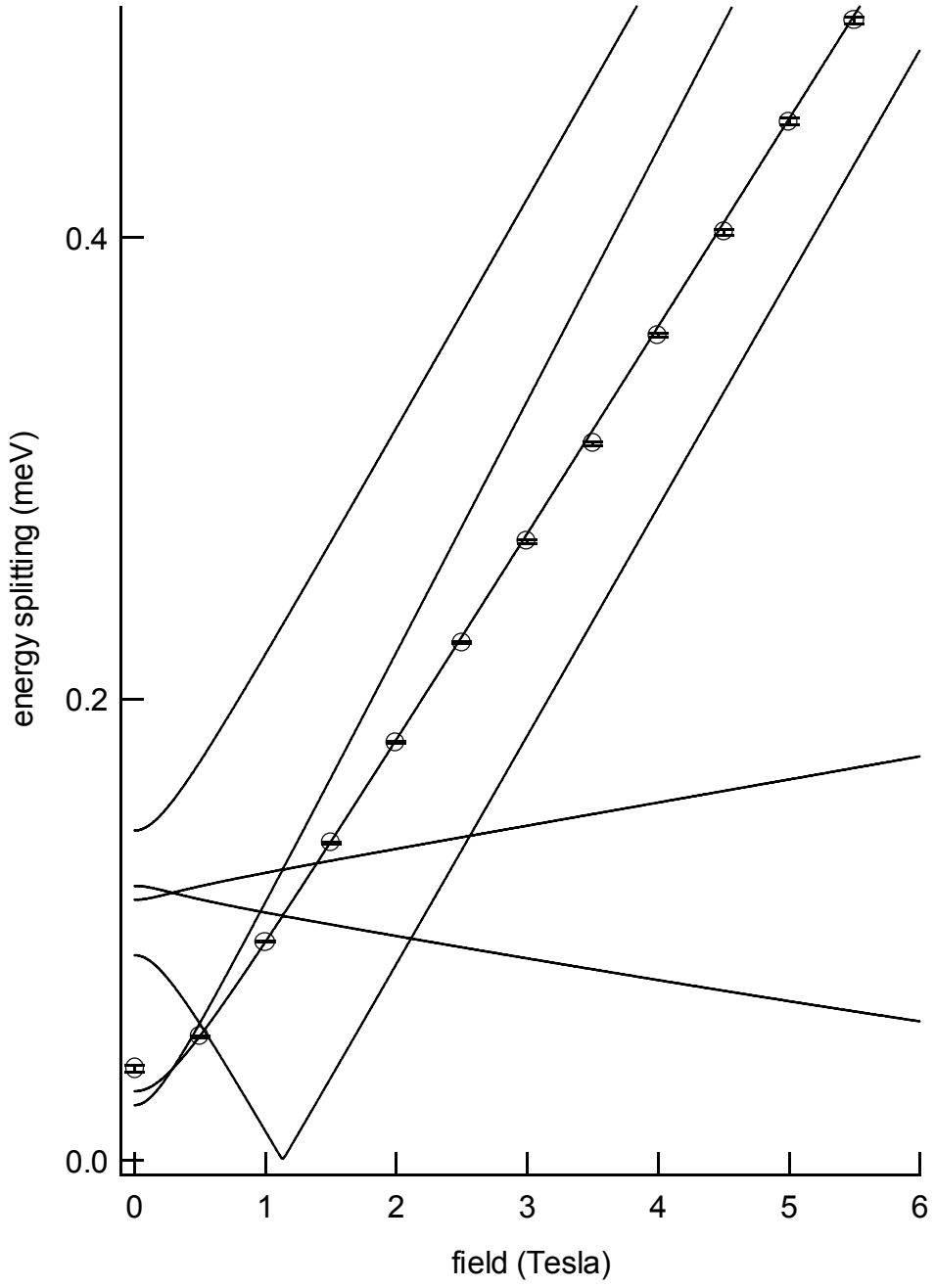

Figure 6.10: Beat frequency components in the time-resolved rotation signal from the 25.7 Å GaAs/AlGaAs multi-quantum well sample as a function of magnetic field strength applied at 8^{o} acute to the growth/excitation axis. Lines show all possible differences of the eigen values of the Hamiltonian for this configuration.

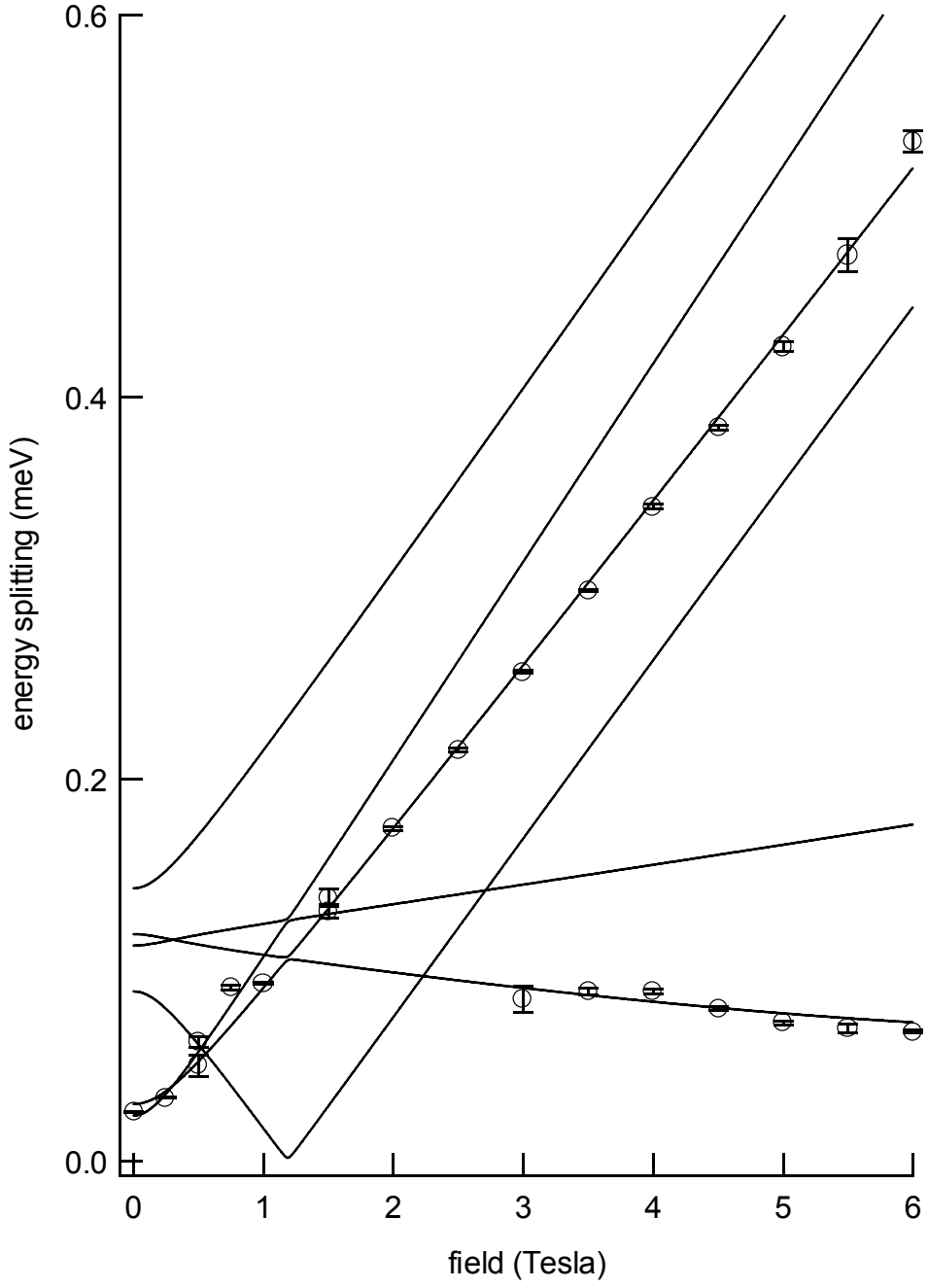

Figure 6.11: Beat frequency components in the time-resolved rotation signal from the 25.7 Å GaAs/AlGaAs multi-quantum well sample as a function of magnetic field strength applied at 19^{o} acute to the growth/excitation axis. Lines show all possible differences of the eigen values of the Hamiltonian for this configuration.

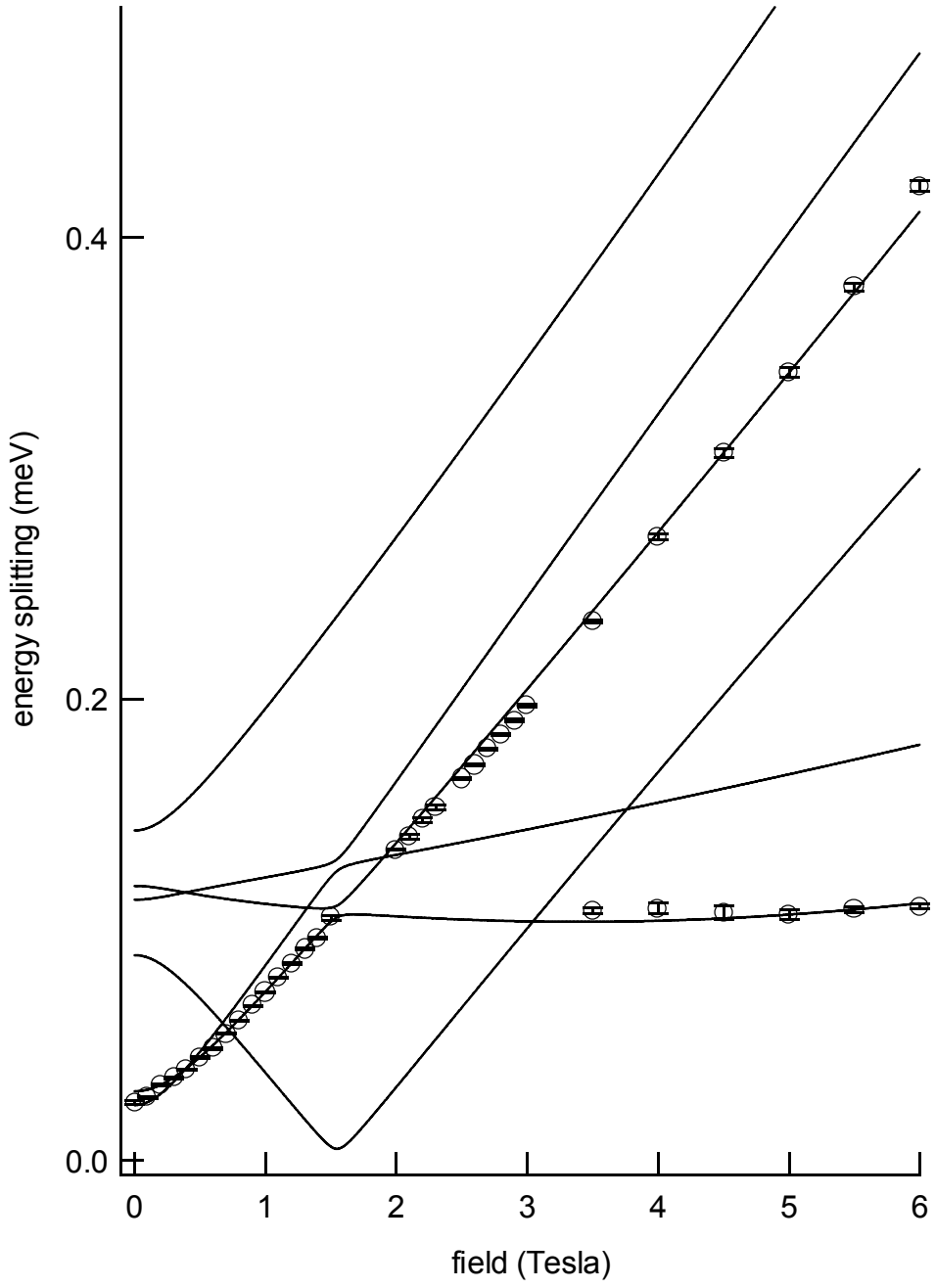

Figure 6.12: Beat frequency components in the time-resolved rotation signal from the 25.7 Å GaAs/AlGaAs multi-quantum well sample as a function of magnetic field strength applied at 43^{o} acute to the growth/excitation axis. Lines show all possible differences of the eigen values of the Hamiltonian for this configuration.

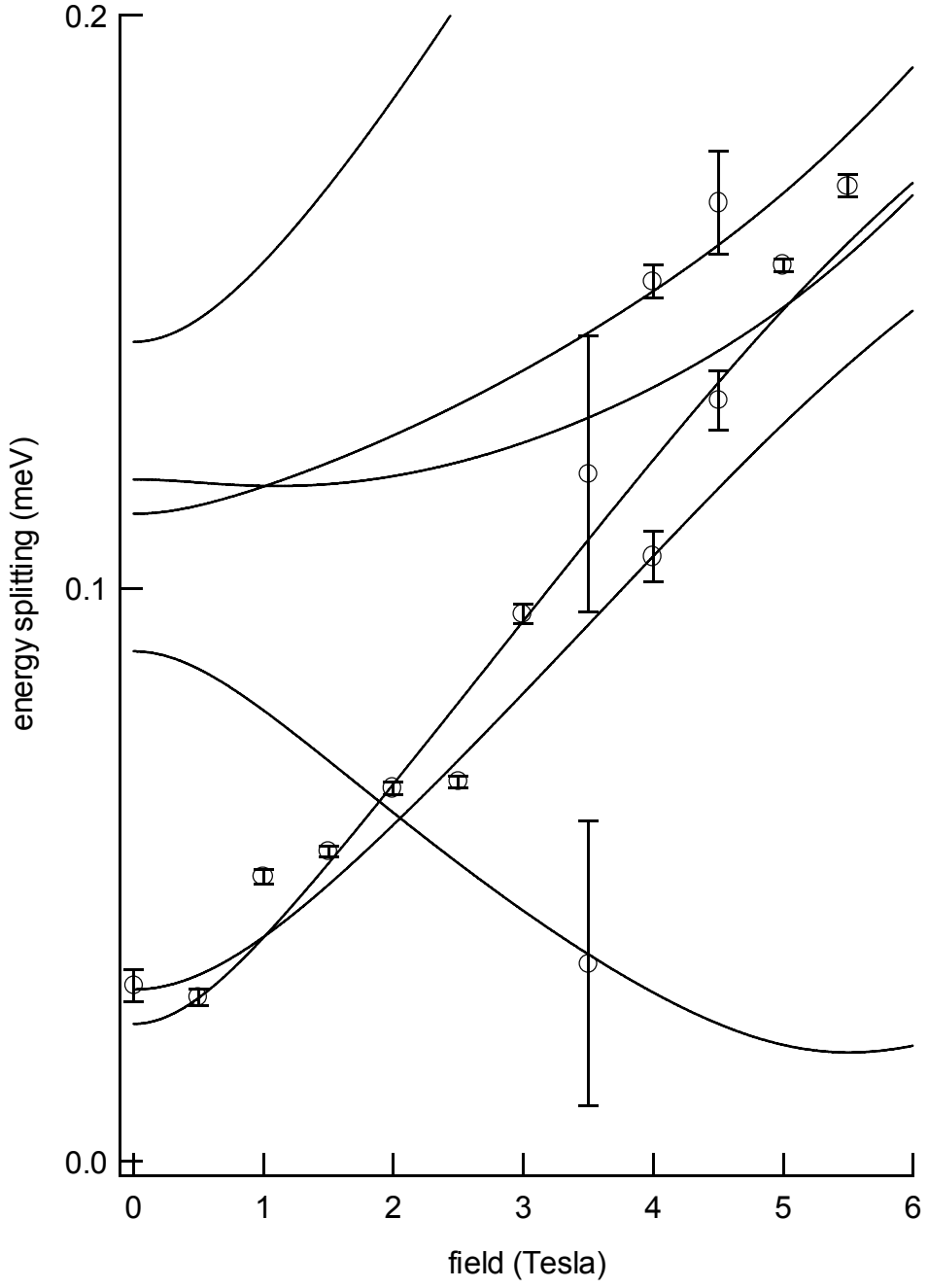

Figure 6.13: Beat frequency components in the time-resolved rotation signal from the 25.7 Å GaAs/AlGaAs multi-quantum well sample as a function of magnetic field strength applied at 74^{o} acute to the growth/excitation axis. Lines show all possible differences of the eigen values of the Hamiltonian for this configuration.

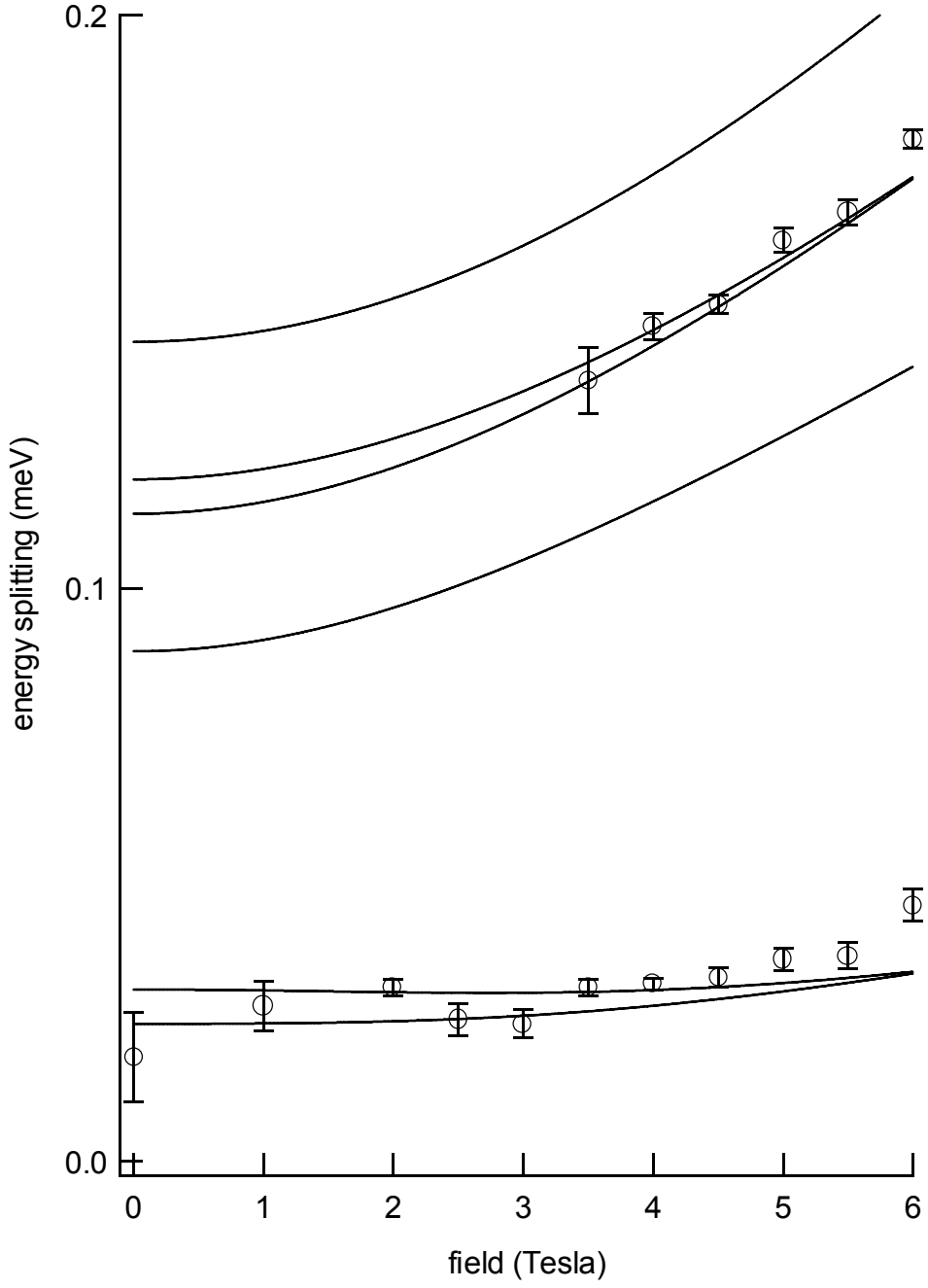

Figure 6.14: Beat frequency components in the time-resolved rotation signal from the 25.7 Å GaAs/AlGaAs multi-quantum well sample as a function of magnetic field strength applied at 87^{o} acute to the growth/excitation axis. Lines show all possible differences of the eigen values of the Hamiltonian for this configuration.

6.6 Summary and Conclusions

We have used a time-resolved birefringence method to optically probe the spin splittings of heavy-hole excitons in a sample which has symmetry lower than D_{2D}. The effect of this symmetry, namely the splitting of the optically active exciton states in the absence of a magnetic field, was observed; we also directly measured quantum beats between the optically inactive and active spin states. There was good agreement between the dependencies on the magnetic field of the measured splittings and the Hamiltonian of equation 6.**1**, and the measurement provided precise values (10 % error) for the anisotropic exchange components and the electron and hole g-factors.

6.7 References

1. **"Exchange interaction of excitons in GaAs heterostructures"**, E. Blackwood, M. J. Snelling, R. T. Harley, S. R. Andrews and C. T. B. Foxon, *Phys. Rev. B **50** 14262 (1994).*

2. **"Fine structure of excitons in type-II GaAs/AlAs quantum wells"**, H. W. van Kesteren, E. C. Cosman, and W. A. J. A. van der Poel, C. T. Foxon. *Phys. Rev. B **41** 5283 (1990).*

3. **"Transient linear birefringence in GaAs quantum wells: Magnetic filed dependence of coherent exciton spin dynamics"**, E. Worsley, N. J. Traynor, T. Grevatt, and R. T. Harley, *Phys. Rev. Lett. **76** 3224 (1996).*

4. **"Coherent dynamics of coupled electron and hole spins in semiconductors"**, D. Hägele, J. Hübner, W. W. Rühle, and M. Oestreich, *Solid Stat. Commun. **120** 73 (2001).*

5. **"Magnetic g factor of electrons in GaAs/Al_xG_{1-x}aAs quantum wells"**, M. J. Snelling, G. P. Flinn, A. S. Plaut, R. T. Harley, A. C. Tropper, R. Eccleston, and C. C. Phillips, *Phys. Rev. B **44** 11345 (1991).*

6. **"Exciton, heavy-hole, and electron g factors in type-I GaAs/Al_xG_{1-x}aAs quantum wells",** M. J. Snelling, E. Blackwood, C. J. McDonagh, R. T. Harley, and C. T. B. Foxon, *Phys. Rev. B **45** 3922 (1992).*

7. **"Zeeman splitting and g factor of heavy-hole excitons in In_xGa_{1-x}As/GaAs quantum wells"**, N. J. Traynor, R. T. Harley, and R. J. Warburton, *Phys. Rev. B **51** 7361 (1995).*

8. **"Highly nonlinear Zeeman splitting of excitons in semiconductor quantum wells"**, N. J. Traynor, R. J. Warburton, M. J. Snelling, and R. T. Harley, *Phys. Rev. B **55** 15701 (1997).*

9. “Investigation of g-factors, Zeeman splittings, exchange interactions and field-dependent spin relaxation in III-V quantum wells”, N. J. Traynor, M. J. Snelling, R. T. Harley, R. J. Warburton, and M. Hopkinson, *Surface Science B 361/362 435 (1996).*

10. **“Time-resolved relaxation processes in quantum wells”**, R. E. Worsley, Ph.D. thesis University Of Southampton, (1995).

11. **“Anisotropy of the electron g factor in lattice-matched and strained III-V quantum wells”**, A. Malinowski and R. T. Harley, *Phys. Rev. B. **62** 2051 (2000).*

12. **“Spin quantum beats of 2D excitons”**, T. Amand, X. Marie, P. Le Jeune, M. Brousseau, D. Robart, J. Barrau and R. Planel, *Phys. Rev. Lett. **78** 1355 (1997).*

13. **“Coherent spin dynamics of excitons in quantum wells”**, M. Dyakonov, X. Marie, T. Amand, P. Le Jeune, D. Robart, M. Brousseau, J. Barrau. *Phys. Rev. B. **56** 10412 (1997).*

14. **“Theory of spin beatings in the Faraday rotation of semiconductors”**, Th. Östreich, K. Schönhammer, and L. J. Sham, *Phys. Rev. Lett. **75** 2554 (1995).*

15. **“Optical orientation in quantum wells”**, M. J. Snelling, Ph.D. thesis, University Of Southampton (1991).

16. **“Tilted field exciton beats in a quantum well”,** A. Malinowski, M. A. Brand and R. T. Harley, *Solid. State Commun. **116** 333 (2000).*

17. 3D fitting method carried out by A. Malinowski, results published in reference

7. Conclusions

This thesis has described some experiments on the time evolution of spin polarised transient carrier populations in III-V semiconductor quantum wells which are excited and probed by short laser pulses. The measurement method consisted of monitoring the intensity change (ΔR) and the rotation ($\Delta\theta$) of the azimuthal polarisation plane of a reflected linearly polarised probe pulse derived from the same source as the exciting pulse. Initial polarisation of the transient population was manipulated by setting the polarisation of the exciting pulse and time evolution was monitored by taking measurements with various delays set in the optical path of the probing pulse.

At the start of work on the high mobility sample (discussed in chapter 4) we had hoped to observe quasi-free electron spin precession in the absence of a magnetic field, leading to a direct measurement of the conduction band spin-splitting. Dr. A Malinowski had previously obtained a weak overshoot of the relaxing $\Delta\theta$ signal (which indicates the spin polarisation along the growth axis) from a similar sample of slightly lower mobility (sample NU211). At the time the heavy damping was thought due to low mobility. We were only able to detect heavily damped precession in our sample also, and then only at the lowest temperature (1.8 K), despite the known high mobility - which indicated that quasi-free precession ought to prevail at temperatures up to ~100 K. Investigation of the full temperature dependence of spin evolution showed was an extra scattering process, ignored in previous theoretical treatments. By Monte-Carlo simulation we demonstrated that evolution could only be reproduced with a scattering rate much higher than indicated by the mobility – otherwise it predicted quasi-free precession up to ~100 K. We concluded that, whilst the D'Yakonov-Perel mechanism was operative, some other scattering process was the cause of motional slowing of precession. The temperature dependence of the active scattering mechanism was very similar to that expected

of electron-electron scattering by Coulomb interaction, which disappears at low temperature due to Fermi blocking and does not affect the mobility of the 2DEG. On this basis we suggested [1] that the electron-electron scattering must be used when applying the D'Yakonov-Perel spin relaxation mechanism to observations in 2DEGs.

Previous measurements [2] of electron spin relaxation in undoped InGaAs/InP quantum wells showed room temperature values much faster, ~5 ps, than in undoped GaAs/AlGaAs wells [3]. Two differences between those nanostructures are the existence of native interface asymmetry and the ternary nature of the well material in InGaAs/InP. The experiments undertaken in this thesis measured a very slow electron spin relaxation in undoped InGaAs/GaAs quantum wells (chapter 5) and we conclude that the native interface asymmetry was the reason for the fast spin relaxation observed in InGaAs/InP. The measured spin evolution at low temperature was clearly affected by coupled electron-hole (exciton) spin-flip and we obtained values for the long-range exchange interaction strength as a function of temperature. At higher temperatures the carriers were able to escape from the quantum wells which were shallow due to the low Indium content; calculations were presented to explain the rates of signal decay based on estimates of the activation energy which were consistent with measurements by others.

Finally, we made a study of quantum beats due to excitons at low temperatures and in applied magnetic field in an undoped GaAs/AlGaAs type I multiple quantum well structure using the optically induced linear birefringence method developed in our group by Worsley et al. [4, 5]. The aim was to make direct observation of the optically inactive excitons by time-resolving quantum beats with a magnetic field applied at various angles to the growth direction which admixes the inactive and active exciton spin states (see chapter 6). We used a unique sample holder arrangement developed by Malinowski and Harley [6] and measured the

electron and hole g-factors and the anisotropic short-range exchange strength to high precision. We also observed the lifting of degeneracy by imperfections of the quantum well which lower the symmetry below the ideal D_{2d}.

7.1 References

1. **"Precession and Motional Slowing of Spin Evolution in a High Mobility Two-Dimensional Electron Gas",** M. A. Brand, A. Malinowski, O. Z. Karimov, P. A. Marsden, R. T. Harley, A. J. Shields, D. Sanvitto, D. A. Ritchie, and M. Y. Simmons. *Physical Review Letters, **89** 239901 (2002).*

2. "Investigation of narrow-band semiconductor quantum well structures using a synchronously-pumped optical parametric oscillator", P. A. Marsden, *Ph.D. thesis, University Of Southampton (2001).*

3. **"Exciton vs free-carrier spin-relaxation in III-V quantum wells"**, A. Malinowski, P. A. Marsden, R. S. Britton, K. Puech, A. C. Tropper and R. T. Harley, *Proc. 25th Int. Conf. Phys. Semicond., Osaka, Part **1** 631 (2001).*

4. **"Transient linear birefringence in GaAs quantum wells: Magnetic filed dependence of coherent exciton spin dynamics"**, E. Worsley, N. J. Traynor, T. Grevatt, and R. T. Harley, *Phys. Rev. Lett. **76** 3224 (1996).*

5. **"Time-resolved relaxation processes in quantum wells"**, R. E. Worsley, Ph.D. thesis University Of Southampton, (1995).

6. **"Anisotropy of the electron g factor in lattice-matched and strained III-V quantum wells"**, A. Malinowski and R. T. Harley, *Phys. Rev. B. **62** 2051 (2000).*

8. List of Publications

"Ultrafast spin evolution in high-mobility 2DEGs", R. T. Harley, M. A. Brand, A. Malinowski, O. Z. Karimov, P. A. Marsden, A. J. Shields, D. Sanvitto, D. A. Ritchie, M. Y. Simmons, *Physica E*, **17** 324 *(2003).*

"D'Yakonov-Perel' spin relaxation under electron-electron collisions in n-type QWs", M. M. M. Glazov, E. L. Ivchenko, M. A. Brand, O. Z. Karimov and R. T. Harley. Proceedings of the international symposium "Nanostructures: Physics and Technology", St.-Petersburg, Russia (*accepted, 2003).*

"Precession and Motional Slowing of Spin Evolution in a High Mobility Two-Dimensional Electron Gas", M. A. Brand, A. Malinowski, O. Z. Karimov, P. A. Marsden, R. T. Harley, A. J. Shields, D. Sanvitto, D. A. Ritchie, and M. Y. Simmons. *Physical Review Letters, **89** 239901 (2002).*

"Spin evolution in high mobility 2DEG: optical study of precession and motional slowing", M. A. Brand, A. Malinowski, O. Z. Karimov, P. A. Marsden, R. T. Harley, A. J. Shields, D. Sanvitto, D. A. Ritchie, M. Y. Simmons, *to be published in Proceedings of the 26th international conference on the physics of semiconductors (ICPS), World Scientific, Edinburgh, UK (2002).*

"Optical study of electron spin evolution in high-mobility 2DEG's", M. A. Brand, A. Malinowski, O. Z. Karimov, P. A. Marsden, R. T. Harley, A. J. Shields, D. Sanvitto, M. Y. Simmons, D. A. Ritchie, *Abstracts of the Rank Prize Funds mini-symposium on optical orientation and spintronics, Grasmere, Cumbria, UK, 18-21 March (2002).*

"Nuclear Effects in Ultrafast Quantum-Well Spin-Dynamics", A. Malinowski, M. A. Brand and R. T. Harley, *Physica E **10**, 13 (2001).*

"Tilted Field Exciton beats in a Quantum Well", A. Malinowski, M. A. Brand and R. T. Harley, *Solid. State Commun. **116** 333 (2000).*